The Dissertation Committee for Danlu Wang Certifies that this is the approved version of the following dissertation:

Phase-driven Optomechanics in Exotic Photonic Media

Committee:

Zheng Wang, Supervisor

Xiaoqin E. Li, Co-Supervisor

Keji Lai

Ernst-Ludwig Florin

Phase-driven Optomechanics in Exotic Photonic Media

by

Danlu Wang

Dissertation

Presented to the Faculty of the Graduate School of

The University of Texas at Austin

in Partial Fulfillment

of the Requirements

for the Degree of

Doctor of Philosophy

The University of Texas at Austin

May 2018

Dedication

To my family.

Acknowledgements

I would like to thank my adviser Prof. Zheng Wang and co-adviser Prof. Xiaoqin E. Li for their guidance, wisdom, broad knowledge in different research topics throughout my PhD Journey. I am grateful to my current and previous committee members, Prof. Keji Lai, Prof. Ernst-Ludwig Florin and Prof. Gennady Shvets for discussions in photonics. I express my sincere gratitude to the LAND group members: Boxue Chen, Ryan Cho, Dr. S. Hossein Mousavi, Thien-An N. Nguyen and Dr. Ian A.D. Williamson, for discussions and helps on simulation software. I thank all my friends for sharing the joy of life. I thank my parents and grandparents for always supporting me in all my endeavors. Finally, I would like to thank my partner, Dr. Xing Zhang, for being with me.

Phase-driven optomechanics in exotic photonic media

Danlu Wang, Ph.D.

The University of Texas at Austin, 2018

Supervisor: Zheng Wang

Integrated photonics provide unique advantages in tailoring and enhancing optical forces. Recent advancements in integrated photonics have introduced many novel phenomena and exotic photonic media, such as photonic topological insulator, negative index material, photonic crystals, 2D material, and strongly-modulated time-dynamic systems. In my dissertation, I theoretically and numerically explore the novel properties and applications of optical forces in these systems.

We propose guided-wave photonic pulling forces in photonic crystal waveguides. Photonic crystal waveguides offer great capability to define the mode properties, and can incorporate complex trajectories, leading to unprecedented flexibility and robustness compared to previous works in free space or in longitudinally uniform waveguides. With response theory, a virtual work approach on optical forces, we establish general rules to tailor optical forces in periodic structures involved with photonic crystals: pulling forces arise from negative gradients in the phase responses of the outgoing modes, which corresponds to forward scattering on the Bloch band diagram with unit cell function corrections. We devise robust forward scattering, first, using topologically protected nonreciprocal chiral edge states, second, using backward (i.e. negative index) waves in a reciprocal system. The structures are tailored to accommodate only the necessary modes, which largely benefits the robustness. With these, we numerically demonstrate long range

pulling forces on arbitrary particles through sharp corners. Our work paves the way towards sophisticated optical manipulation with single laser beam.

We next explore the implication and applicability of momentum conservation in periodic media, which has been unclear due to the inhomogeneity and strong near field. We first quantify the linear momentum flux of Bloch modes under discrete translational symmetry, which is further understood from their plane wave composition. We then demonstrate through varies examples that the change in momentum flux predicts a total force distributed to both the scatterer and the media. However, one still need response theory to predict the forces on individual objects.

Using response theory, we can predict more general forms of optical forces. We numerically demonstrate optical motoring effect due to singularity in the phase responses, and strong optical forces between graphene sheets due to large gradients in the phase responses. In particular, by combining the strong forces in graphene guided-wave system and the exceptional elastic properties of graphene, we can get an SBS gain that is four orders of magnitude stronger than in a silicon step-index waveguide, which may lead to smaller devices for RF signal processing.

Table of Contents

List of Figures

Chapter 1: Introduction

Optical forces have been widely studied for its broad range of applications in biophysics[1]–[4], atomic physics[5] and integrated photonics[6]–[9]. In particular, integrated photonics offer unique degrees of freedom to tailor and enhance the optical field and light-matter interactions. For example, one can design waveguides or resonators to generate large optical forces that can create deformation or displacement, in order to dynamically tune the optical properties of the system[6], [7]. More recently, optical forces are used to produce high-frequency mechanical waves, via a process known as Stimulated Brillouin scattering. This process can provide gain for GHz phonons[10], [11], cascaded Stokes photons[12], and can coherently transduce signals between light and sound waves[13].

Over the past few decades, advancements of integrated photonics have incorporated many novel ingredients such as subwavelength scale structural features [14]–[16], photonic crystals[14], magneto-optical materials[17], 2D materials[18]–[20], strongly time-modulated dynamics [21], [22], etc., leading to exotic photonic properties. For instance, using photonic crystals or metamaterials, one can realize novel dispersion relations such as negative index[23]–[26] and slow light[27], [28]. Using magneto-optical materials[17], [29], [30] or temporal modulation[21], [31], [32], one can break the time reversal symmetry, which leads to non-reciprocal propagation of light. By carefully designing the nontrivial band structure and Bloch modes, people have realized the photonic analog of topological insulators, which leads to topologically protected light propagation[17], [29], [32]–[34]. Using 2D materials that interact strongly with photons, one can enhance the optical field by orders of magnitude[35], [36]. However, for most of these systems, only their optical properties were well studied, whereas their potential applications to optical

forces are yet to be explored. Furthermore, the optical forces in these novel systems may behave quite differently compared with those in conventional systems. Here, we list a few examples as follows:

(1) Topological photonics have been applied to protect the propagation of light[17], [29], [32]–[34], while their potentials to protect optical forces have not yet been explored. We envision having unidirectional forces guided through arbitrary waveguide trajectories in these systems. In particular, the robustness of the rare photonic pulling forces[37] that are directed opposite to the incident light may be improved under topological protection, which would greatly improve the flexibility of optical manipulation with a single laser beam. Because conventionally the optical manipulation are limited to gradient forces and positive radiation pressure[1].

(2) Negative index (also referred to as backward-waves) has been proposed to generate optical pulling forces in longitudinally uniform structures [24], [25]. However, the definition of negative index becomes problematic when generalized to Bloch modes for periodic systems. Because the periodic band structure of Bloch modes leads to ambiguity as one tries to determine the sign of the wave-vector in the periodic system[38], which in turn results in ambiguity in the direction of optical forces.

(3) How to apply momentum conservation in periodic structure is not as straightforward as in free space[39]–[41]. A scattering particle immersed inside the periodic medium can generate substantial near field, which distributes the scattering forces to the periodic medium itself. It is unclear what quantity governs the total force, and how the total force is distributed to the particle and the periodic medium.

(4) For optical manipulation of objects inside those aforementioned inhomogeneous photonic media, it would be desirable to have a general theory that can tailor optical forces purely based on the intrinsic properties of the eigen modes supported

by the media, such as band structure and field profile, rather than being distracted by the chaotic instantaneous near fields at presence of the manipulated objects. The analysis on optical forces can also extend to optical torques, for realizing photonic motors in integrated system.

(5) It is also worth investigating whether and how the field enhancement by novel 2D materials[35], [36] translates to significantly stronger optical forces and photon-phonon couplings.

In my PhD work, I conduct theoretical and numerical studies to address these unexplored aspects about the optical forces in novel photonic systems, and to unlock new possibilities for optical manipulation.

A main line that underlies our optical forces analysis is response theory[42], [43]. Conventionally, the strong near field in inhomogeneous photonic media largely limited the understanding of optical forces to first-principle calculations, such as the Maxwell stress tensors (MST)[44]. While the MST method is reliable, it offers little intuition for the design of a system to achieve a desired optical force profile, as a small displacement may drastically change the near field. Fortunately, integrated photonic systems can often be abstracted into a handful of ports[45], [46], and there exist rigorous analytical connection between the responses of the ports caused by the motion of an object and the optical forces experienced by the object, known as the response theory of optical forces (RTOF)[42], [43]. In particular, the phase responses contain the richest design insights towards the optical forces. For example, negative gradients in the phase responses indicate optical pulling forces which are directed oppositely to the incident light (Chapter 3, 4). Singularities in the phase responses indicate non-conservative forces (Chapter 6). Large gradients in the phase responses indicate enhancement of optical forces (Chapter 2, 7). More intriguingly, the responses offer an universal design guidance, which is somewhat

independent of the underlying implementation[42]. For example, we have synthesized negative gradients in the phase responses using two completely different photonic crystals, and they both realized robust photonic pulling forces (Chapter 3, 4). However, given the elegance of response theory, there still exist challenges that we need to address. First, the prediction of the responses requires good understandings about the system, including the eigen properties of the ports (and resonators if applicable) and how they exchange energy spatially and temporally (Chapter 2-4, 6). This also leads to the development of our theories that use band structures and eigen mode profiles to tailor optical forces inside the photonic media (Chapter 3-4, 6). Second, eliminating unwanted ports may require special design efforts. For example, to get robust photonic pulling forces, we have resorted to topological protection (Chapter 3), dispersion engineering (Chapter 4, 8), and optimization techniques (Chapter 8) to eliminate unwanted ports.

The arrangement of this dissertation is as follows: In Chapter 2 we review the numerical methods that we have used in characterizing the optical properties and optical forces. We use frequency domain studies and finite element method to solve the Maxwell's equations in the highly inhomogeneous medium that we use[47], [48]. On optical forces, we address several different numerical realizations for the calculation of MST forces[44]; we demonstrate the agreement between the RTOF calculated forces [42] and the MST calculated forces; and we highlight the intuitions provided by RTOF. RTOF requires accurate characterization of the ports and their responses (i.e. scattering matrix). Ports are usually attributed to propagating eigen modes, which are identified using eigen value studies. The responses are numerically found from full-wave study and are often predictable from intuitive understating about the system. We demonstrate these procedures with an example.

In Chapter 3 we generalize the topological protection of light propagation to topologically protected photonic pulling forces in guided-wave system, with a highlight on the unprecedented robustness of the puling forces to support arbitrary particle properties, multiple particles, complex trajectories and long operational length, compared with the pulling forces proposed in previous works [24], [25], [37], [49]–[62]. The topological protection origins from the reflection-free property of the chiral edge states (CES)[29], a photonic analog of the surface states on topological insulators whose conductivity is invariant to imperfections[63]. We devise forward scattering between these CESs that have different wavenumbers to generate the pulling forces. The understanding of forward scattering in photonic crystals which are required for the CESs, however, is different from the conventional momentum conservation picture. Instead, we use RTOF to establish rigorous correspondence between the forward scattering on the Bloch band diagram incorporating the mode profiles, and the negative gradients in the phase responses, which all point towards pulling forces. Along the way, we analyze special symmetries in the responses that greatly simplifies the RTOF analysis. In addition to multi-mode scattering, we demonstrate that absorption on the manipulated particle can also be devised into forward scattering which generates photonic pulling forces.

In Chapter 4 we switch gears to use backward waves (i.e. negative index waves) to implement the pulling forces in an all silicon single-mode waveguide, which is highly chip-compatible. Backward waves have been proposed as a general approach to generate optical pulling forces in complex media, such as photonic crystals[23] and metamaterials[24], [25]. Although this approach applies to a broad range of scatterers, the general coexistence of forward waves in these systems allows optical pushing forces to be unintentionally introduced, especially when multiple scattering events occur. In this context, we explore the generation of robust optical pulling forces from backward waves in a single-mode

waveguide synthesized by dispersion engineering in a photonic crystal line defect. We also formulate the general criterion that distinguishes genuine backward waves that produce pulling forces from "aliased" backward waves that produce pushing forces, which is a unique problem encountered in periodic structures such as photonic crystals. We numerically demonstrate our results using first-principle simulations, in excellent agreement with analysis from the response theory of optical forces. A single-mode waveguide supporting genuine backward waves paves the way towards nanomanipulation in optical circuits with topologies that match the complexity found in state-of-art microfluidics.

In Chapter 5 we investigate the concept of momentum conservation for Bloch modes in periodic systems, which is not yet fully understood[41]. First, we identify that the linear momentum flux is a conservative quantity and an intrinsic property for a Bloch mode, thanks to the discrete translational symmetry. We visualized the momentum flux into spectra which exhibit great distinctions from the conventional band structures in both the magnitude and signs. We analyze the momentum flux by decomposing it into contributions from the underlying plane wave components. Next, to address the momentum conservation in periodic structures, we notice that a change in the momentum flux transfers to a total force that is distributed to all the dielectrics in the near field, including both the defect/scatterer and the surrounding structure. As an application of this concept, compressive/expansion forces can be predicted from the change of the momentum flux at interfaces of different periodic structures supporting different Bloch modes. On the other hand, by revisiting the setup in Chapter 3, where a particle experiences pulling forces inside a photonic crystal waveguide that is barely correlated with the total forces accompanied by momentum conservation, we recognize that the response theory is still the best suitable

approach to predict forces on an individual object being manipulated inside a periodic structure.

In Chapter 6 we propose an optical motor around a phase singularity in a photonic crystal cavity. By taking analogy with a free space experiment where a lossy test particle is driven into cyclic motion by a helical beam in 3D[64], [65], we implement the photonic motor into a 2D integrated photonic system, where the field profile that leads to the motoring effect is entirely shaped by the photonic crystal structure. Unlike in free-space, here the motoring effect is confirmed only when there exists a port that perceives the phase singularity of the electromagnetic field into its phase response, according to RTOF[43]. We find that a manipulated lossy particle can be devised into such a port. We also give a theoretical upper limit of the torque, assuming the cavity is excited by side-coupling to a single port, operating on resonance and at critical coupling.

In Chapter 7 we study the optomechanics in the integrated graphene photonic system. We extend the extraordinary wavelength reduction of the guided quasi-TEM mode between parallel graphene sheets at THz[35] to generate strong optical forces. At a 30nm gap size, the forces are 40 times stronger than in a silicon step-index waveguide[66]. Using RTOF analysis, we explain an interesting observation about the quasi-TEM mode, which always generates attractive forces irrespective of dispersion tuning. Combining the strong optical forces and the exceptional mechanical properties of graphene, we find that a doubly clamped parallel graphene waveguide can support an SBS gain of 4e8/W/m, which is 4 orders of magnitude stronger than in a Silicon step-index waveguide[10]. Graphene optomechanics may lead to smaller devices for RF signal processing.

In Chapter 8, we incorporated gradient based topology optimization[67]–[69] to replace human effort in the dispersion engineering task encountered in Chapter 4. In this optimization method, the design parameters are the dielectric properties on each pixel (i.e.

discretized mesh elements) in a defined volume in the device. The target function and constraints are specified with respect to the dispersion relations. The gradients of the target function and constraints versus the design parameters are constructed through the finite element method[47], [70]. The optimization opens up a 2.2% frequency range for the single mode operation of the backward-wave.

Chapter 2: Electromagnetic Simulation and Characterization of Optical Forces

This chapter reviews the numerical methods that we use in characterizing the optical property and optical forces in integrated photonic systems.

The mechanical motions involved in our works are orders of magnitude slower than the harmonics in the photonic waves. Therefore it is sufficient to use the electromagnetic fields from steady state solution of Maxwell's equation to calculate the optical forces. Using frequency domain method (Section 2.1.1), we can find the steady state solutions, including the frequency and field distribution from an eigen value study, and the field distribution from a full wave study. We use the Finite Element Method[47](Section 2.1.2) to solve the Maxwell's equation, because it provides accurate representation of complex geometry and is good at capturing local effects.

In free space, people often calculate optical forces using gradient forces and scattering forces[1]. Gradient forces are based on the gradients of field intensity, which is assumed be un-perturbed by the object (i.e. beads, particles). Scattering forces are based on the changes in photon momentum before and after scattering. However, optical forces are very different in integrated photonics systems. Gradient forces do not work because displacements often introduce drastic changes to the field profile. Scattering forces are chaotic in sub-wavelength scale inhomogeneous media, and can only be redefined under discrete translational symmetry (Chapter 3-5). Nevertheless, the first principle calculation from Maxwell Stress Tensor are still reliable [44] (Section 2.2.1), although it does not provide much intuition as the field distribution would change in response to the displacements. Response theory provides an alternative and more intuitive way to calculate optical forces[42], [43] (Section 2.2.2). It abstracts the integrated system into ports and relates the optical forces to the power and phase responses of the ports with respect to the

displacements, where we often theoretically come up with a predictable profile for the responses.

In Section 2.3 we walk through an example to characterize the optical properties and optical forces in an integrated system consisting of photonic crystal waveguide and cavity, with a highlight on the insights provided by response theory in predicting optical forces. Meanwhile, checking the agreement between Maxwell stress tensor and response theory calculated optical forces guarantees numerical accuracy.

2.1 ELECTROMAGNETIC SIMULATION

2.1.1 Solving Maxwell's Equations in Frequency-Domain

The macroscopic electromagnetic waves are governed by Maxwell's equations[44]:

$$\nabla \cdot \boldsymbol{B} = 0 \tag{2.1}$$

$$\nabla \cdot \boldsymbol{D} = \rho \tag{2.2}$$

$$\nabla \times \boldsymbol{E} = -\frac{\partial \boldsymbol{B}}{\partial t} \tag{2.3}$$

$$\nabla \times \boldsymbol{H} = \boldsymbol{J} + \frac{\partial \boldsymbol{D}}{\partial t} \tag{2.4}$$

where $\boldsymbol{E}$ and $\boldsymbol{H}$ are macroscopic electric and magnetic fields, $\boldsymbol{D}$ and $\boldsymbol{B}$ are displacement and magnetic induction fields, ρ and $\boldsymbol{J}$ are free charge and current densities. $\boldsymbol{D}$ to $\boldsymbol{E}$ and $\boldsymbol{B}$ to $\boldsymbol{H}$ are related by constitutive relations. For most dielectric materials, we can neglect the nonlinear terms in the constitutive relations, which yield $\boldsymbol{D}(\boldsymbol{r}) = \epsilon(\boldsymbol{r})\boldsymbol{E}(\boldsymbol{r})$ and $\boldsymbol{B}(\boldsymbol{r}) = \mu(\boldsymbol{r})\boldsymbol{H}(\boldsymbol{r})$, where ϵ and μ are the permittivity and permeability, $\boldsymbol{r}$ is the spatial coordinate.

Frequency-domain method separates the time dependence from the spatial dependence by expanding the fields into a set of harmonic modes.

$$\boldsymbol{E}(\boldsymbol{r}, t) = \boldsymbol{E}(\boldsymbol{r})e^{-i\omega t}, \quad \boldsymbol{H}(\boldsymbol{r}, t) = \boldsymbol{H}(\boldsymbol{r})e^{-i\omega t} \tag{2.5}$$

Substituting Eq.2.5 and the constitutive relations into Eq.2.1 -2.4, we obtain the Master's equations

$$\nabla \times (\mu^{-1}\nabla \times \boldsymbol{E}) - \omega^2 \epsilon \boldsymbol{E} = i\omega \boldsymbol{J} \tag{2.6}$$

$$\nabla \times (\epsilon^{-1}\nabla \times \boldsymbol{H}) - \omega^2 \mu \boldsymbol{H} = \nabla \times (\epsilon^{-1}\boldsymbol{J}) \tag{2.7}$$

It is evident that the solutions of Eq.2.6 also satisfies Eq.2.1, and the solutions of Eq.2.7 also satisfies Eq.2.2 [14], [47].

In frequency domain, we use two kinds of numerical study: Eigen value study and full-wave study[14]. Eigen value study is associated with source-free problems such as wave-propagation in waveguide and resonances in cavities. It finds the dispersion relation and the field profile of Eigen modes. Full-wave study is usually associated with scattering, radiation, and other problems where there exists a source or excitation. It finds the field distribution in realistic setups, e.g. optical manipulation of objects inside waveguides or cavities.

2.1.1.1 Eigen value study

In Eigen value study, since there is no sources, we can set $\boldsymbol{J} = 0$. Eq.2.6 and Eq.2.7 becomes

$$\nabla \times (\mu^{-1}\nabla \times \boldsymbol{E}) = \omega^2 \epsilon \boldsymbol{E} \tag{2.8}$$

$$\nabla \times (\epsilon^{-1}\nabla \times \boldsymbol{H}) = \omega^2 \mu \boldsymbol{H} \tag{2.9}$$

As the structure is specified, $\epsilon(\boldsymbol{r})$ and $\mu(\boldsymbol{r})$ are known. One can solve Eq.2.8 to find the Eigen frequency ω and the Eigen field $\boldsymbol{E}$, then use curl relation to find Eigen field $\boldsymbol{H}$. Or we can solve Eq.2.9 to find the Eigen frequency ω and the Eigen field $\boldsymbol{H}$, then use curl relation to find the Eigen field $\boldsymbol{E}$. For a structure that is uniform in one direction (e.g. z-direction), TM and TE polarization can be decoupled. One can solve Eq.2.8 to get E_z for

the TM polarization, and solve Eq.2.9 to get H_z for the TE polarization, then use the curl relation to find the other field components.

For photonic crystals, due to the periodicity, one can solve the Eigen frequency and Eigen fields for a unit cell, then apply discrete translational symmetry to the entire structure. Waves propagating in periodic systems are known as Bloch waves. Taking the $\boldsymbol{E}$ field as example, the Bloch wave function can be written as

$$\boldsymbol{E}(\boldsymbol{r}) = \boldsymbol{u_k}(\boldsymbol{r})e^{i\boldsymbol{k}\cdot\boldsymbol{r}} \tag{2.10}$$

where $\boldsymbol{u_k}(\boldsymbol{r})$ is the unit cell function, $\boldsymbol{k}$ is the Bloch wave vector. Eq.2.8 becomes

$$[(i\boldsymbol{k} + \nabla) \times \mu^{-1}(i\boldsymbol{k} + \nabla)] \times \boldsymbol{u_k}(\boldsymbol{r}) = \omega^2 \epsilon\, \boldsymbol{u_k}(\boldsymbol{r}) \tag{2.11}$$

Periodic boundary condition $\boldsymbol{u_k}(\boldsymbol{r}) = \boldsymbol{u_k}(\boldsymbol{r} + \boldsymbol{R})$ is applied, where $\boldsymbol{R}$ is the lattice vector. Solving Eq.2.11 for each $\boldsymbol{k}$ in the Brillouin Zone, we get the dispersion relation $\omega(\boldsymbol{k})$ and the corresponding Bloch wave functions.

The Eigen value study can be done using either MPB[71] or COMSOL Multiphysics[48]. MPB is a package that calculates the photonic bands for periodic system based on Fourier transform. MPB is usually used for fast parameter sweeping under a coarse structural resolution. COMSOL is based on finite element method, which is used for accurate characterization of the Eigen frequencies, especially when the mesh need to be matched between the Eigen value study and the full-wave study.

2.1.1.2 Full-wave study

After identifying the Eigen modes, we can implement full-wave study to emulate a realistic optical manipulation setup. The full-wave study is driven by current source $\boldsymbol{J}$. For Eq.2.6 and Eq.2.7, the frequency ω is chosen according to the dispersion relation of the Eigen modes, and the configuration of the current source $\boldsymbol{J}$ is chosen according the symmetry/field distribution of the Eigen modes that one wants to excite.

The regular simulation domain is terminated by Perfect Matching Layers (PML) that are impedance matched, while gradually introducing loss into the depth[72]. As the PML is designed to absorb the field, the field is not supposed to approach the outmost boundary. Therefore the outmost boundary can be simply set as PEC ($\hat{n} \times E = 0$) for Eq.2.6 or PMC ($\hat{n} \times H = 0$) for Eq.2.7. These are either Dirichlet or Neumann boundary conditions for different field components. The PML is configured such that reflection into the regular simulation domain is suppressed below -60dB.

With the field distribution solved from full-wave study, one can calculate optical forces on objects that is placed inside the system, as well as the amplitudes and phases of scattering between the Eigen modes, in preparation for further analysis.

We use COMSOL Multiphysics[48] for the full-wave study.

2.1.2 The Finite Element Method

The finite element method is a numerical technique for obtaining approximate solutions to boundary-value problems of PDEs in engineering and mathematical physics[47], [73]. The principle of the method is to replace an entire continuous domain by a number of subdomains in which the unknown function is represented by simple interpolation functions with unknown coefficients to be solved. Thus the original boundary-value problem with an infinite number of degrees of freedom is converted into a problem with a finite number of degrees of freedom, or in other words, the solution of the entire system is approximated by a finite number of unknown coefficients. Then a system of algebraic equations is obtained by applying the Ritz variational or Galerkin procedure. Finally, solution of the boundary-value problem is achieved by solving the system of equations. Generally, a finite element analysis include the following steps: (1)

Discretization; (2) Selection of the interpolation functions; (3) Formulation of the system of equations; (4) Solution of the system of equations.

2.1.2.1 Discretization

The benefit of finite element method lies in the capability to discretize the entire domain into sub-domains (i.e. elements) that are adaptive to the structure. The mesh elements are flexible in both the shapes and sizes. The elements can take the shape of line segments in 1D, triangle or rectangles in 2D, tetrahedra, triangular prisms, or rectangular bricks in 3D. In particular, triangle and tetrahedra are best suited for irregularly-shaped domains. Smaller mesh elements are required for regions of high fineness or high index, while larger elements can be used for uniform regions with lower index. The element sizes can change gradually inside a domain.

The global function to be solved is mapped onto interpolation functions on individual elements. The interpolation functions (also known as shape functions) are expressed in terms of unknown coefficients, where the coefficients are the values of the approximated global function on the nodes associated with the element. For first order shape function, the nodes are simply taken as the vortices of the elements. For higher order shape functions, more coefficients are needed, therefore additional nodes are identified at interpolation points on the element. A complete description of a node contains its coordinate values, local index inside the element, and global index. The local index of a node indicates its position in the element, whereas the global index specifies its position in the entire system. The independent nodes consist of total degree of freedoms to be solved later in the system of equations.

2.1.2.2 Selection of interpolation functions

By discretization, the finite element method sacrifices the continuity in higher order derivatives of the solution at the element boundaries. Using linear/quadratic/cubic interpolation functions, the solution belongs to the $C^0/C^1/C^2$ class[1] respectively[74]. By default, COMSOL first solves for the $\boldsymbol{E}$ field based on the Master's equation (Eq.2.6), and then calculates the $\boldsymbol{H}$ field based on the curl relation. The continuity in both $\boldsymbol{E}$ and $\boldsymbol{H}$ are necessary for the accuracy in optical forces characterization, which requires C^1 continuity in the $\boldsymbol{E}$ field. Therefore we choose the quadratic interpolation functions in COMSOL. Using cubic interpolation function provides better accuracy but at a higher computational cost. Nonlinear optics simulation often requires cubic interpolation.

Once the order of the interpolation function is selected, we can formulate an expression for the unknown solution in an element, say element e, in the following form:

$$\varphi^e = \sum_{i=1}^{n} \phi_i^e v_i^e = \{\phi^e\}^T \{v^e\} \tag{2.12}$$

where n is the number of nodes in the element, ϕ_i^e is the element interpolation function which takes value of 1 at node i and takes value of 0 at other nodes of the element, v_i^e is the value of the approximated solution φ of the global function at node i of the element. $\{\cdot\}$ denotes a column vector.

2.1.2.3 Formulation of the system of equations

Let's consider the boundary value problem of a differential equation in a domain Ω

$$\mathcal{L}\psi = f \tag{2.13}$$

where $\mathcal{L}$ is a differential operator, ψ is the global function to be solved, f is the source term. In electromagnetics, Eq.2.13 can represent Poisson equations of the electric potential,

[1] The function f is said to be of (differentiability) class C^k if the derivatives f', f'', ..., $f^{(k)}$ exist and are continuous.

or wave equations like Eq.2.6. The boundary conditions can be periodic, Dirichlet, Neumann, impedance or radiation conditions, or even higher order conditions.

There are two classical methods to solve Eq.2.13. One is the Ritz variational method, the other is Galerkin's method. The Ritz method formulates a functional whose minimum corresponds to the differential equation under the given boundary conditions. The Galerkin's method seeks the solution by weighting the residual of the differential equation. The two methods yield the identical linear algebra under finite element method when the operator $\mathcal{L}$ is self-adjoint[2] (e.g. lossless system). Here we illustrate the procedure with Galerkin's method.

Assume that φ is an approximate solution to Eq.2.13, it results in a nonzero residual

$$r = \mathcal{L}\varphi - f \neq 0 \tag{2.14}$$

The best φ will be the one that minimizes the residual r at all points of Ω. In this vein, weighted residual methods enforce the condition

$$R = \int_{\Omega} w\, r\, d\Omega = 0 \tag{2.15}$$

where R denote weighted residual integral and w is the weight. In Galerkin's method, the weight w is selected to be the complex conjugate of φ. w is also known as the test function in COMSOL. φ and w can be expended as

$$\varphi = \sum_{j=1}^{N} \phi_j v_j = \{\phi\}^T\{v\} \tag{2.16}$$

$$w = \sum_{j=1}^{N} \phi_j v_j^* = \{\phi\}^T\{v^*\} \tag{2.17}$$

where ϕ_j are the global expansion functions defined over the entire domain and v_j are coefficients to be determined. Substituting Eq.2.16 and Eq.2.17 into Eq.2.15

$$R = \{v^*\}^T \int_{\Omega} (\{\phi\}\mathcal{L}\{\phi\}^T \{v\} - \{\phi\}f)\, d\Omega = 0 \tag{2.18}$$

[2]Self-adjoint operator $\mathcal{L}$ satisfies $\langle \mathcal{L}\phi, \psi\rangle = \langle \phi, \mathcal{L}\psi\rangle$, where $\langle \phi, \psi\rangle = \int_{\Omega} \phi\psi^* d\Omega$.

Eq.2.18 should hold for arbitrary coefficients in the test function, which leads to a linear algebra problem

$$[K]\{v\} = \{b\} \tag{2.19}$$

where

$$[K] = \int_\Omega \{\phi\}\mathcal{L}\{\phi\}^T \, d\Omega \tag{2.20}$$

$$\{b\} = \int_\Omega \{\phi\} f \, d\Omega \tag{2.21}$$

The matrix $[K]$ is not necessarily symmetric unless the operator $\mathcal{L}$ is self-adjoint.

As the domain is discretized into elements, the residual R can be decomposed into contributions from individual elements

$$R = \sum_{e=1}^{N_e} \overline{R^e} = \sum_{e=1}^{N_e} \left\{\overline{v^{e*}}\right\}^T \left([\overline{K^e}]\{\overline{v^e}\} - \left\{\overline{b^e}\right\}\right) = 0 \tag{2.22}$$

where N_e is the total number of elements. $[\overline{K^e}]$ is an $N \times N$ matrix augmented from an $n \times n$ matrix $[K^e]$, where

$$K^e = \int_{\Omega^e} \{\phi^e\}\mathcal{L}\{\phi^e\}^T \, d\Omega \tag{2.23}$$

$\{\overline{v^e}\}$ and $\left\{\overline{b^e}\right\}$ are $N \times 1$ column vectors augmented from $n \times 1$ column vectors $\{v^e\}$ and $\{b^e\}$, where

$$\{b^e\} = \int_{\Omega^e} \{\phi^e\} f \, d\Omega \tag{2.24}$$

Augmenting the deterministic quantities $[K^e]$ and $\{b^e\}$ into $[\overline{K^e}]$ and $\left\{\overline{b^e}\right\}$ involves padding 0s. While v^e is the unknown, the augmented version $\overline{v^e}$ is just $\{v\}$, the global coefficients. Now, based on the correspondence of a node in the global system and its belonging to one or multiple elements, the global expansion functions ϕ_j should be specified as the sum of element interpolation functions ϕ_i^e that take the value of 1 at the global node j, where ϕ_i^e may come from multiple elements that share the same node j. It follows that $[K]$ and $\{b\}$ are assembled by summing up the nonzeros from individual elements

$$[K] = \sum_{e=1}^{N_e} [\overline{K^e}] \tag{2.25}$$

$$\{b\} = \sum_{e=1}^{N_e} \{\overline{b^e}\} \tag{2.26}$$

Before the system of equations Eq.2.19 are ready for solving, we need to apply the boundary conditions. For example, periodic boundary condition reduces some degree of freedom by specifying the dependence between nodes at periodic boundaries. Dirichlet boundary condition reduces some degree of freedom by specifying their value explicitly. Neumann boundary condition, which requires the normal derivative to vanish at the boundary, is usually satisfied implicitly and automatically in the solution process.

2.1.2.4 Solution of the system of equations

The assembled system of equations take one of the two forms:

$$[K]\{v\} = \{b\} \tag{2.27}$$

or

$$[A]\{v\} = \lambda[B]\{v\} \tag{2.28}$$

Eq.2.27 corresponds to the full-wave study that has a source term $\{b\}$. Eq.2.28 corresponds to the source-free Eigen value study. In this case, the matrix $[K]$ can be written as $[A] - \lambda[B]$, where λ is the Eigen value. Once we find $\{v\}$, we can use Eq.2.16 to construct the field distribution.

2.2 Optical Forces Calculation

2.2.1 Maxwell Stress Tensor

Optical forces can be calculated by integrating the Maxwell Stress Tensor (MST) over a surface enclosing the object.

$$\boldsymbol{F} = -\int_S \overleftrightarrow{T} \cdot \boldsymbol{n}\, ds \tag{2.29}$$

$$\overleftrightarrow{T}_{ij} = \epsilon E_i E_j - \frac{1}{2}\delta_{ij}E^2 + \frac{1}{\mu}\left(B_i B_j - \frac{1}{2}\delta_{ij}B^2\right) \tag{2.30}$$

$$i, j \in \{x, y, z\}$$

where $\boldsymbol{n}$ is an *inward* normal vector, $\overleftrightarrow{T}$ is the Maxwell Stress Tensor.

There are several variations in the force calculation derived from MST. Here we verify the agreements between the variations and choose the one that is the most accurate for a given computational budget. We limit our discussion to dielectric/metallic, lossless/lossy objects that have the permeability $\mu = \mu_0$, which cover the needs of Chapter 2-6.

Integrating MST over an additional surface enclosing the object requires fine mesh on the surface. One can instead integrate a pressure over the object's surface. Consider the pressure on the surface from the outside (domain 1) to the inside (domain 2) of the object. The normal vector $\boldsymbol{n}$ points from domain 1 to domain 2. The surface pressure is expressed as[3]

$$\boldsymbol{p} = \left(\overleftrightarrow{T}_2 - \overleftrightarrow{T}_1\right) \cdot \boldsymbol{n} \tag{2.31}$$

As we have taken $\mu_1 = \mu_2 = \mu_0$, the magnetic part in $\overleftrightarrow{T}$ do not contribute to $\boldsymbol{p}$ due to the continuity. We only need to consider the $\boldsymbol{E}$ component

$$T_{ij} n_j = \epsilon E_n E_i - \frac{1}{2}\epsilon E^2 n_i$$

$$\overleftrightarrow{T} \cdot \boldsymbol{n} = \epsilon E_n \boldsymbol{E} - \frac{1}{2}\epsilon E^2 \boldsymbol{n} = \epsilon(E_n^2 \boldsymbol{n} + E_n E_t \boldsymbol{t}) - \frac{1}{2}\epsilon(E_n^2 + E_t^2)\boldsymbol{n}$$

$$= \frac{1}{2}\epsilon E_n^2 \boldsymbol{n} - \frac{1}{2}\epsilon E_t^2 \boldsymbol{n} + \epsilon E_n E_t \boldsymbol{t}$$

Using the following relations

$$E_{1t} = E_{2t} = E_t, \qquad \epsilon_1 E_{1n} = \epsilon_2 E_{2n} = D_n$$

The surface pressure becomes

$$\boldsymbol{p} = \frac{1}{2}(\epsilon_2 E_{2n}^2 - \epsilon_1 E_{1n}^2)\boldsymbol{n} - \frac{1}{2}(\epsilon_2 E_t^2 - \epsilon_1 E_t^2)\boldsymbol{n} = \frac{1}{2} D_n^2 \left(\frac{1}{\epsilon_2} - \frac{1}{\epsilon_1}\right)\boldsymbol{n} - \frac{1}{2} E_t^2 (\epsilon_2 - \epsilon_1)\boldsymbol{n} \tag{2.32}$$

The total force on the object is calculated as

[3] $\overleftrightarrow{T}_1$ and $\overleftrightarrow{T}_2$ are evaluated at the same boundary in the finite element mesh system. At material boundary, finite element method maintains separate quantities for the two sides.

$$\boldsymbol{F} = \int_S \boldsymbol{p}\, ds \tag{2.33}$$

For a 2D system (uniform in the z-direction) with TM polarization, the forces on a uniform object in air can be further transformed into the volume integration of Lorentz force on the polarization current $\boldsymbol{J}_p$.

$$\begin{aligned}
\boldsymbol{F} &= (\epsilon_2 - \epsilon_1) \int_S \frac{1}{2} E_z^2 (-\boldsymbol{n}) ds = \left(\epsilon_{obj} - \epsilon_{air}\right) \int_V \frac{1}{2} \nabla\left(E_z^2\right) da \\
&= \left(\epsilon_{obj} - \epsilon_{air}\right) \int_V \frac{1}{2} \nabla(\boldsymbol{E} \cdot \boldsymbol{E}) da = \left(\epsilon_{obj} - \epsilon_{air}\right) \int_V \boldsymbol{E} \times (\nabla \times \boldsymbol{E}) da \\
&= -\left(\epsilon_{obj} - \epsilon_{air}\right) \int_V \boldsymbol{E} \times \frac{\partial \boldsymbol{B}}{\partial t} da = \int_V i\omega\left(\epsilon_{obj} - \epsilon_{air}\right) \boldsymbol{E} \times \boldsymbol{B} da = \int_V \boldsymbol{J}_p \times \boldsymbol{B} da
\end{aligned} \tag{2.34}$$

To verify the agreements between the different approaches of calculating optical forces (Eq.2.29, Eq.2.33 and Eq.2.34), we setup a simple test case (Fig.2.1). The test case is in 2D, which covers the scenarios encountered from Chapter2 to Chapter 6. A cylindrical particle is placed inside a PEC box. The surrounding media is air. There is a current source that can excite TE or TM polarization. The theoretical value of the optical forces on the particle is of less concern here, as the goal is to verify the agreement between different approaches. We test 3 cases: TE polarization with a lossless particle ($\epsilon_r = 3.9$); TM polarization with a lossless particle ($\epsilon_r = 3.9$); TM polarization with a lossy particle ($\epsilon_r = 3.9 + 1i$). In all cases $\mu_r = 1$. The numerical agreement on the forces between the different approaches is to the 4th significant digit (Table 2.1) using the mesh shown in Fig.2.1 and is improved to the 5th significant digit (Table2.2) as we reduce the mesh size by 3x from Fig.2.1. Without loss of generality, these approaches to calculate the optical forces also apply to metallic particles ($Re\{\epsilon_r\}$<0).

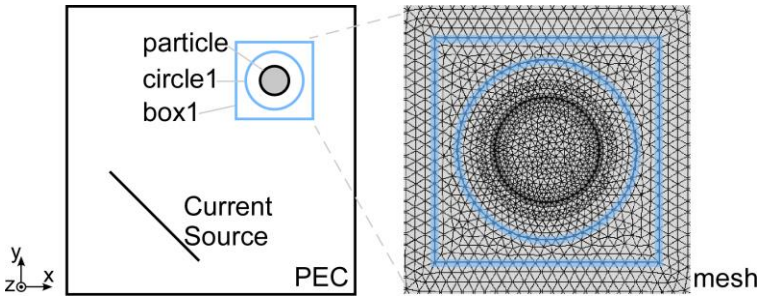

Figure 2.1: Schematics to test the optical forces calculation from varies approaches derived from the Maxwell Stress Tensor. A cylinder (grey disk, $\epsilon_r = 3.9$ or 3.9+1i, $\mu_r = 1$) is placed inside a PEC box. Two virtual surfaces (blue colored) enclosing the cylinder are finely meshed for testing the MST integration. The line current source can excite TE or TM field.

	TE $\epsilon_r = 3.9$		TM $\epsilon_r = 3.9$		TM $\epsilon_r = 3.9 + 1i$	
	Fx (N/m)	Fy (N/m)	Fx (N/m)	Fy (N/m)	Fx (N/m)	Fy (N/m)
Lorentz	NA	NA	2.73139e-8	-7.97213e-10	2.69458e-8	9.14726e-10
Surf_p	9.78706e-7	1.09553e-7	2.73139e-8	-7.97214e-10	NA	NA
MST c1	9.78726e-7	1.09557e-7	2.73135e-8	-7.97263e-10	2.69455e-8	9.14655e-10
MST b1	9.78721e-7	1.09537e-7	2.73138e-8	-7.97208e-10	2.69457e-8	9.14727e-10

Table 2.1: Optical forces on the cylinder in Fig.2.1 for varies setups and from varies approaches. Lorentz: integrating the Lorentz force over the volume of the cylinder based on Eq.2.34. Surf_p: integrating the surface pressure over the surface of the cylinder based on Eq.2.33. MST c1/b1: integrating the MST over circle 1 / box 1 denoted in Fig.2.1 based on Eq.2.29. The mesh is shown in Fig.2.1.

	TE $\epsilon_r = 3.9$		TM $\epsilon_r = 3.9$		TM $\epsilon_r = 3.9 + 1i$	
	Fx (N/m)	Fy (N/m)	Fx (N/m)	Fy (N/m)	Fx (N/m)	Fy (N/m)
Lorentz	NA	NA	2.73138e-8	-7.97214e-10	2.69458e-8	9.14725e-10
Surf_p	9.78721e-7	1.09536e-7	2.73139e-8	-7.97215e-10	NA	NA
MST c1	9.78722e-7	1.09536e-7	2.73138e-8	-7.97214e-10	2.69458e-8	9.14723e-10
MST b1	9.78722e-7	1.09535e-7	2.73138e-8	-7.97214e-10	2.69458e-8	9.14725e-10

Table 2.2: Optical forces on the cylinder in Fig.2.1 for varies setups and from varies approaches. The setup is identical to Table 2.1 but the mesh size is decreased by 3x.

Integrating over a volume provides better numerical stability for given computational budget, because it involves more degrees of freedom than integrating over a surface. Comparing Table 2.1 with Table 2.2, the Lorentz forces, which is integrated over

the volume, yields the most stable results for two different mesh qualities. MST integrated over the outer box is the second most stable, however it complicates the meshing. When situations permit, our first choice is to integrate the Lorentz force over the volume. In the rest of the dissertation, we use MST to refer to all the variations being tested in this section, as they are all derived from MST.

2.2.2 Response Theory of Optical Forces

Response theory of optical forces (RTOF) establishes a new approach of deriving optical forces in mechanically variable photonic systems consisting of linear media [42]. Through energy and photon-number conservation, it was shown that the power and phase responses of the system versus the mechanical coordinate of interest are sufficient to compute the optical forces. Optical forces can be designed purely based on the responses, while independent of the construction of the underlying device or its field distribution.

RTOF is derived from virtual work principle in the adiabatic limit[4][42]. Suppose the object makes a displacement, introducing an exchange of energy with the optical field. The exiting photons accumulate shifts in their phases, as their frequencies were altered by the energy exchange (i.e. Doppler effect). The power of the exiting photons also have a response to the displacement, but its derivative versus the displacement is of higher order contribution to the energy exchange compared to the phase response term. As a simplest example, for a mirror displaced by δq (Fig.2.2), under steady state approximation, the work being done to the mirror is

$$F_{opt} \cdot \delta q \approx -\int_{t_i}^{t_f} \hbar \Phi \delta \omega dt \approx \hbar \Phi \left(\psi_f - \psi_i\right) \tag{2.35}$$

[4] The mechanical motion involves a time-scale that is much longer than the photon life time.

where $\hbar$ is the Planck constant, Φ is the phonon number flux, $\delta\omega$ is the change in photon frequency due to the virtual work. Rearranging Eq.2.35, it is found that the force on the mirror is

$$\boldsymbol{F}_{opt} = \frac{I}{\omega}\frac{d\psi}{d\boldsymbol{x}} \tag{2.36}$$

where I is the power, ω is the angular frequency.

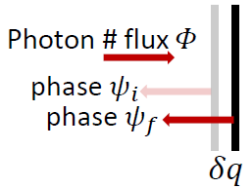

Figure 2.2: Response in the phase of reflected photons due to the displacement of a mirror

A mode leaving the system is referred to as a 'port'. The example in Fig.2.2 only have one port, the reflected plane wave. Integrated photonic system usually involves multiple ports, where RTOF can be generalized by simply summing up the contributions from each port

$$\boldsymbol{F}_{opt} = \Sigma_i \frac{I_i}{\omega_i}\nabla\psi_i \tag{2.37}$$

It should be noticed that the transmission and reflection of the same mode are counted as 2 ports. Also, a port is identified with a single frequency. To treat a broadband source, a continuous integral over the frequency is needed.

Response theory provide rich insights into tailoring the optical forces. A one-port system have conservative optical forces, because the gradient of a scalar ψ is cur-less. Integrated photonic systems are usually multi-port, which indicates non-conservative[43] optical forces. In some special cases, one can decompose the forces into conservative and non-conservative components and enhance the conservative part using resonances (Section

2.3). One can also exploit the non-conservativeness to design optical motors around phase singularity (Chapter 6). On the other hand, one can use RTOF to predict properties of longitudinal forces (Chapter 3, 4) or the transverse forces (Chapter7) in waveguides, based on the dispersion relation and other properties of the Eigen modes.

2.3 Example Workflow to Characterize Optical Forces in Photonic Crystal

In this section we demonstrate the workflow from electromagnetic simulation to optical forces characterization, with an example model. We study a system that consists of a cavity side-coupled to a single-mode photonic crystal defect waveguide (Fig.2.3), with a particle inside the cavity experiencing optical forces. Experimental works had demonstrated optical trapping in such a system [75]. This system is more interesting theoretically because the forces can be decomposed into conservative and non-conservative components, where only the conservative component can be enhanced by resonance. One can further adjust the shape of the optical potential by tuning the operating frequency.

In order to apply response theory to predict optical forces, one should be able to predict the responses in the first place. It had been demonstrated that such an optical resonance system can be modeled by temporal coupled-mode theory [45], [76], [77], which provides a full description of the responses in terms of a few system parameters. As a result, we can apply response theory to predict the force fields.

This section is arranged as follows: We first introduce the theoretical model description using coupled-mode theory (Section 2.3.1). We then show necessary steps in setting up the frequency domain simulation (Section 2.3.2). Finally, we show optical forces analysis using response theory. The response theory is accurate even when the forces are enhanced by orders of magnitudes (Section 2.3.3).

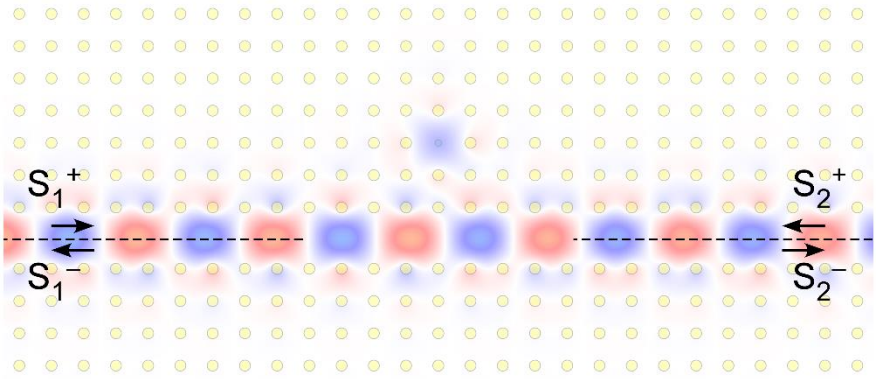

Figure 2.3: A single-mode cavity side coupled to a single-mode waveguide. A particle (blue disk) inside the cavity can move around and experience optical forces.

2.3.1 Model Description

Fig.2.3 illustrates a lossless system with two ports and a side-coupled resonator. s_1^+ and s_2^+ are the amplitudes of the incoming waves from the two ports. s_1^- and s_2^- are the amplitudes of the outgoing waves. Temporal coupled-mode theory[45], [76], [77] describes the system as

$$\frac{dA}{dt} = (-j\omega_0 - 1/\tau_1 - 1/\tau_2)A + [\kappa_1 \quad \kappa_2]\begin{bmatrix} s_1^+ \\ s_2^+ \end{bmatrix} \tag{2.38}$$

$$\begin{bmatrix} s_1^- \\ s_2^- \end{bmatrix} = C\begin{bmatrix} s_1^+ \\ s_2^+ \end{bmatrix} + \begin{bmatrix} d_1 \\ d_2 \end{bmatrix} A \tag{2.39}$$

where A is the amplitude of the resonance-mode, with $e^{-j\omega t}$ dependency[5], $\kappa_{1,2}, d_{1,2}$ are the coupling rates between ports and the cavity. C is the scattering matrix for the direct transport process, which takes the form[45]

$$C = e^{j\phi}\begin{bmatrix} -jr & t \\ t & -jr \end{bmatrix} \tag{2.40}$$

where $r, t, \phi \in \mathbb{R}$ and $r^2 + t^2 = 1$. By choosing the location of reference planes, we can set $\phi = 0$. The total scattering matrix S is defined as

$$\begin{bmatrix} s_1^- \\ s_2^- \end{bmatrix} = S\begin{bmatrix} s_1^+ \\ s_2^+ \end{bmatrix} \tag{2.41}$$

[5] References [45], [76], [77] used the $e^{j\omega t}$ convention. Here to be consistent with the rest of the dissertation, we use the $e^{-j\omega t}$ convention.

$$S = C + \frac{|d\rangle\langle\kappa|^*}{j(\omega_0-\omega)+\frac{1}{\tau_1}+\frac{1}{\tau_2}} \tag{2.42}$$

It had been demonstrated [45], [76] that under time reversal symmetry

$$C|d\rangle^* = -|d\rangle \tag{2.43}$$

Under energy conservation and time reversal symmetry

$$|\kappa\rangle = |d\rangle \tag{2.44}$$

Energy conservation also indicates

$$\frac{2}{\tau} = \frac{2}{\tau_1} + \frac{2}{\tau_2} = d_1^* d_1 + d_2^* d_2 \tag{2.45}$$

Separating Eq.2.45 into individual contributions of the 2 ports, we have

$$\frac{2}{\tau_1} = d_1^* d_1,\ \frac{2}{\tau_2} = d_2^* d_2 \tag{2.46}$$

Without loss of generality

$$\kappa_1 = d_1 = \sqrt{\frac{2}{\tau_1}} e^{i\phi_1},\ \kappa_2 = d_2 = \sqrt{\frac{2}{\tau_2}} e^{i\phi_2} \tag{2.47}$$

In our system, we have $r \to 0,\ t \to 1$, together with Eq.2.43 and Eq.2.45 we can get

$$\tau_1 = \tau_2 = 2\tau \tag{2.48}$$

$$\phi_1 + \phi_2 = (2N+1)\pi \tag{2.49}$$

Eq.2.48 agrees with the bounds $\frac{1-r}{1+r} \le \frac{\tau_1}{\tau_2} \le \frac{1+r}{1-r}$ proved by reference [77]. In Eq.2.49 we can set $N = 0$ without loss of generality. Putting together Eq.2.40-2.49 and making the substitution $2\phi_1 - \pi = -\phi_{11}$, we find

$$S_{11} = \frac{-\frac{1}{\tau}e^{-i\phi_{11}}}{j(\omega_0-\omega)+\frac{1}{\tau}} \tag{2.50}$$

$$S_{21} = \frac{j(\omega_0-\omega)}{j(\omega_0-\omega)+\frac{1}{\tau}} \tag{2.51}$$

Assume the incident light comes in from the left hand side (port 1). Using RTOF, the optical forces on the particle is given by

$$\boldsymbol{F} = \sum_i \frac{I_i}{\omega} \nabla \psi_i = \frac{I_{in}}{\omega} |S_{11}|^2 \nabla(\angle S_{11}) + \frac{I_{in}}{\omega} |S_{21}|^2 \nabla(\angle S_{21}) \tag{2.52}$$

where the gradient ∇ is taken versus the particle's coordinate. ω_0, τ, ϕ_{11} are determined by the particle's coordinate. Once we find ω_0, τ, ϕ_{11} from simulation, the force fields can be fully described.

2.3.2 Frequency Domain Studies

In order to find the proper configuration and operating frequency, we need to individually characterize the Eigen frequencies of the cavity and the waveguide. There are several requirements to be fulfilled through adjusting the configurations. For the cavity, it's desirable that it has a single resonance mode in the middle of the bulk bandgap, which leads to a large quality factor. The waveguide should have a single mode around the resonance frequency of the cavity, in order to excite the cavity mode, and be consistent with the 2-port model derived above. It's desirable that the waveguide mode has a large group velocity, which requires thinner PML layer.

We choose to use the TM polarization, as it provides a complete bandgap between the first and 2nd bulk band[14]. The dielectric property of the rods is given ($\epsilon_r = 11.56$). The first step is to adjust the radius of the rods until the resonance is in the middle of the bandgap. It should noticed that the particle ($\epsilon_r = 3.9,\ r = 0.1a$) is part of the cavity (Fig.2.4a), its displacement introduces changes to the resonance frequency (Fig.2.4b). The proper cavity mode is found when the rods have radius $r = 0.169a$. Now the property of the bulk photonic crystal is fixed. Next we adjust the width of the line defect waveguide. A proper dispersion relation (Fig.2.4d) of the waveguide mode is found when the distance between the 2 rows of rods is enlarged by $0.9a$ (Fig.2.4c).

For Eigen value study, periodic boundary condition is applied on the dashed lines shown in Fig.2.4(a)(c).

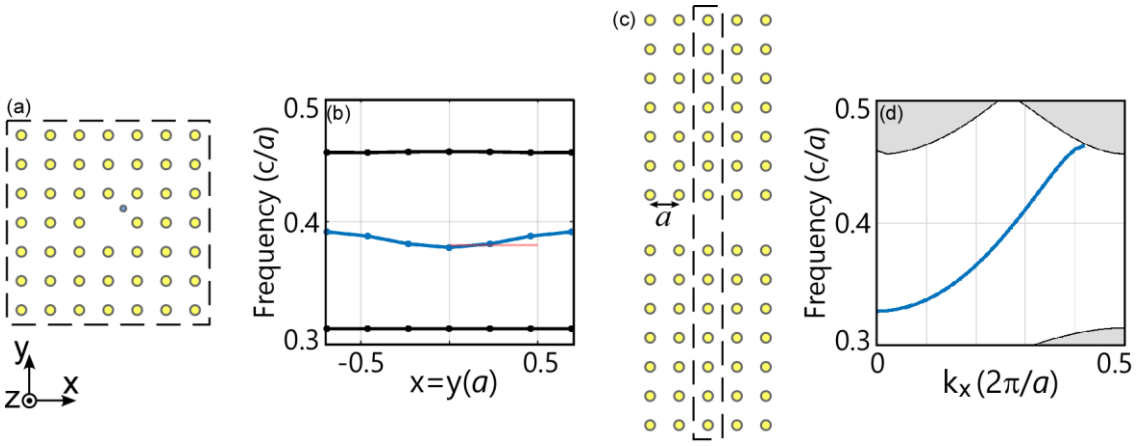

Figure 2.4: Eigen value studies to characterize the Eigen frequencies of the photonic crystal point defect cavity and line defect waveguide. The photonic crystal is made of dielectric rods ($\epsilon_r = 11.56,\ r = 0.169a$), where a is the lattice constant. (a) A cavity is created by removing one rod from the photonic crystal. A dielectric particle ($\epsilon_r = 3.9,\ r = 0.1a$) is placed inside the cavity. (b) Resonance frequency of the cavity (TM polarization) versus the particle's location (blue curve). The black curves indicate the band-edge of the upper and lower bulk bands. (c) A line defect waveguide is created by enlarging the distance between two rows of rods. The defect size is $d = 1.9a$ by measuring the center-to-center distance between the rows of rods that are nearest to the defect. (d) Dispersion relation (TM polarization) of the waveguide mode (blue curve) in the bulk bandgap (white area). k_x is the Bloch k.

Full-wave study is conducted to find the field distribution when the cavity is coupled to the waveguide, which allows us to find the parameters needed by the coupled mode theory, and to predict / verify the optical forces experienced by the particle. The light comes in from the left hand side (port 1), driven by a current source. To verify the agreement between the Eigen value study and the full-wave study, we operate at $f = 0.38c/a$ and move the particle along the line $x = y$. The cavity becomes on resonance when the particle is at $x = y = 0.15$ and off resonance elsewhere (Fig.2.5), which is consistent with the trend of resonance frequencies versus location from the Eigen value study (red line in Fig.2.4).

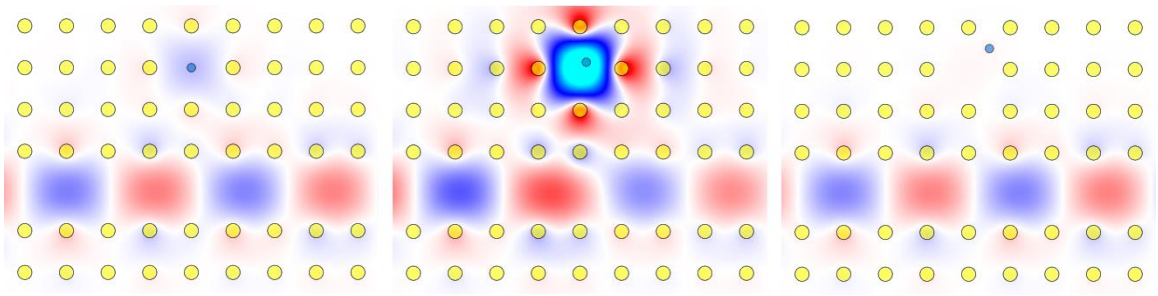

Figure 2.5: The cavity being off/on/off resonance for the particle located at $x = y = 0$; $x = y = 0.15a$ and $x = y = 0.5a$. $\omega = 0.38 \cdot 2\pi c/a$

2.3.3 Optical Forces Analysis

In order to use response theory (RTOF) combined with coupled mode theory (CMT) (Eq.2.50-2.52) to characterize the optical forces, we need to find the system parameters ω_0, τ, ϕ_{11} from the full-wave simulation. We sweep the particle over spatial grid points. At each grid point, ω_0, τ, ϕ_{11} are found (Fig.2.6) from curve fitting S_{11}, S_{21} versus the operating frequency. S_{11} and S_{21} are found from curve fitting sinusoidal waves to the E_z field along the black dashed lines shown in Fig.2.3. The sampling of E_z field is taken from points separated by the lattice constant a, in order to avoid the oscillations caused by the unit cell function.

ω_0, τ, ϕ_{11} are obtained with spatial resolution of $0.06a$ for the off-resonance case (Fig.2.7a) and with spatial resolution of $0.005a$ for the on-resonance case (Fig.2.7b). These parameters are interpolated into spatial resolution of $0.00001a$ to compute the gradients required by Eq.2.52. The forces predicted from RTOF&CMT agrees well with the MST calculated forces, for both the off-resonance case (Fig.2.7a) and the on-resonance case (Fig.2.7b).

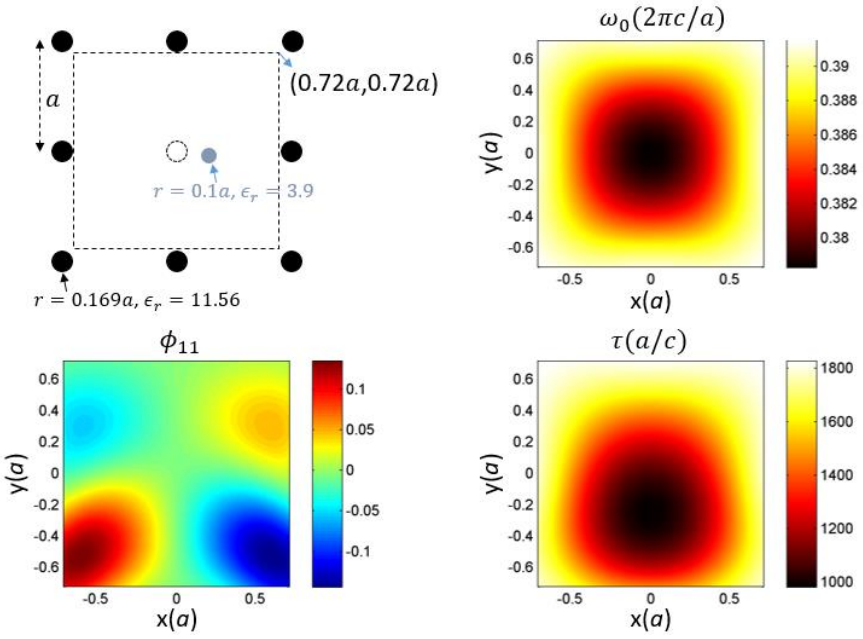

Figure 2.6: System parameters versus the location of the particle.

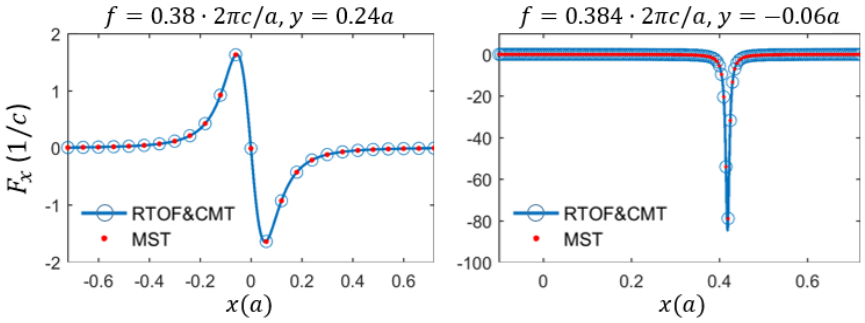

Figure 2.7: Forces calculated from response theory combined with coupled mode theory agrees well with the forces calculated from Maxwell Stress Tensor. The forces are normalized to 1W of incidence power.

As we have demonstrated that the theoretically predicted forces from RTOF&CMT are numerically accurate, we can further analyze the properties of the force fields from theoretical approach.

The total forces can be decomposed into the conservative and non-conservative components, which have different scaling versus the photon lifetime. Consider the phases in the 2 ports without constants

$$\angle S_{11} = -\phi_{11} - \text{atan}[\tau(\omega_0 - \omega)] \tag{2.53}$$

$$\angle S_{21} = -\text{atan}[\tau(\omega_0 - \omega)] \tag{2.54}$$

The phases share a common part

$$\psi = -\text{atan}[\tau(\omega_0 - \omega)] \tag{2.55}$$

Therefore the total forces can be decomposed (Fig.2.8) into a conservative component ($\boldsymbol{\nabla} \times \boldsymbol{F}_C = \boldsymbol{0}$) associated with the common phase ψ, and a non-conservative component ($\boldsymbol{\nabla} \times \boldsymbol{F}_{NC} \neq \boldsymbol{0}$) associated with the difference in the phases, ϕ_{11}.

$$\boldsymbol{F} = \boldsymbol{F}_C + \boldsymbol{F}_{NC} \tag{2.56}$$

$$\boldsymbol{F}_C = \frac{I_{in}}{\omega} \nabla\psi \tag{2.57}$$

$$\boldsymbol{F}_{NC} = \frac{I_{in}}{\omega} \frac{\nabla(-\phi_{11})}{1+\tau^2(\omega-\omega_0)^2} \tag{2.58}$$

From Fig.2.8 we find the maximum of conservative forces is 500x stronger than the maximum of the non-conservative forces. A brief analysis is as follows. The maximum of both $|\boldsymbol{F}_C|$ and $|\boldsymbol{F}_{NC}|$ are reached when the particle is positioned at $\omega_0(\boldsymbol{x}) = \omega$. The ratio between the maximum is

$$\frac{\max|\boldsymbol{F}_C|}{\max|\boldsymbol{F}_{NC}|} = \tau \frac{|\nabla\omega_0|}{|\nabla\phi_{11}|} \tag{2.59}$$

Eq. 2.59 indicates at a given frequency, the conservative forces scale up with photon lifetime τ, while the non-conservative forces do not. Therefore by enhancing the resonances (i.e. increasing the quality factor), only the conservative force is enhanced, which leads to applications such as particle trapping[78].

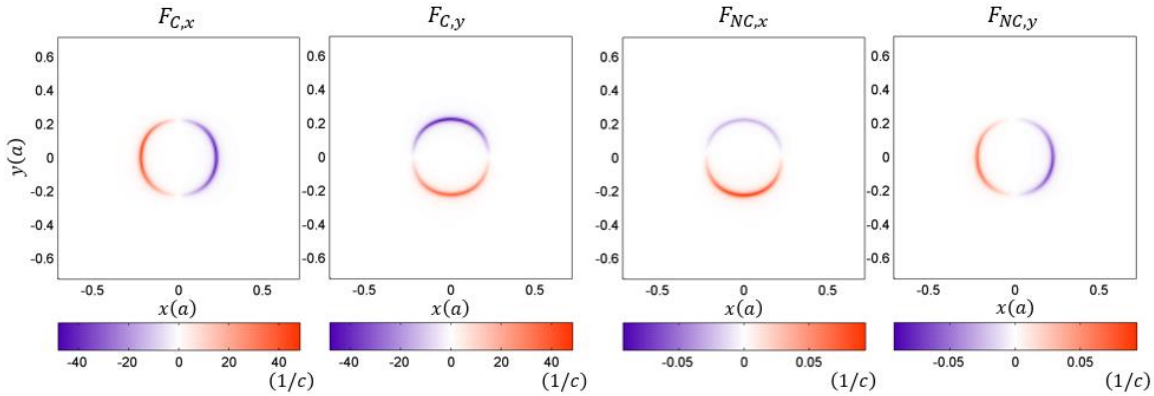

Figure 2.8: Decomposed conservative and non-conservative components of optical forces, based on RTOF. The operational frequency is $\omega = 0.38 \cdot 2\pi c/a$. The forces are normalized to 1W of incidence power.

The conservative component in the optical forces is associated with an optical potential Φ, where $\boldsymbol{F}_C = \frac{I_{in}}{\omega}\nabla\psi = -\nabla\Phi$, which leads to $\Phi = -\psi\frac{\omega}{I_{in}}$. The shape of the potential can be adjusted by tuning the operating frequency (Fig.2.9). The wall of the potential well is located at $\omega_0(\boldsymbol{x}) = \omega$. Reducing the operating frequency ω shrinks the area of the potential well without reducing the depth. Only when $\omega < \min\omega_0$, the potential well disappears.

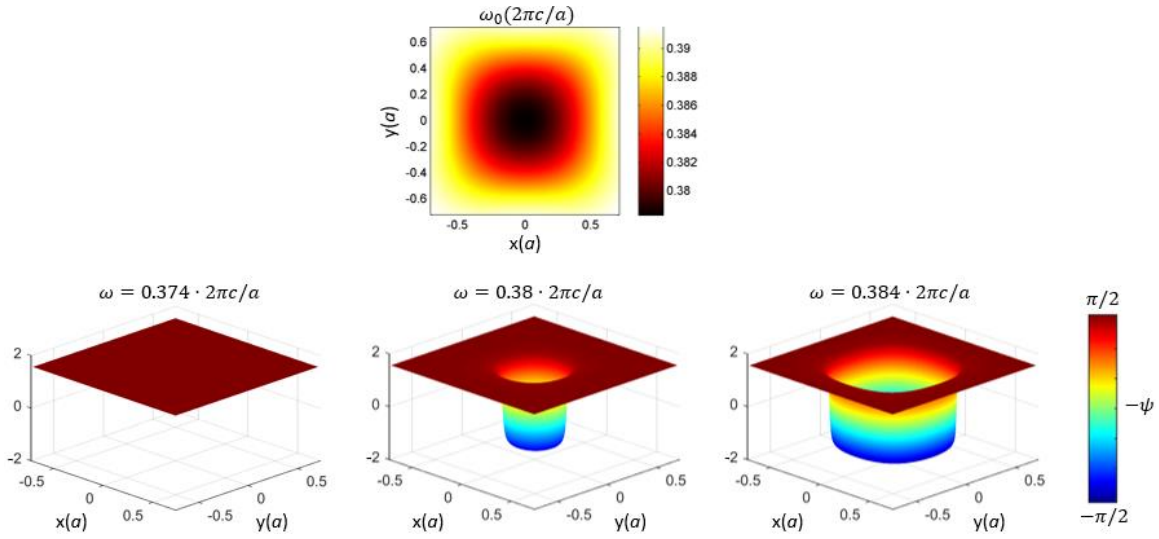

Figure 2.9: Based on RTOF, the conservative component of the optical forces is governed by an optical potential, which is determined by the common phase response ψ of the two ports (Eq.2.55). The shape of the optical potential differs for different operating frequencies ω. When the particle is located at the π phase jump in ψ, the cavity is on resonance, satisfying $\omega_0(x, y) = \omega$.

As a summary, we have demonstrated a reliable workflow from electromagnetic simulation to optical forces characterization. In particular, Response Theory of Optical Forces[42] provides intuition in predicting the optical forces, and stays accurate even when the forces are enhanced by orders of magnitude on resonance. RTOF will be applied to various systems in the following chapters.

Chapter 3: Topologically Protected Photonic Pulling Forces

3.1 INTRODUCTION

Photonic pulling force is an unusual phenomenon where a light source attracts illuminated objects over a distance significantly greater than a few wavelengths[37]. It is unique because none of the well-understood optical forces can be pulling through the entire beam: The gradient forces attract dielectric particles to and repel metallic particles away from the intensity maxima. The radiation pressure typically pushes objects away from the light source. In ordinary optical tweezers, the transportation of particles in arbitrary directions requires spatial modulation that tunes the locations of gradient traps[1], where the gradient forces have to dominate over the positive radiation pressure for the stability of manipulation. However, if we can devise continuous and stable pulling forces over the entire range of a gradientless beam, it would allow stable forward and backward transportation using a single light source without instantaneous spatial modulation. Moreover, if complex trajectories can be configured for the pulling forces, it would further improve the flexibility of optical manipulation at micro- and nano- scales.

Obtaining photonic pulling forces is a challenge from the momentum conservation perspective. According to Maxwell's electromagnetic theory, propagating light carries momentum flow in the direction of Poynting vector[44]. When light impinges on a particle, reciprocity governs that reflections naturally occur, which leads to positive momentum transfer and pushing forces on the particle. In addition, absorption also leads to positive momentum transfer and pushing forces. Generally speaking, pulling forces can only be achieved by introducing forward scattering (Fig.3.1) that increases the projected photon momentum along the axial direction[37], [49]–[60]. Forward scattering is a rare phenomenon because it requires special profile of the incident light and special form of light-matter interaction.

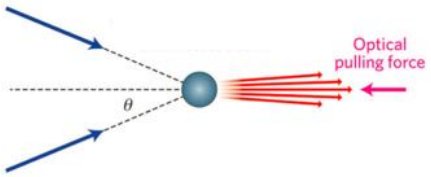

Figure 3.1: (adopted from [49]) Forward scattering that increases the axial photon momentum and generates optical pulling forces.

Early works to realize forward scattering and pulling force are typically limited to free space. These includes using large angle incidence such as multiple oblique Gaussian beams[50], [51] or a Bessel beam[52]–[60], using interface aided diffraction[79]–[81], and using negative radiation pressure localized to part of the cross section in a globally forward propagating field[82]. Special particles have also been used to aid the forward scattering, such as those with chirality[59], [60], [83] or gain media[84], [85]. Lastly, photophoretic effects[86]–[88] can also be applied to generate pulling forces. However, free space pulling forces are generally inefficient to launch. Gaussian beams have low efficiency of intensity focus. The Bessel beam requires a large source facet and is still subject to diffraction over long distance. Forward scattering in free space usually requires the particle to support dipole, quadrupole and even higher order interactions in the Mie regime[50]–[57], [59], [83], [84]. Despite the complicate setups, the trajectories of the realized pulling force are still simple, i.e. straight lines or curves prescribed by an Airy beam[89].

Unlike in free space, realizing optical pulling force in guided-wave systems offers significant benefits: light fields can be tightly confined in the transverse direction to a sub-wavelength scale to enhance field intensity and to reduce footprint; photonic waveguides can be constructed along complex trajectories to facilitate large scale integration, and can form beam splitters and interferometer for additional functionalities such as sorting and assembly; guided wave systems typically operates in the single-mode or few-mode regime,

eliminating the need and cost to synthesize exquisite light fields necessary for pulling forces to occur; guided-wave optical pulling forces could have promising applications in integrated photonics[90], such as microfluidic channels[91].

There are several works that have achieved long range pulling forces in guided wave systems. For example, people have proposed to use a ring resonator side-coupled to a dielectric waveguide [61]. The ring resonator minimizes the reflection, and can scatter a mode of smaller momentum into another mode of larger momentum. Momentum conservation indicates that the ring-resonator experiences a pulling force. However, this approach doesn't apply to arbitrary particles. Meanwhile, people have proposed to use negative index waveguides[24], [25] to get unconventional negative radiation pressure on arbitrary particles. For negative index modes, the reflection of photon corresponds to forward scattering in k space (Chapter 4.1), which agrees with the negative radiation pressure. However, these negative index modes coexist with positive index modes at the same frequency. The positive index modes have overlaps in the lateral field distribution with the negative index modes and are hard to be removed by dispersion engineering, which hinders experimental excitation of the pure negative index mode. In addition, none of these guided-wave approaches are compatible with complex trajectory. Can we get more robust forward scattering and photonic pulling forces that incorporate both arbitrary particles and complex trajectories?

Recently it had been demonstrated that the propagation of light can be topologically protected against back-scattering in photonic crystal systems, even when large structural disorders are present along the path [92]–[94]. The topology is associated with quantized behavior of the wave functions of bulk photonic crystals on its entire dispersion band, and is invariant under continuous deformations [92]. The topology determines the robustness of certain edge states on the surface of the bulk crystal, which is inherently invariant under

deformations and disorders. One class of such topologically protected light is called photonic Chiral Edge States (CESs), also known as photonic one-way modes [17], [29](Section 3.1.1). The CES propagates unidirectionally along the edge of a photonic crystal that exhibits non-trivial topological phase under broken time reversal symmetry. The CES is highly non-reciprocal, because modes along the opposite direction do not exist (Fig.3.3a). In particular, the fields can continuously navigate around obstacles (Fig.3.3b) and through sharp corners (Fig.3.12), which easily extends to complex trajectories.

Our work extends the topological protection of light propagation to topological protection of photonic forces for the first time. In particular, we exploit the topological protection to generate robust photonic pulling forces in guided-wave systems. Because CESs (i.e. one-way modes) are protected against reflection, the incident photons in a state of smaller wavenumber k must scatter forward into a state of larger k, provided that the state of larger k exists, regardless of the properties of the scattering particle, and regardless of the trajectories defined by the waveguide. The forward scattering leads to topologically protected photonic pulling forces. Based on this idea, we demonstrate pulling forces in a one-way waveguide supporting two one-way modes that have different wavenumbers (Section 3.2). The pulling forces exhibit robustness against particles with arbitrary shapes, sizes, permittivity, clusters of particles and sharp corners, and is scalable for different wavelengths (Section 3.4).

One need to be careful when predicting the scattering forces in periodic system, such as the photonic crystal that we use for realizing CESs. In free space, the relation between forward scattering and pulling forces were based on linear momentum conservation. However, in photonic crystal waveguides, the definition of linear momentum is more complicated due to the periodic nature of the wave function and the momentum conservation only predicts the sum of forces on the scatterer and forces distributed to the

near field (e.g. the photonic crystal rods), but not the individual force on each object (Chapter 5). Moreover, a periodic system processes a periodic Bloch band diagram, which posts ambiguity on the direction of scattering. To address these challenges, we use response theory (RTOF)[42] to isolate the forces on the scatterer from the forces distributed to the near field. We also combine RTOF with the perturbation method to establish consistency between pulling forces on a particle inside the photonic crystal waveguide and forward scattering on the Bloch band diagram, for the first time in a periodic system which is required to support CESs (Section 3.3). More specifically, responses theory indicates that pulling forces arise from negative gradient in the phase response (Section 3.3.1), where we find that the responses are uniquely determined by the Bloch k and the unit cell function (Section 3.3.2). Combining the Bloch k and unit cell function, we provide an unambiguous identification of Bloch modes in the k space on the periodic Bloch band diagram, where forward scattering agrees with the negative gradient in the phase response and pulling forces (Section 3.3.2). We also studied the spatial symmetry of the responses, which largely simplified the analysis of forces (Section 3.3.3).

In addition, we propose another scheme where we use the absorption on a lossy particle to generate pulling forces in a single-mode one-way waveguide, which is also based on the forward scattering in k space and is supported by the response theory analysis (Section 3.6).

Part of this work has been published at the Conference on Lasers and Electro-Optics[95].

3.1.1 Topologically Protected Light Propagation

Topological photonics have been extensively studied over the past decade [92], [94], inspired by topological insulators that were first discovered in electron systems. A

topological insulator is insulating in the bulk, while conductive on the edge, with robust conductivity that is insensitive to a broad range of impurities or disorders[96]. The robustness of the edge states arise from the robustness of the topological invariants of the bulk, which stay constant under continuous deformations and can only change abruptly when the bulk frequency gaps close and reopen[97], [98]. Since deformation of the edge does not modify the properties of the bulk, the properties of edge states are preserved.

In photonics crystals, by establishing nontrivial topological orders in the bulk band structures, topologically protected robust transport of edge states have been realized. For example, by introducing Quantum Hall (QH) phase that is characterized by non-zero Chern numbers of the bulk bands, one can realize unidirectional transport of chiral edge states (CES) [17], [29]. On the other hand, by introducing Quantum Spin Hall (QSH) phase characterized by non-zero Z2 indices of the bulk bands, one can realize unidirectional transport spin-polarized edge states[34], [99]. However, the QSH system does not protect against backscattering on special defects that flips the spin. Therefore we choose to use the QH system with CES.

The CES is predicted by an analogy between a time-reversal symmetry breaking photonic crystal and an electronic system exhibiting the integer quantum Hall effect [17], [29]. In this analogy, the electromagnetic fields play the part of the electronic current, the variations of permittivity and permeability within the photonic crystal play the part of the periodic potential and the gradients of the gyrotropic components of the permeability tensor play the part of the external DC magnetic field that breaks the time-reversal symmetry. The direction of the external DC magnetic field determines the CES's direction of propagation.

There is a bulk-edge correspondence that determines the existence and propagation direction of the CES[97]. Each bulk band is associated with a topological invariant, called

the Chern number, which characterizes the winding number of the phase of the Bloch wave functions around the first Brillouin Zone. The Chern number of the nth photonic band is

$$C_n = \frac{1}{2\pi i}\int_{BZ} d^2k \left(\frac{\partial \mathcal{A}_y^{nn}}{\partial k_x} - \frac{\partial \mathcal{A}_x^{nn}}{\partial k_y}\right) \tag{3.1}$$

$$\boldsymbol{\mathcal{A}}^{nn'}(k) \equiv \langle \boldsymbol{E}_{nk} | \nabla_k | \boldsymbol{E}_{n'k} \rangle \tag{3.2}$$

where BZ refers to the 1st Brillouin zone, $\langle \cdot \rangle$ denotes an integral over the unit cell in the format of $\langle \boldsymbol{E}_1 | \boldsymbol{E}_2 \rangle = \int d^2r \boldsymbol{\epsilon}(\boldsymbol{r}) \boldsymbol{E}_1^* \cdot \boldsymbol{E}_2$. The Chern numbers are very robust against structural perturbations[100], but can be exchanged in integer numbers between the bulk bands by closing and reopening bulk frequency gaps [97]. The value and sign of Chern number being exchanged between the neighboring bulk bands correspond to the number and direction of CES that would emerge in the bulk bandgap.

CES have been demonstrated in both theoretical work[29] and microwave experiment[17]. In reference[17], [29] , the bulk photonic crystal is composed of magneto-optical material (yttrium iron garnet (YIG)), arranged in 2D square lattice (insets in Fig.3.2). Without external magnetic field, the material has diagonal permittivity and permeability tensor. All the TM bulk bands in Fig.3.2a have zero Chern numbers. When a DC magnetic field is applied in the +z (out-of-plane) direction, the permeability becomes an asymmetric tensor with $\mu_{12} = -\mu_{21} \in \mathbb{I}$, which lifts the degeneracies (Fig.3.2a) between the 2nd, 3rd, and 4th bulk bands, resulting in a band structure as shown in Fig.3.2b. Upon the abrupt change (i.e. lifting of the degeneracies), Chern numbers are exchanged between the bulk bands: The 2nd and 3rd bands exchange a Chern number of -1, the 3rd and 4th bands exchange a Chern number of 1. The resultant Chern numbers are 1, -2, 1 for the 2nd, 3rd, and 4th bulk bands respectively. According to the bulk-edge correspondence[97], along the edge of the photonic crystal, there exist one CES propagating in the clockwise direction in the bandgap of the 2nd and 3rd bulk band, and one CES propagating in the

counter-clockwise direction in the bandgap of the 3rd and 4th bulk band. The dispersion relation of the CES in the bandgap between the 2nd and 3rd bulk band is shown in Fig.3.3a, and the field profile of its unidirectional propagation is shown in Fig.3.3b. The CES navigates around a PEC obstacle inserted perpendicular to its path, demonstrating the robustness of topological protection.

The direction of DC magnetic field determines the direction of propagation for the CES. If the DC magnetic field is applied in –z direction, the exchanged Chern numbers would take opposite sign, the resultant Chern numbers would be -1, 2, -1 for the 2nd, 3rd, and 4th bulk bands respectively. The CES in the bandgap between the 2nd and 3rd bulk band would propagate in counter-clockwise direction.

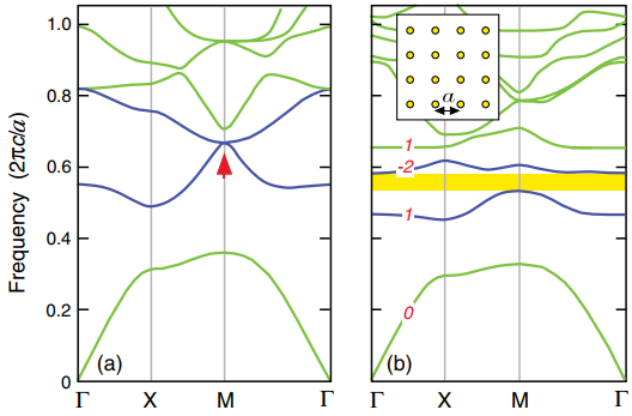

Figure 3.2: (adopted from [29]). Construction of a MO photonic crystal supporting one-way edge modes. The crystal consists of a square lattice of YIG rods (inset in (b), with $\epsilon = 15\epsilon_0$ and $r = 0.11a$) in air. (a) Band diagram with zero dc magnetic field ($\boldsymbol{\mu} = diag([1 \quad 1 \quad 1]\mu_0)$). The relevant quadratic degeneracy point is indicated. (b) Band diagram with a 1600 Gauss +z dc magnetic field ($\boldsymbol{\mu} = \begin{bmatrix} 14 & 12.4i & 0 \\ -12.4i & 14 & 0 \\ 0 & 0 & 1 \end{bmatrix}\mu_0$). The degeneracies are lifted, resulting in the given nonzero Chern numbers (red numbers).

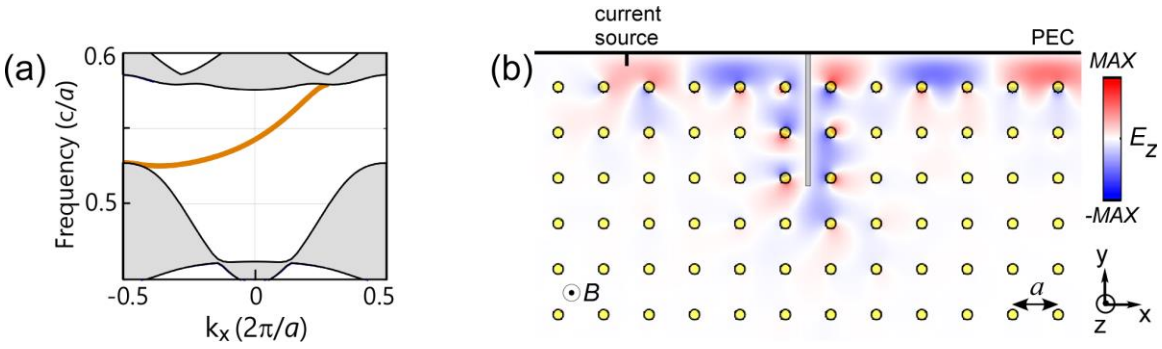

Figure 3.3: Topologically protected chiral edge state (CES) (reproduced from [17]) (a) Dispersion relation of the CES (orange curve) between the 2nd and 3rd bulk band (grey belts). (b) Field distribution illustrating how the CES wraps around a large obstacle made of PEC wall. The photonic crystal consists of a square lattice of rods made of magneto-optical materials, with $\epsilon = 15\epsilon_0$ and $r = 0.11a$ in air. A DC magnetic field is applied in the z direction, leading to the permeability $\boldsymbol{\mu} = \begin{bmatrix} 14 & 12.4i & 0 \\ -12.4i & 14 & 0 \\ 0 & 0 & 1 \end{bmatrix} \mu_0$.

3.2 Pulling Forces From Multi-Mode Scattering

We demonstrate topologically protected pulling forces from forward scattering between two chiral edge states. One CES propagating clock-wise had been realized in the 2nd TM band-gap, along the edge of the photonic crystal composed of magneto-optical (yttrium iron garnet (YIG)) rods in 2D square lattice, under external +z DC magnetic field [17], [101] (Section 3.1.1). We interface two such photonic crystals with opposite DC magnetic field to create a line defect (domain wall) with two chiral edge states traveling along the same direction, according to the bulk-edge correspondence [97], [100]. The size of the defect is $1.5a$, which measures the center-to-center distance between the rows of rods at the interface. Incidentally, the opposite magnetization also sets up a mirror symmetry along the center line of the waveguide[102], and the two chiral edge states can be classified into an even mode and an odd mode (Fig.3.4b). Both modes flow

unidirectionally from the left to the right, with distinct Bloch k throughout the bandgap (Fig.3.4c).

At frequency $f = 0.54c/a$, the odd mode has the smaller Bloch k, and is used for excitation[6]. The incident odd mode (Mode1) is scattered by a round particle ($r = 0.15a$, $\epsilon_r = 13$), partially into the even mode (Mode2). The spatial beating between the odd and the even modes are evident downstream from the particle (Fig.3.4b). Photonic forces on the particle (Fig.3.4d) calculated from integrating the Maxwell stress tensor (MST) in first-principle finite-element simulations exhibit negative axial components over the entire waveguide cross-section. Two thin polytetrafluoroethylene barriers ($\epsilon_r = 2.1$, width=$0.05a$) adjacent to the crystals define the range of motion for the particle, which is slightly narrower than the width of the waveguide because of the finite radius of the particle. Considering the longitudinal translational symmetry of the crystal, the negative photonic forces seen in Fig.3.4d can be mapped to the entire length of the waveguide, suggesting such topologically protected one-way waveguides can sustain photonic pulling forces over long distances.

[6] See the reason of this choice in Section 3.3.

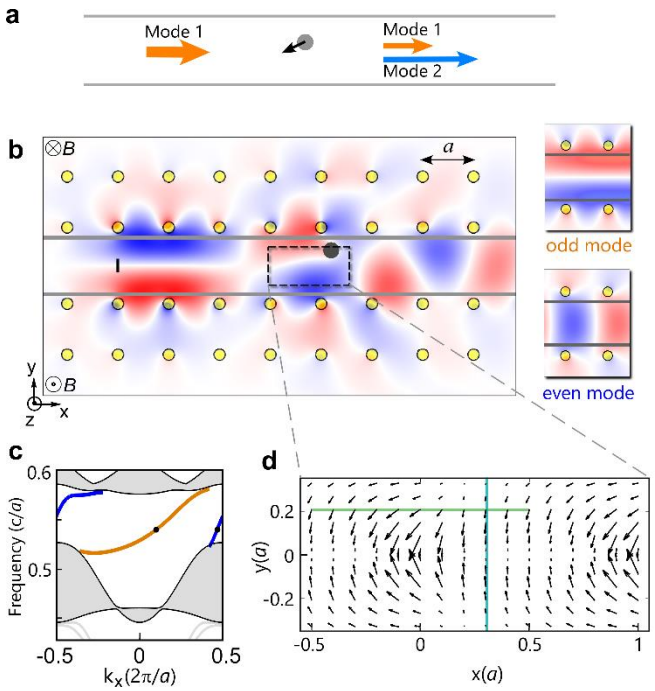

Figure 3.4: Photonic pulling forces in a waveguide with two one-way chiral edge states. (a) Schematic of a particle scattering the incident light (in Mode 1) partly into Mode 2, and experiencing an optical force (black arrow). The power and momentum of Mode 1 (orange) and Mode 2 (blue) are represented by the width and length of the arrows. (b) Calculated field distribution (Ez) of a particle ($r = 0.15a,\ \epsilon_r = 13$) in a one-way waveguide formed between two gyrotropic photonic crystals. The upper crystal and the lower crystal are magnetized along -z and +z directions respectively. The defect size is d=1.5a by measuring the center to center distance between the rods at the interface. A current source (black line) excites the odd mode at frequency $f = 0.54c/a$. (c) Projected band diagram of the propagating even (blue) and odd (orange) chiral edge states. Black dots indicate the operational frequency used in b. (d) Calculated photonic forces experienced by the particle in the waveguide with respect to the center of the particle. The axial components of the forces consistently points towards the left. All possible center locations of the particle is shown as the dashed rectangle in b.

3.3 Response Theory Analysis

3.3.1 Relating the Responses to Pulling Forces

Robust photonic pulling forces in topological one-way waveguide can be conceptually understood from the conservation of linear momentum: for a waveguide with

two and only two distinct (non-degenerate) propagating modes, both unidirectional in the same direction, a particle scattering light from the mode with the smaller linear momentum to the mode with the greater linear momentum should experience a pulling force (Fig.1A). Since backward propagating modes do not exist, back-scattering and the associated pushing forces are completely suppressed. Neglecting the absorption loss of the particle for simplicity, the magnitude of the pulling force is determined by the difference in the linear momentum of the two modes, and the power being scattered between the two. To maintain a pulling force on the particle, the waveguide simply needs to be excited in a way to ensure the particle is illuminate mostly by the mode with the smaller momentum.

However, topologically protected one-way modes exist only in periodic media, which leads to two main difficulties in the analysis above. Firstly, the linear momentum of a Bloch mode in periodic media is not conserved, varying in value at different observation planes[38], [39]. In other words, for a Bloch mode $\boldsymbol{u}(\boldsymbol{r}) \cdot e^{i\boldsymbol{k}\cdot\boldsymbol{r}}$, the Bloch wavevector k alone does not completely determine the linear momentum of the mode, since the unit cell function $\boldsymbol{u}(\boldsymbol{r})$ can vary rapidly in space and contribute significantly to the linear momentum. Secondly, a scattering particle can generate substantial near fields in a periodic medium, which distribute the scattering force from the change in photon momentum to the periodic medium itself. For example, in a photonic crystal waveguide, rods adjacent to a scatterer also experience large photonic forces (Fig.3.5), and the forces on the particle can be smaller or even in the opposite direction.

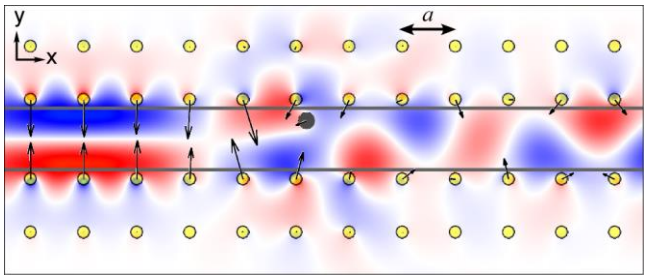

Figure 3.5: Numerically calculated photonic forces on the rods and the particle, at $f = 0.54c/a$. Regions with large positive and negative Ez fields (instantaneous distribution) is shown as the red and blue shaded areas.

These challenges can be resolved elegantly using the response theory of optical forces (RTOF)[42], [43], an energetic treatment for lossless systems under adiabatic changes, to find the conditions for photonic pulling forces in periodic media. Rather than relying on linear momentum, RTOF relates photonic forces to the optical powers and the change in phases of the scattered waves, allowing us to use band diagrams to predict the direction and amplitude of the optical forces on the particle itself. Later we will demonstrate agreement between the forward scattering in k space and the pulling forces (Section 3.3.2). For now, we just show how RTOF predicts the forces, using the responses measured from the full wave studies.

In the waveguide supporting two one-way modes, the force on the particle (scatterer) can be calculated by summing the product between the power and the phase gradient with respect to the displacement of the particle for each mode,

$$F_x(x,y) = \frac{I_1(x,y)}{\omega}\frac{\partial \phi_1(x,y)}{\partial x} + \frac{I_2(x,y)}{\omega}\frac{\partial \phi_2(x,y)}{\partial x} \tag{3.3}$$

Here, ω is the angular frequency of the incident light. I_n and ϕ_n are the power and the phase responses of the n-th outgoing mode respectively. Both I_n and ϕ_n are functions of the particle's location (x, y). Assuming the incoming light is from Mode 1, the first term represents the forces related to the optical power that remains in Mode 1, while the second term represents the contribution from the scattering into Mode 2. Consider the

contribution from the responses in Mode 1. The translational symmetry of the Bloch modes requires that ϕ_1 restore its value after a displacement of the lattice constant a. As a result, $\frac{\partial \phi_1(x,y)}{\partial x}$, as well as the associated forces oscillate between positive and negative. The contribution from the response in Mode 2 determines the overall direction of forces. The averaged force over an axial downstream displacement of lattice constant *a* is determined by the change in ϕ_2

$$\Delta\phi_2(\Delta x = a) = (k_1 - k_2)a + m \cdot 2\pi \tag{3.4}$$

where $(k_1 - k_2)a$ accounts for the change in phase associated with the Bloch k, $m \cdot 2\pi$ is determined by the unit cell functions, and vanishes when the unit cell functions have a constant phase in the axial direction (see Section 3.3.2). In the event of a positive m emerge from a unit cell function with large phase gradient, the sign of $\Delta\phi_2(\Delta x = a)$ can become positive, which leads to a pushing force. However, the optical pulling forces can be restored by using Mode 2 for excitation, reversing the role of Mode 1 and 2.

In order to calculate the optical forces from response theory, we extract the complex-valued amplitudes of the two output modes (a_e and a_o) from an overlap integral between the eigenmode and the output fields over a longitudinal unit cell including the cladding. For example, the amplitude of the odd mode is

$$a_o = v_{go}/2 \cdot \int \epsilon \cdot E_z^{(o)*} \cdot E_z \, dS \tag{3.5}$$

where $E_z^{(o)}$ is the electric fields of the odd eigenmode calculated from an eigen-solver; E_z is electric fields from the full-wave study, taken from a unit cell at a fixed location downstream from the particle (the output reference plane). Normalized by the incident power, the power response of the output odd mode is

$$I_{odd} = \frac{|a_o|^2}{|a_o|^2 + |a_e|^2} \tag{3.6}$$

and the phase response is

$$\phi_{odd} = \angle a_o \tag{3.7}$$

The forces calculated using RTOF is identical to the forces calculated from Maxwell stress tensors, in both the axial and transverse direction (Figs.3.6a, 3.6b). Along an axial path (green line in Fig.3.4d), the axial component of the force F_x (Fig.3.6a) is negative, which is due to the consistent negative slope of the phase response ϕ_2 (Fig.3.6e) accompanied by large power I_2 (Fig.3.6c) of the even mode. ϕ_2 is the sum of three terms: (1) the phase delay from the source to the particle in Mode 1, (2) the phase delay from the particle to the output plane in Mode 2, (3) and the phase delay associated the near fields around the particle. For the displacement of a lattice constant a, term (3) has no contribution due to the periodicity, the contribution from term (1) and (2) corresponds to Eq.3.4. In this case, we find $\Delta\phi_2(\Delta x = a) = (k_1 - k_2)a$ and $m = 0$, which indicate the unit cell function did not modify the direction of scattering. $\Delta\phi_2(\Delta x = a)$ determines the base-line negative force from forward scattering. With $m = 0$, a large difference between k_1 and k_2 is conductive to set up a large negative slope for the phase response, which serves as a large base-line negative force. Now let's consider term (3) for displacements in the range of $(0, a)$. For small particles, near-field contribution to the phase is generally not large enough to change the overall phase response of the even mode (Fig.3.6e).

Now let's revisit the contribution from the responses in Mode 1. In this setup, due to the spatial symmetry (Section 3.3.3), both I_1 and ϕ_1 are symmetric with respect to $x = 0$. Therefore Mode 1 contribute to 0 axial forces on average. However, the periodic fluctuation in ϕ_1 from the near fields does call for a large base-line negative force provided by Mode 2 to maintain an overall pulling force. In this case, the remaining power in the odd mode is kept at minimum, particularly near the regions where $\partial\phi_1/\partial x$ is large and positive, e.g. near $x = -0.24a$ in Fig.3.6c, 3.6e, thereby keeping the direction of the total force unaffected.

As seen in Fig.3.4b, the transverse forces F_y point towards the center of the waveguide. RTOF analysis (Fig.3.6d, 3.6f) suggests that the direction of F_y is largely a result of the phase peak near the plane $y = 0$ for both even and odd modes. Note that the RTOF analysis above for a single unit cell applies to the entire waveguide, thanks to the translational symmetry of the waveguide.

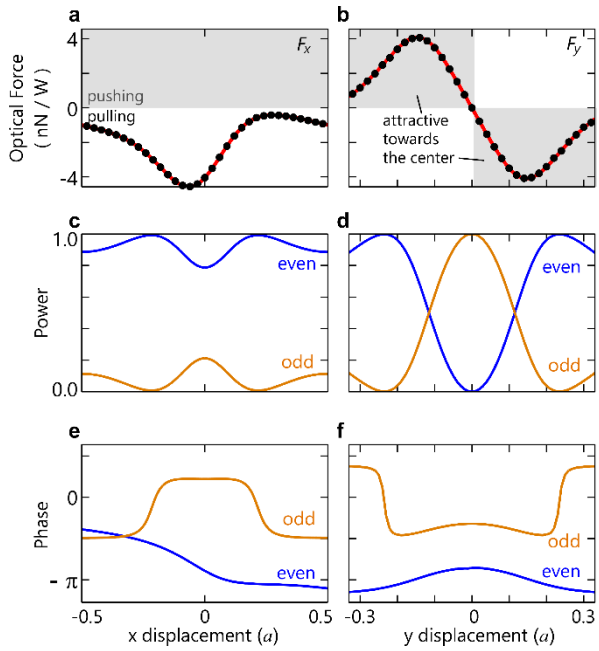

Figure 3.6: Photonic pulling forces analyzed by the response theory. (a) Calculated axial component F_x and (b) transverse component F_y of photonic forces on the particle in the waveguide described in Fig.3.4. Results from the Maxwell stress tensor (red curves) agree very well with the prediction from the response theory (black dots). F_x is evaluated along an axial segment (y=0.2a, shown as a green line in Fig.3.4d), and F_y is evaluated along a transverse segment (x=0.3a, the cyan line in Fig.3.4d). Light enters the waveguide entirely in the odd mode, and is partially scattered into the even mode, with (c,d) normalized power and (e,f) phase responses as functions of the particle displacement.

3.3.2 Responses in Periodic Guided Wave System

For the periodic media being used here, we need to consider the contribution of the unit cell function ($m \cdot 2\pi$ in Eq.3.4) to the phase responses. For a Bloch mode, the Bloch k alone does not completely determine the wavenumber of the mode, since the unit cell function can vary rapidly in space and contribute significantly to the wavenumber. This raises the ambiguity of whether the scattering follows $k_1 \to k_2$, or $k_1 \to k_2 - 2\pi/a$, or $k_1 + \frac{2\pi}{a} \to k_2$, etc. Perturbation theory allows us to identify the authentic wavenumbers of Bloch modes in extended Brillouin Zone. As a result, forward scattering can be determined unambiguously by identifying the Bloch modes in k space, and will be consistent with the negative gradient in the phase response.

We use perturbation theory to explain the underlying mechanism of the responses in the power and phase responses. This way, the contributions from the Bloch k and unit cell functions will be uncovered. In the perturbative regime, the amplitude of scattering from Mode 1 to Mode 2 follows an overlap integral $S_{21} = \left\langle f^{(Mode2)} \middle| \Delta\epsilon \middle| f^{(Mode1)} \right\rangle$ [103], where f is the wave function of the eigen mode, $\Delta\epsilon$ is the perturbation introduced by the scatterer. The physical picture is: Mode 1 (the input) introduces a current density on the scatterer, which in turn excites Mode 2. Because the perturbation is localized on the particle, the integration only needs to be taken over the volume of the scatterer (i.e. the particle). As the particle moves, we can find the power response $I_2(x, y) = |S_{21}|^2$ as well as the phase response $\phi_2(x, y) = \angle S_{21}$.

Here's a demonstration of the perturbation treatment in prediction of the responses using a small particle of radius $\mathrm{r} = 0.05\mathrm{a}$, and permittivity $\epsilon_r = 13$. With TM polarization, the Eigen wave function is reduced to the scalar out-of-plane electric field E_z (Fig.3.7a,b). Let Mode 1 (the input) be the odd mode, Mode 2 be the even mode. The phase response of the even mode becomes $\phi_{even} = \angle \left\langle E_z^{(even)} \middle| \Delta\epsilon \middle| E_z^{(odd)} \right\rangle$. Assuming the

particle (located at (x, y)) is small enough, the overlap integral over the volume of the particle reduces to an integration over a delta function at (x, y). Thus ϕ_{even} simplifies to $\angle E_z^{(odd)}(x, y) - \angle E_z^{(even)}(x, y)$. Tracing along the axial direction (dashed lines in Fig.3.7a,b), ϕ_{even} has a negative slope (Fig.3.7d), being consistent with the negative slope in $\angle E_z^{(odd)}$ and the positive slope in $\angle E_z^{(even)}$. The prediction of ϕ_{even} from perturbation theory agrees well with first principle calculation (Fig.3.7d). The slight discrepancy is due to ignoring the higher order perturbations and the near field. Particularly for the displacement of a, the phase shift $\Delta\phi_{\text{even}}$ is exactly $(k_{\text{odd}} - k_{\text{even}})a$ (with $m = 0$). Similarly, the power responses follow $I_{even}(x) = |S_{21}|^2 \propto \left|E_z^{(odd)}\right|^2 \cdot \left|E_z^{(even)}\right|^2$. In this case, $\left|E_z^{(odd)}\right|$ is relatively uniform along the axial direction (Fig.3.7a), so larger $\left|E_z^{(even)}\right|$ (Fig.3.7a) corresponds to larger I_{even} (Fig.3.7c).

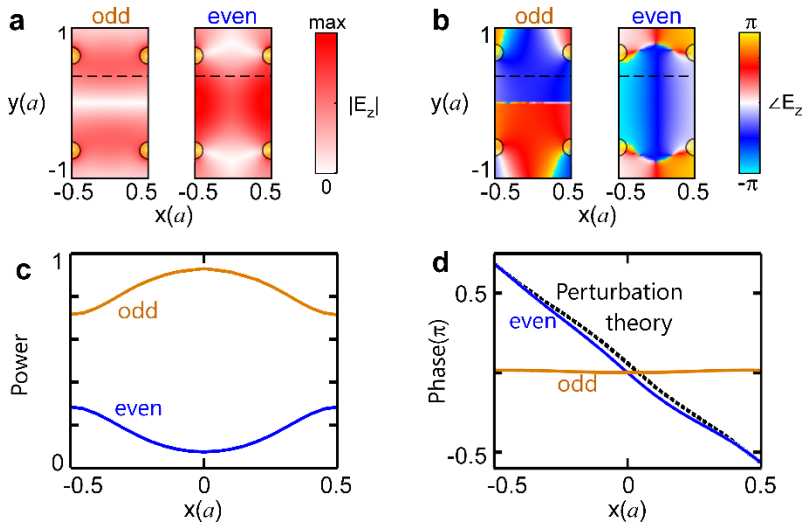

Figure 3.7: Prediction of responses from mode profiles. (a) Amplitude $|E_z|$ of the eigen modes. (b) Phase angle $\angle E_z$ of the eigen modes. (c) Power responses of the outgoing modes versus the particle's axial location from first principle calculation at y=0.35a (dashed lines in a,b). (d) Phase responses of the outgoing modes versus the particle's axial location from first principle calculation (solid line) and from perturbation theory (dashed line) at y=0.35a. The defect size is d=1.3a, frequency f=0.545c/a.

As the field distributions of the eigen modes are employed to determine the power and phase responses, the break down to the contributions from the Bloch k and the unit cell functions becomes clear. According to Bloch theory, the E_z field of the eigen mode is expressed as $E_z(x,y) = e^{i \cdot k_x \cdot x} u(x,y)$, where $u(x,y)$ is the unit cell function, which may carry a multiple of $2\pi/a$ wavenumbers in addition to the Bloch k (upper right panel in Fig.3.8a). Among the many Fourier components embedded in the unit cell function, the dominating component determines its contribution to the authentic wavenumber, where the authentic wavenumber ultimately determines the scattering pathway and is reflected in the overall phase responses. The authentic wavenumber including the contribution from the unit cell function can be written as $k_x + n \cdot \frac{2\pi}{a}$, where $k_x \in [-\frac{\pi}{a}, \frac{\pi}{a}]$ is the Block k. n is the index of the major Fourier component in the unit cell function. After examining the unit cell functions of the entire waveguide band, we find the even mode has $n = 1$ for $k_x < 0$, and $n = 0$ for $k_x > 0$; while the odd mode has $n = 0$ for the entire band. The authentic wavenumbers are identified along the orange and blue curves in Fig.3.8b. This fact is verified as well for the wilder waveguide ($d = 1.5a$) used in Fig.3.4. Therefore the odd mode is located on the left for the entire bandgap, incidence of the odd mode guarantees forward scattering and pulling forces. In particular, at the operational frequency $f = 0.54c/a$ in Fig.3.4, the contributions from both the unit cell functions are 0, which agrees with the phase responses in Fig.3.7e.

It's worth noting that the scattering pathway is completely determined by the locations of authentic wavenumbers, rather than choosing the closest pair in the k space from the periodic band diagram. This point is demonstrated as in Fig.3.8 we have reduced the width of waveguide by $0.2a$ from the one used in Fig.3.4, so that the distance between the authentic wavenumbers of the two modes exceed π/a (half size of a Brillouin zone) for a broader range of frequencies (Fig.3.8b). The incident odd mode is still scattered to

the authentic wavenumber of the even mode on the right (blue line) rather than to the closer brunch on the left (grey line).

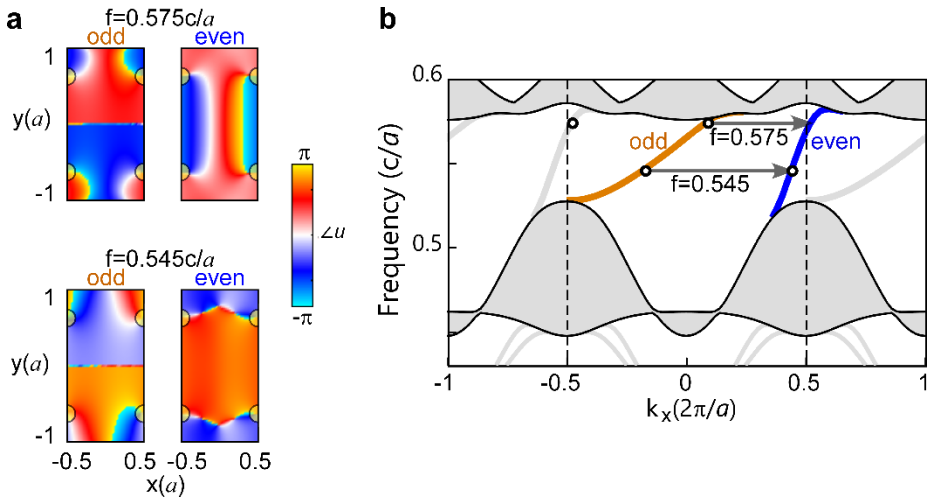

Figure 3.8: Scattering in k-space as determined by unit cell functions. (a) Phase angle of the unit cell functions $\angle u$, for the odd and even modes at two frequencies: $0.545c/a$ and $0.575c/a$. Sharp transition in phase from π to $-\pi$ (from yellow to blue) along an axial path is physically continuous. The integer multiple n of 2π increment in $\angle u$ over one lattice constant in the center waveguide region reveals the multiple of $2\pi/a$ that need to be added to the Bloch k in the 1st BZ to get the authentic wavenumbers. It's found that n=1 for the even mode with $k < 0$ (e.g. at f=$0.575c/a$) and $n = 0$ otherwise. (b) Projected band diagram in extended Brillouin zones. Orange and blue curves represent where the authentic wavenumbers are identified. The four black circles correspond to modes illustrated in (a). Arrows indicate the scattering pathway. The defect size is $d = 1.3a$.

3.3.3 Symmetries in the Responses

For a round particle, the power and phase responses of Mode1 (the input) as a function of the particle's displacement are symmetric with respect to the mirror plane at the center of a unit cell (purple line at $x = 0$ in Fig.3.9a). As a result, Mode 1 contributes a zero axial force, when averaged over one unit cell. Thus the average axial force on the particle is entirely determined by the responses of Mode 2. This symmetry is not incidental,

and can be rigorously proven from a two-step symmetry operation, with the complex amplitude of the transmitted waves unchanged in each step. Here we show that the transmitted power I_1 and phase ϕ_1 of Mode 1 are identical in two systems (Fig.3.9c and 3.9e) where a round particle is situated at same distance from the mirror plane (purple line). In all systems, Mode 1 denotes the odd mode (the input).

The first step relates System 1 (Fig.3.9c) to System 2 (Fig.3.9d) with an operation usually used in the proof of the reciprocity theorem: swapping the source and monitor points. The reversal of DC magnetic field, i.e. transposing the permeability tensor, recovers the conclusion of the Lorentz reciprocity theorem between the two systems: $\frac{J_z^{(1)}}{E_z^{(1)}} = \frac{J_z^{(2)}}{E_z^{(2)}}$. In system 1, the current source $J_z^{(1)}$ is located at point A, and the electric field $E_z^{(1)}$ is detected at Point B. While in System 2 the current source $J_z^{(2)}$ is located at point B, and the electric field $E_z^{(2)}$ is detected at Point A. Point A and B are on nodal planes of the even mode (stars in Fig.3.9a,b), so that only the odd mode is excited and detected. The output amplitudes of the odd mode are identical for system 1 and 2, which translate to $I_1^{(1)} = I_1^{(2)}$ and $\phi_1^{(1)} = \phi_1^{(2)}$.

The second step is a reflection operation with respect to the mirror plane at x=0 that relates System 2 (Fig.3.9d) to System 3(Fig.3.9e). The operation again reverses the sign of the DC magnetic field B_z and transposes the permeability tensor. The operation also reverses the sign of the x-coordinate, and the signs of the field components $E_x,\ H_y,\ H_z$. In particular we have $J_z^{(2)}(x,y) = J_z^{(3)}(-x,y)$ and $E_z^{(2)}(x,y) = E_z^{(3)}(-x,y)$. The symmetry leads to $\frac{J_z^{(2)}}{E_z^{(2)}} = \frac{J_z^{(3)}}{E_z^{(3)}}$, with the current source $J_z^{(2)}$ located at Point B, the electric field $E_z^{(2)}$ detected at Point A in system 2, and vice versa for System 3. Therefore the output amplitudes are identical for system 2 and 3, which translate to $I_1^{(2)} = I_1^{(3)}$ and $\phi_1^{(2)} = \phi_1^{(3)}$.

Combining the two steps, we find that the transmitted power as well as the phase in System 1 and System 3 for Mode 1 are identical.

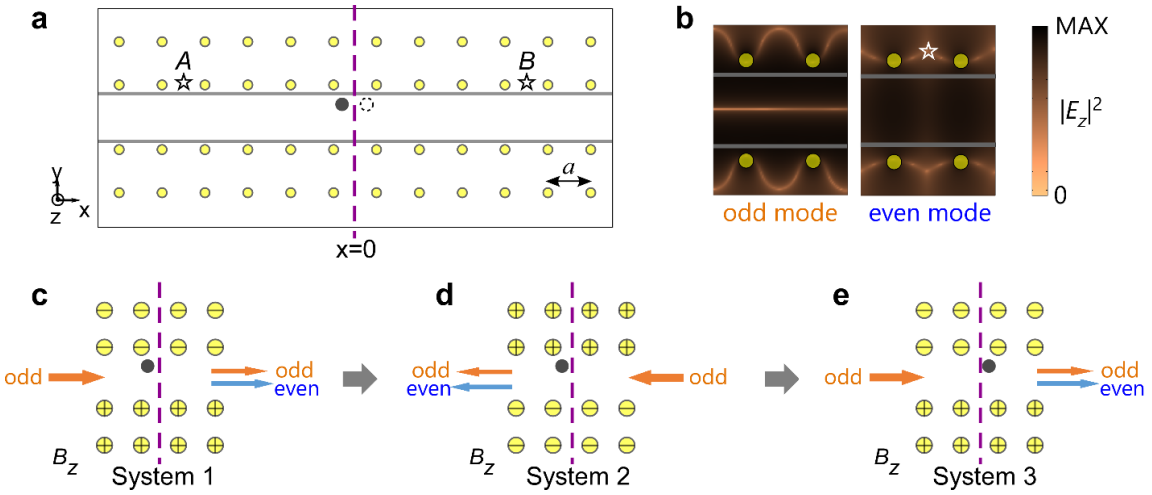

Figure 3.9: Symmetry operations that relate the amplitudes of the scattered light for two mirror-symmetric locations of the particle. (a) Schematics of the structure with the particle at its original location (black disk) and the mirror-reflected location (gray dashed circle) with respect to $x = 0$. (b) Log scale $|E_z|^2$ distribution of the even and odd eigenmodes to identify their nodal planes. A point source (star next to A) and E_z monitor point (star next to B) are placed on the nodal planes of the even mode, to excite and detect only the odd mode. The operations are conducted in two steps, from (c) the original system to (d) its reciprocal pair, and subsequently to (e) the system after a mirror operation. The gray disk represents the particle, and the yellow disks represent the gyromagnetic rods forming the waveguide. "+" and "-" signs indicate the direction of the DC magnetization along z direction.

3.4 Robustness of the Pulling Forces

3.4.1 Pulling a Particle of Arbitrary Size and Permittivity

Since the conditions leading to negative photonic forces in chiral edge states are topologically protected, a wide range of particles (including metallic particles) can be accommodated beyond the small particle limit discussed above, as shown in Fig.3.10. For a subwavelength particle, its scattering cross-section and in turn the magnitude of the

negative photonic forces, depend more on its dielectric constant and size, and less on its shape. Therefore, under the same incident power, larger particles with large dielectric constants generally experience stronger pulling forces than smaller particles. In all combinations of r and ϵ_r covered in Fig.3.10, waveguide regions with negative photonic forces are always contiguous. Small pockets of positive photonic force start to appear near the edge of a waveguide, when the particle is large enough to form Mie resonances with the ferrite rod in the crystal. However, these pockets are not contiguous for the parameter space shown in Fig.3.10. In addition, scatterers with dielectric constants smaller than that of the waveguide, e.g. an air bubble in a high-index liquid, could also produce negative photonic forces, since the forward scattering condition is independent of the properties of the scatterer.

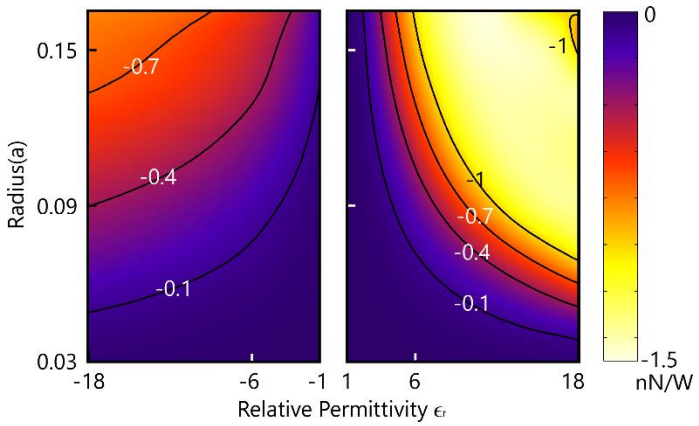

Figure 3.10: Average axial photonic forces F_x for a variety of particle sizes and dielectric compositions. F_x is averaged over all areas inside the waveguide, for a circular dielectric/metallic ($\mu_r = 1$) particle with various combination of relative permittivity ϵ_r and radius r.

3.4.2 Pulling a Cluster of Particles

The topological protection is robust against any defect that preserves the photonic crystal cladding, which translates to an even wider range of targets for photonic pulling

forces. For example, a cluster of three free particles ($\epsilon_r = 13, r = 0.05a$) initially placed within one lattice constant is shown through numerical simulation to be simultaneously pulled in the one-way waveguide (Fig.3.11). As the particles depart from their initial position, they rearrange into a stable formation that allows them to be pulled towards the source in tandem at roughly the same velocity. The stable axial distance between the particles is consistent with the spatial beating frequency between the two modes. Note that the last particle is pushed downstream initially due to near-field interactions, but reverts its course to be pulled upstream shortly after when the particles become separated at the stable formation. Although downstream particles are no longer illuminated by the pure odd mode, the total photonic forces experienced by all three particles as a whole is similar to that of a single particle, that scatters the incident odd mode into the even mode. The total forces move the center of mass of the particle cluster to the left, and eventually the entire cluster will settle at the most upstream location, given enough time.

The trajectories of the three particles are simulated from the equations of motion, using the finite difference method (2^{nd} order central-difference time stepping). At each time step, EM fields and photonic forces are solved using the current locations of the particles.

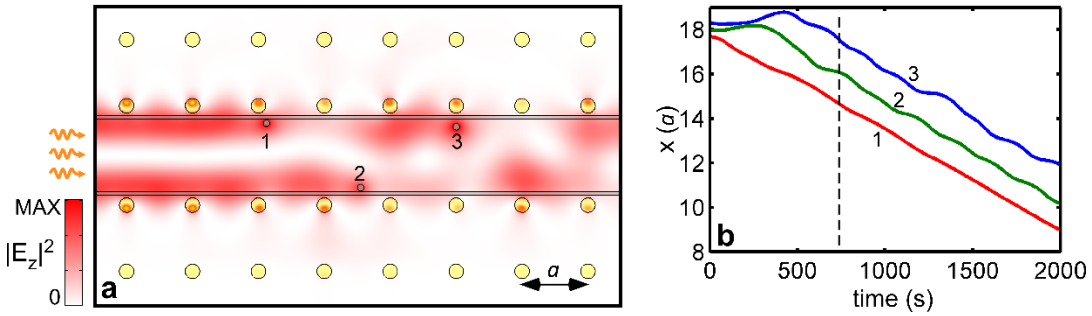

Figure 3.11: Three identical particles (r=0.05a, ϵ_r=13) being pulled together towards the light source in an air-filled waveguide. (a) $|E_z|^2$ distribution after the particles have reached a stable formation, 744 seconds post-release. (b) Time evolution of the x position of the three particles. Dashed line indicates the time (744s) at which (a) is captured. The input field is the odd mode at f=0.54c/a. input power 101.3W/m. lattice constant a=40mm.

For a given terminal velocity of the particle, we determine the commensurate input power levels by recognizing that a steady state is reached when the photonic pulling force is balanced by the viscous drag force of the surrounding medium. An input power P_b generates an average photonic pulling force $F_b = t \cdot P_b \cdot F_x(r, \epsilon)$, where the system thickness[7] t along the z direction is taken as $0.1a$. The power-normalized average axial photonic force $F_x\,(r, \epsilon_r)$ is a function of particle radius r and relative permittivity ϵ_r, as shown in Fig.2.8. For small particles with low Reynold's numbers [104], the drag force is determined by the Stokes law $F_d = -t \cdot 3\pi\mu \cdot v$, where v is the terminal velocity[8]. The corresponding input power is $P_b = 3\mu\pi v / F_x(r, \epsilon_r)$.

For a single particle (r=0.05a, ϵ_r=13), it experiences an average axial photonic force F_x of −0.16nN/W (Fig.3.10). The lattice constant a is taken as 40mm[9]. In an air-

[7] An effective 2D system can be formed between conductive metals[17].

[8] In 3D, the stokes drag forces is $F_{d,3D} = -c_{drag-3D} \cdot v$, where $c_{drag-3D} = \frac{18\mu}{\rho_p d_p^2} m_p = 6\mu\pi r_p$. Here in the 2D system, we are using a coefficient that is normalized by the size of the 3D particle in the 3rd dimension $c_{drag-2D} = c_{drag-3D} \frac{1[m]}{2r_p} = 3\mu\pi$, therefore $F_{d,2D} = -t \cdot c_{drag-2D} \cdot v$.

[9] This setting is inherent from the first experimental demonstration of the chiral edge states[17], operated with microwave. Later in Section 3.4.4 we will perform a scaling analysis versus the dimension and

filled waveguide, with a dynamic viscosity μ of 1.837×10^{-5}Pa·s at 20°C, a single particle can reach the terminal velocity of 0.0046a·s-1, at an input power of $P_b = 202.5$ [W/m]. For the three-particle complex, however, the near field interaction between the three and the final lateral positioning turn out requiring less input power. As they travel, the three particles form a stable complex and are individually settled near the edge of the waveguide, where the axial photonic forces (Fig.3.4d) are roughly twice the value of the overall average forces shown in Fig.3.10. As a result, the actual power used in simulation to reach the terminal velocity of 0.0046a·s-1 is reduced to P_b=101.3W/m.

3.4.3 Pulling a Particle Through a Waveguide Bend

Waveguides have the advantage over free-space optics as being compatible with low-loss and wavelength-scale bends and junctions[105], [106] that enable complex circuit topology, allowing the pulling forces to be routed in nontrivial configurations. For example, a right-angle bend for the dual-mode one-way waveguide completely preserves the incident mode profile, when the radius of a ferrite rod (pointed by an arrow in Fig.3.12a) is reduced from $0.11a$ to $0.071a$. Preserving the incident odd mode is crucial to maintain the pulling forces on the particle before it enters and after it exits the bend (Fig.3.12b). The open structure of the bend introduces no resonance, and thus no trapping forces, as shown in Fig.3.12b, preventing the particle from being stuck. The calculated forces take into account that the electromagnetic fields are significantly modified by the particle displacement. The passage of the particle through the bend, irrespective of its initial transverse location, is numerically confirmed over a broad bandwidth of $0.1(c/a)$.

We simulated the trajectories of a single particle ($r = 0.15a,\ \epsilon = 13\epsilon_0$) being pulled through the waveguide bend, from many different initial positions (Fig.3.13). First,

viscosity, to accommodate the operation at optical frequency and in a microfluidic system.

a series of electromagnetic full-wave simulations were performed to map out the distribution of optical forces as a function of all possible particle locations in the waveguide bend. Then, we solve the equations of motion[10] to obtain the trajectories of particles starting from different initial positions. As seen in Fig.3.13, irrespective of the initial position, all trajectories reach the upper left end of the waveguide, indicating that the particle passes through the bend. The color of the trajectories represents the magnitude of velocity. For a terminal velocity of $0.0014a/s$ and a lattice constant of 40mm, the input power calculated from $P_b = F_d/(F_x(r,\epsilon)\cdot t)$ is 16.2W/m. Here the averaged axial force $F_x(r,\epsilon)$ is found to be −1.4nN/W from Fig.3.10, and Schiller and Naumann viscous force model is used[104] to take into account the larger particle size and the larger Reynold's number. Although the particle's trajectory varies with respect to the input power, we have numerically verified that a ±20% change in the input power does not change the conclusion.

[10] COMSOL Particle Tracing Module is used here. The force field is solved beforehand using COMSOL RF Module and imported into the Particle Tracing Module.

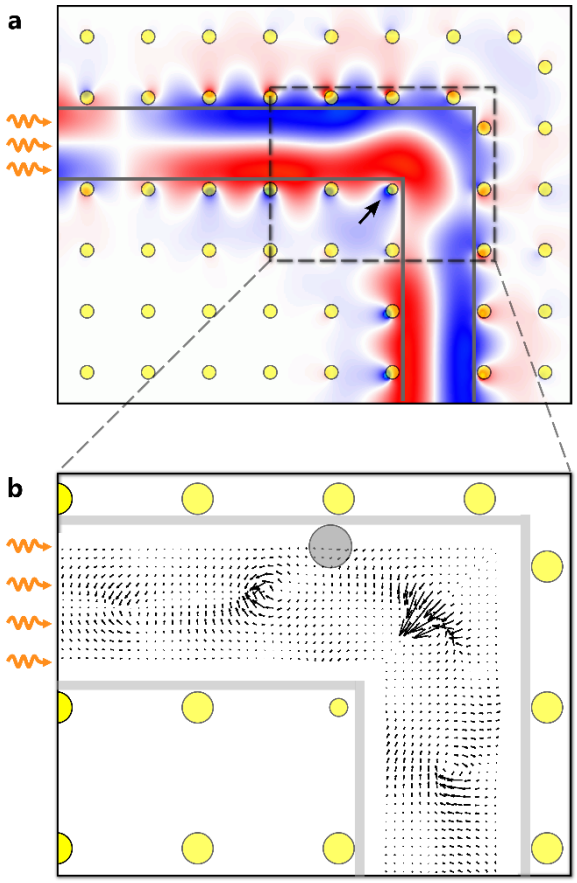

Figure 3.12: Photonic pulling force through a waveguide bend. (a) Calculated Ez field pattern of an odd mode passing through a 90º bend at frequency $f = 0.54c/a$. The size of a ferrite rod (indicated by the black arrow) is reduced to $r = 0.071a$, to keep the odd mode throughout the bend. (b) Calculated photonic forces on a circular particle ($r = 0.15a,\ \epsilon = 13$) over the region indicated by the gray dashed rectangle in a.

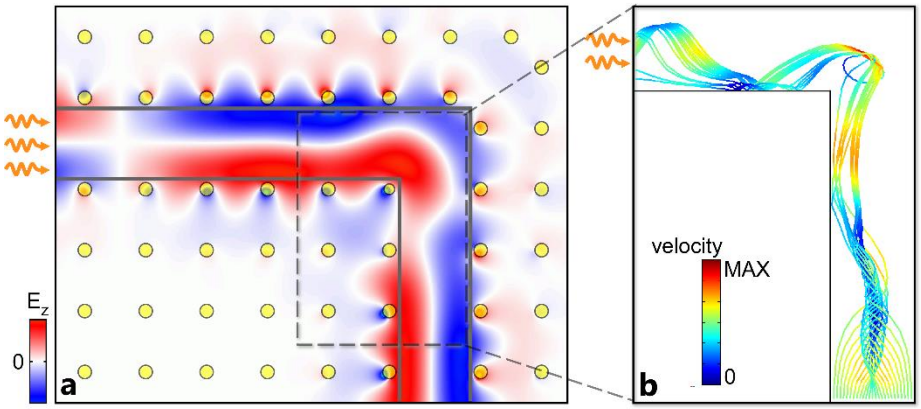

Figure 3.13: Single particle (r=0.15a, ϵ=13) being pulled through a waveguide bend from various initial locations (air filled). (a) Calculated E_z field distribution in the absence of the particle. The input field is the odd mode at frequency f=0.54c/a. (b) Calculated particle trajectories from various initial locations at the lower right corner with the same initial velocity of 0.0014a/s. Colors indicate the magnitude of the velocity |v|.

3.4.4 Scaling Analysis for Optical Manipulation

The dynamics in Section 3.4.2 and Section 3.4.3 are simulated for the operational frequency of 4GHz, corresponding to a lattice constant of 40mm, following the first experimental work that observes the chiral edge state[17]. Because the magnitude of optical forces are proportional to the input power, but not to the wavelength, we need a large power to get the large absolute velocity to match the large system size. Even at the power level of 100W/m, the particle's relative velocities with respect to the lattice constant are still small (Fig.3.11, Fig.3.13). However, at optical frequencies, our system would allow a significantly larger relative velocity with a much smaller absolute power.

We include a brief scaling analysis on the particle's velocity and input power, for the lattice constant and the viscosity typically found in microfluidic systems. To keep the trajectories unchanged, we maintain the same relative velocity (in the unit of a/s), such

that the three particles still travel in that the same stable formation (Fig.3.11) and the single particle still passes through the bend smoothly (Fig.3.13).

A reduction of the lattice constant a by a factor of 10 while keeping the relative velocity the same causes the absolute velocity to be reduced by a factor of 10, which in turn reduces the drag force F_d by a factor of 10. Therefore only 1/10 of the input power per unit thickness P_b (in the unit of W/m) is needed to overcome the drag force at the terminal velocity. Taking into account that the thickness t of the system will also be reduced by a factor of 10, the resultant absolute input power is reduced by a factor of 100.

On the other hand, if the viscosity is reduced from μ to μ', we need to increase the time to $t' = \mu/\mu' \cdot t$, reduce the velocity to dr/dt', and reduce the optical force to $F_b{}' = (\mu'/\mu)^2 \cdot F_b$, in order to keep the equation of motion $m \cdot d^2r/dt^2 = F_b - C\mu \cdot dr/dt$ unchanged. For example, with a reduction in μ by a factor of 10, maintaining the original trajectory requires us to reduce the absolute velocity by a factor of 10, and reduce the drag force, the photonic force and the input power by a factor of 100.

Combining the two scaling relations, we can estimate the terminal velocity and input power for pulling the cluster of three particles (Fig.3.11) at optical frequency in a microfluidic system. Keeping the equation of motion unchanged, replacing the viscous medium of air ($\mu = 1.8 \times 10^{-5}$Pa·s at 20°C) with water ($\mu = 10^{-3}$Pa·s at 20°C) requires increasing the terminal velocity to $0.25\,a/s$ and increasing the input power to 3×10^5W/m. However, this increase is offset by the reduction associated with the smaller lattice constant at optical frequency. For example, for the operational wavelength of 633nm, the lattice constant would be reduced from 40mm to 342nm to keep the relative velocity at $0.25a/s$, accordingly the input power would be reduced to $0.09\mu W$ (assuming the thickness in the z direction is $0.1a$). We note that, strong non-reciprocity for

topological protections at optical frequency may be achieved using novel magneto-optical materials or spatial-temporal index modulations[107].

3.5 DISCUSSION

In a lossless setup, the forward scattering from a mode with smaller wavenumber to a mode with larger wavenumber requires at least two one-way modes. Structures supporting multiple one-way modes can similarly exhibit photonic pulling forces, as long as we choose the mode with the smallest wavenumber as input. Examples include gyromagnetic photonic crystals with large Chern number[108], and multi-mode nonreciprocal surface plasmons situated between a photonic crystal and a metal under a static magnetic field[109].

Large structural disorders upstream from the particle may reduce the photonic pulling forces, because disorders can scatter light into modes with large Bloch k before reaching the particle. Though this problem can be compensated in principle by an excitation field with both eigenmodes components and deliberately-chosen phase lag such that the scattering from the disorder results in a pure low-k mode.

Our demonstrations so far was based on a lossless assumption. However, substantial absorption loss is usually associated with such systems, and must be taken into account. Absorption from the waveguide mainly attenuates the power of the propagating modes, with little impact on the scattering process, particularly when the loss is small. Absorption from the particle generally reduces the magnitude of pulling force, as the power being scattered into the mode of larger k is substituted by absorption on the particle. However, the absorption on the particle can as well contribute to pulling forces as long as the incident mode has a negative wavenumber. In Section 3.6 we will demonstrate pulling forces in a single-mode one-way waveguide, on a lossy particle.

In the response theory analysis, both the intensity and phase of mode 1 (I_1, ϕ_1) exhibit mirror symmetry with respect to $x = 0$, which renders zero contribution from Mode 1 to the average axial forces. Here we note that such symmetry stems from the mirror symmetry of the circular particle (Section 2.5). For particles with less symmetry, $I_1(x)$ and $\phi_1(x)$ can be asymmetric, which may render nonzero, possibly positive contribution to the average axial force. However, as long as the system is resonance free, I_1 and ϕ_1 should still be periodic, therefore the net contribution from Mode 1 will not dominate over Mode 2, particularly when the particle is a small perturbation to the waveguide. Our system also has a mirror symmetry with respect to the plane y=0. However, such y-symmetry is not required for a system to have two one-way modes with very different propagation constants. A waveguide without y-symmetry can still generate pulling forces, for example, waveguide bend does not have y-symmetry.

The structures discussed here can be scaled down proportionally in dimension to operate at optical wavelengths[110]. In practice, visible light is commonly used to manipulate submicron objects, which have a favorable force to mass ratio[111], [112]. To operate at 633nm, the lattice constant needs to be reduced to 342nm, and one needs strong magneto-optical material[109], [113], or time reversal engineering. Through scaling we can apply the general principle of pulling force to sub-micron scale. For a given power, density, fluidic environment, and electromagnetic properties, the terminal velocity is inversely proportional to the square of the lattice constant a. Therefore in the visible light regime (e.g. 633nm wavelength), significant pulling velocity of $0.25a/s$ requires only 0.09μW of optical power (from section 3.4.4).

3.6 PULLING FORCES FROM ABSORPTION

In Section 3.2-3.4 we have demonstrated optical pulling force from forward scattering between 2 one-way modes of different propagation constants. Here we show that with a single one-way mode, pulling forces are still realizable, as long as we can introduce a port with negative slope in the phase responses. With a single one-way mode, topological protection guarantees the transmitted light do not contribute to net axial forces. The port with negative slope in the phase responses must be something else. Lossy particle serves as an extra port, which processes negative slope in the phase responses, when the incident wave has negative propagation constant. In other words, the lossy particle brings the propagation constant of the absorbed photon to zero, which is equivalent to forward scattering in k space when the incoming light has negative k. Therefore, the lossy particle experiences a pulling force.

We still use RTOF for the analysis of forces. RTOF was originally developed for lossless system. To apply RTOF on our lossy system, we treat the loss as effective ports coupled to an energy reservoir, so we effectively have a larger lossless system. Similar approaches are well known in a quantum system with loss, where its non-Hermitian Hamiltonian and the associated non-orthogonal bases can be turned into a Hermitian Hamiltonian and orthogonal bases, when one incorporates the hidden degrees of freedoms associated with the loss. For particles far smaller enough for electrostatic approximation, it is sufficient to describe the absorption on the particle as a single effective port, because the phase and amplitude of the electric field in the volume of the particle is a constant under first order perturbation. Therefore, in a single mode one-way waveguide, when the absorption on the particle is taken into account, two output ports contribute to the overall optical forces (Fig.3.14a),

$$F_x = \frac{I_{tr}}{\omega}\frac{\partial \phi^{(tr)}}{\partial x} + \frac{I_{ab}}{\omega}\frac{\partial \phi^{(eigen)}}{\partial x} \tag{3.8}$$

The first term represent the conventional output port (transmission) of the one-way mode, and the second term describe the force from the power absorbed by the particle. We note that due to the translation symmetry of the crystal and the zero phase gradient of unit cell function, the transmission do not contribute to the axial force on average. The absorption, however, produces a net axial force. First-order perturbation theory yields the power and the phase responses of the absorption port

$$I_{ab}(x_p) = \frac{1}{2}\int_{s_p} Im(\epsilon_p)|E_z|^2 dx'dy' \tag{3.9}$$

$$\phi^{(eigen)}(x_p) = \angle E_z(x_p) = \angle u(x_p) + k_x \cdot x_p \tag{3.10}$$

where x_p is the axial location of the particle, the integration in Eq.3.9 is taken over the volume of the particle in 2D, E_z is the electric field, u is the unit cell function, k_x is the Block k in the axial direction. If the unit cell function has negligible phase gradient and if the phase response in the transmission port $\phi^{(trans)}$ also has negligible gradient (in the weakly-scattering regime), the axial force will be dominated by $\frac{I_{ab}}{\omega} \cdot k_x$ according to Eq.3.8&Eq.3.10. The direction of forces will be dictated by the sign of the Bloch k.

Same as in Section 3.2-3.4, the photonic crystal is formed by a square lattice of ferrite rods polarized by a DC magnetic field (Fig.3.14b) ($\epsilon_{11} = \epsilon_{22} = \epsilon_{33} = 15.0\epsilon_0$, $\mu_{11} = \mu_{22} = \mu_{33} = 14.0\mu_0$, $\mu_{12} = -\mu_{21} = -12.4i \cdot \mu_0$). The chiral edge state we use is located in the 2nd TM bandgap (Fig.3.14c). Being a non-reciprocal single mode in the entire bandgap, the mode is robust to scattering of defects, particles or waveguide bends. A PEC wall is placed close to the domain wall to confine the mode profile. The dispersion relation of the edge mode can be tuned by changing the width of the waveguide, so that negative Bloch k dominates the frequencies in the bandgap. Here we choose a width of 0.7a from the PEC wall to the center of the closest row of rods. We get negative Bloch k from 0.525c/a to 0.555c/a, while positive Bloch k from 0.555c/a to 0.575c/a. The waveguide is designed such that the unit cell function has a vanishing phase gradient along

the axial direction in the waveguide-core region (Fig.3.14d). As we use a weakly-scattering particle ($\epsilon = 2 + 0.5i$), the force is largely determined by the absorption port $\frac{I_{ab}}{\omega} \cdot k_x$. Negative Block k yields optical pulling forces and vice versa.

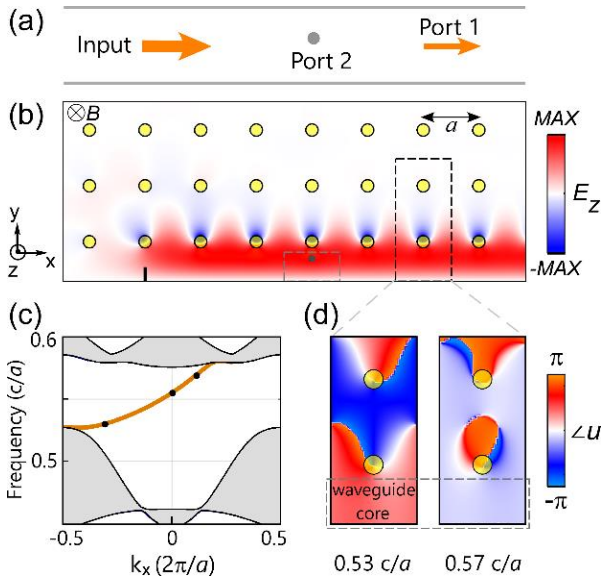

Figure 3.14: (a) Conceptual illustration of optical ports. (b) Electric field of the one-way chiral edge state at f=0.555c/a. A particle (gray dot) is placed inside the waveguide. (c) Dispersion relation of the one-way mode (orange curve). Black dots indicate frequencies of 0.53c/a, 0.555 c/a and 0.57 c/a. (d) Phase distribution of the unit cell function of E_z at f=0.53c/a and f=0.57c/a

At frequencies associated with negative k_x, the negative optical forces are clearly seen in Fig.3.15a. Although only one period is shown, negative forces extends over the entire length of the waveguide, thanks to the translational symmetry of the crystal. The amplitude of axial optical forces vary in space, but remains negative near the core region (y<0.5a) in Fig.3.15a, as the contribution from the 2nd term (absorption) in Eq.3.8 dominates over the 1st term (transmission). When k_x is close to 0, half of the waveguide area exhibit positive force as seen in Fig.3.15b. When k_x becomes positive, optical forces in most area of the waveguides become positive (Fig.3.15c).

The amplitude of the absorption-induced pulling forces is proportional to the power of absorption I_{ab} according to Eq.3.8, which is a linear function of ϵ_i according to Eq.3.9(Fig.3.15d). For Fig.3.15d we have chosen a point on a symmetry plane (x=0.5a) of the unit cell, where the contribution from the 1st term (transmission) vanishes. Strong absorption is favored to get a large pulling force.

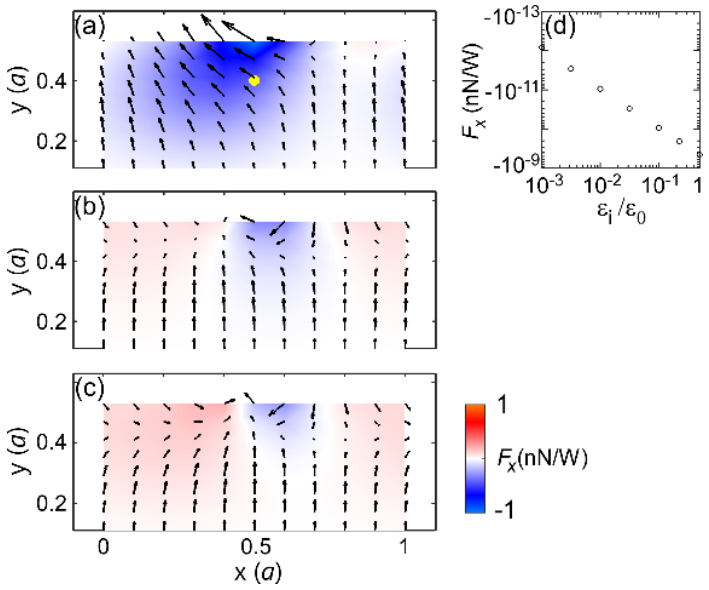

Figure 3.15: (a-c) Vector force fields for a particle (r=0.05a, ϵ=2+0.5i) in the waveguide (corresponding to the gray dashed rectangle in Fig.3.14a), at (a) f=0.53c/a, (b) f=0.555c/a and (c) f=0.57c/a. (d) Force amplitude versus ϵ_i at a fixed point (x=0.5a, y=0.41a) marked by the yellow disk in (a), at f=0.53c/a.

Using RTOF, we numerically separate the contributions to the optical force from the transmission port and the absorption port, by evaluating their power and phase responses respectively. The responses of the transmission port is calculated from the overlap integral between the electric fields at the output and the Eigen electric field over an unit cell. The responses of the absorption port is calculated from the overlap integral between the polarization current and the Eigen electric field over the volume of the particle.

The forces associated with the transmission port average to zero. As shown by the solid light colored lines in Fig.3.16a (0.53c/a) and Fig.3.16b (0.57c/a), the force is anti-symmetric with respect to mirror planes at x=Na and x=(N+1/2)a. Such anti-symmetry in the force follows from the symmetry in the power and phase responses, which is a result of the symmetry in the shape of the photonic crystal and the particle (Section 2.5).

The forces associated with the absorption port is nonzero on average (dashed lines in Fig.3.16ab). The direction of the average of this force is determined by the sign of k_x. The magnitude of the average of this force is determined by the magnitude of k_x. As can be seen in Fig.3.16b, from f=0.530c/a to 0.555c/a, k_x is negative, and the average force is found to be negative (dashed lines from red to purple in Fig.3.16a). The greatest force amplitude coincide with the largest value of $|k_x|$ at f=0.53c/a. When k_x is positive for frequencies from 0.555c/a to 0.570c/a (Fig.3.16b), the average force is positive (dashed lines from purple to blue in Fig.3.16b). The positive average force is not very large as $|k_x|$ is not very large. In part of the unit cell, pushing forces from the transmission port are inevitable, suggesting that it is important to operate with large negative k_x to produce a sufficiently large negative force from the absorption port, resulting in an overall negative force. We find excellent agreement between the response theory and the Maxwell stress tensor method (Fig.3.16).

The competition between the pushing forces from the transmission and the pulling forces from the absorption indicates that optical pulling forces are difficult to realize for strongly-scattering particles. For example, a metallic particle (ϵ = -10+0.5i) scatters strongly, as illustrated by the near-fields expelled from the particle (Fig.3.16c, right inset). The strong scattering causes large oscillation in the forces. Thus pockets of positive force persists even for large negative k_x at 0.53c/a (line with gray dots in Fig.3.16c). Similarly, pockets of negative forces persist even for positive k_x at 0.57c/a (line with gray dots in

Fig.3.16d). On the other hand, for dielectric particles with strong absorption and little scattering (ϵ = 2+0.5i) (Fig.3.16c, middle inset), large negative forces dominates when k_x is large and negative (line with black dots in Fig.3.16c). An intermediate case is a dielectric particle with less absorption and slightly more scattering (ϵ = 10+0.5i) (Fig.3.16c, left inset), the pulling force dominates over oscillation but is not very large, due to the low absorption (line with white dots in Fig.3.16c). Thus, strong absorption is beneficial to maintain an overall negative force, especially for strong scatterers.

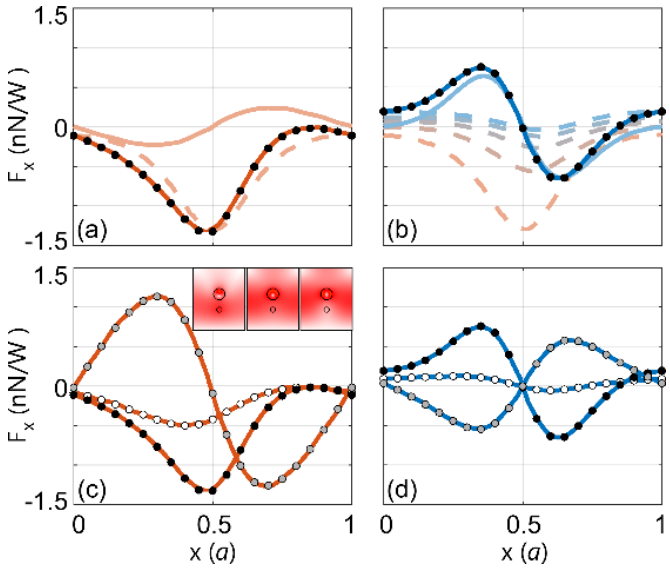

Figure 3.16: Axial optical force as a particle (r=0.05a) is traveling along the line at y=0.4a, calculated using both MST (dots) and RTOF (curves). (a,b) Separate contributions from the transmission port (light colored solid curve) and the absorption port (light colored dashed curve) to the axial forces, at frequencies of (a) f=0.53c/a, (b) f=0.57c/a. The dashed lines in (b) represent the contribution from the absorption port for 5 interpolated frequencies from 0.53(red) to 0.57(blue). The particle has permittivity of 10+0.5i. (c,d) Axial optical force at frequencies of (c) f=0.53c/a and (d) f=0.57c/a for particles of permittivity $10 + 0.5i$ (black dots), $2 + 0.5i$ (white dots) and $-10 + 0.5i$ (gray dots). Inset shows the electrical fields attracted (left), barely perturbed (middle), and repulsed (right) by the particle of permittivity 10+0.5i, 2+0.5i and -10+0.5i respectively. Agreements between RTOF (curves) and MST (dots) method are shown.

The single-mode chiral edge state is topologically protected against scattering loss when it encounters particles, defects, or waveguide bends. Therefore complex routes of pulling force can be configured with such guided wave. However, the width of the waveguide should be carefully chosen, as the dispersion relation is determined by the width of the waveguide. It is beneficial to maintain a range of frequency with large negative k_x.

Although strong absorption produces large negative force given a negative k_x, optical power is reduced after the absorption. Therefore forces in a cascaded setup will decrease for particles downstream. However since the absorption on a single particle is not very significant compared to the input (<5% for the particle with parameter r=0.05a, ϵ =10+0.5i), pulling force on multiple particles is still applicable.

As a summary to this section, we have shown pulling forces can be realized completely using optical absorption on the particle itself, when the particle is immersed in a modal field with negative wavenumber. A mode of negative wavenumber can be created at the edge of a topological non-trivial photonic crystal, i.e. as a chiral edge state. The mode is topologically protected against scattering in single-mode regime, so any momentum transfer due to scattering is suppressed. Large negative wavenumber, strong absorption and weak scattering are beneficial for large overall pulling forces. The pulling forces extend throughout the entire length of the waveguide due to translation symmetry.

3.7 Concluding Remarks

In conclusion, we have theoretically proposed and numerically verified the topologically protected photonic pulling forces using chiral edge states. We found the key to pulling forces is forward scattering in the space of wavenumber k, which can be realized either using multi-mode scattering on a lossless particle or using absorption on a lossy particle (Fig.3.17). Based on response theory of optical forces and perturbation treatment,

we found the forces are determined by the Bloch wave vectors and unit cell functions of the chiral edge states. The pulling forces are robust to the particle's dielectric property, shape, and size. We have also demonstrated the photonic pulling forces over an assembly of particles, and through a waveguide bend.

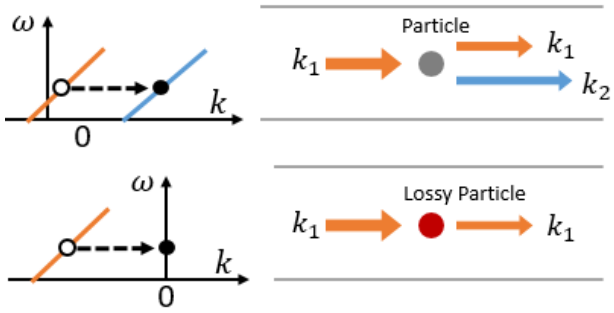

Figure 3.17: Schematics of topologically protected forward scattering in a multi-mode waveguide on a lossless particle (upper panel) and in a single-mode waveguide on a lossy particle (lower panel)

The aforementioned versatilities are unique only to certain topologically protected structures. In particular, we have chosen to use a topologically protected edge state that emulates the Integer Quantum Hall effect[109]. The breaking of time reversal symmetry ensures no mode is available for reflection. Therefore an arbitrary defect (arbitrary particle) is allowed. On the other hand, there exist topologically protect edge states that emulate Quantum Spin Hall Effect (QSHE). The spin degree of freedom can be synthesized by linear combination of TE and TM modes with $\pm 90°$ relative phases [33], [34]. The propagation of opposite spin state is topologically protected in the opposite direction. In the QSHE system, arbitrary particles may flip the spin of the incoming light, which leads to topologically protected reflection. Therefore the QSHE system does not protect against reflection on arbitrary particles and is not suitable for realizing photonic pulling forces.

Chapter 4: Optical Pulling Forces Using Single-mode Backward Waves

4.1 INTRODUCTION

In Chapter 3, we demonstrated photonic pulling forces in one-way waveguides using the topologically protected forward scattering. The pulling forces are long range, being robust to arbitrary particles, defects, and are compatible with complex routes. We note that the realization of one-way modes requires strong non-reciprocity (i.e. breaking the time reversal symmetry). In Chapter 3, we have used magneto-optical materials for this purpose. However, magneto-optical materials have far weaker responses at optical frequencies than their counterpart in microwave regime[114]. To be compatible with integrated photonics [90] and microfluidic channels[91] that typically have feature sizes comparable with optical wavelength, we need to seek for strong non-reciprocity at optical frequencies. One may use spatial-temporal index modulation to introduce strong non-reciprocity [107] and in turn create topologically protected one-way modes[32] in integrated photonics at optical frequency. However, the modulation also introduces extra complexity to the device. It would be a great simplification if one can realize the pulling forces in reciprocal system, i.e., using two-way modes.

People have proposed to use backward waves (i.e. negative index waves)[23]–[25] to obtain optical pulling forces in reciprocal systems. Backward-wave is a special photonic mode which has its propagation constant opposite to its group velocity ($k < 0$ for $v_g > 0$). Using backward waves, reflection becomes a good feature which corresponds to forward scattering in k space (Fig.4.1) and can generate robust pulling forces.

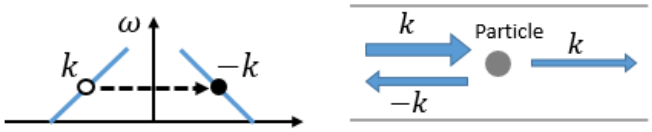

Figure 4.1: Schematics of forward scattering in a backward-wave waveguide on a lossless particle

In fact, we have already encountered a backward-wave in Section3.6, namely, the one-way mode with negative wavenumber k, but it is operated at microwave frequency. At optical frequencies, guided backward-wave pulling forces have been proposed in reciprocal systems such as dielectric waveguide arrays [24] and birefringence waveguides [25]. However, in both references [24], [25] the backward wave coexist with many forward waves at the same frequency. Such multi-mode systems post challenges for experimental realizations: (1) In order to excite the backward wave alone, the light source/current source need to have a spatial configuration that is orthogonal to all the forward waves. (2) Disorders due to imperfect fabrication can scatter the excited backward wave into forward waves along the propagation. Whereas single mode backward wave offers great benefits: (1) The excited wave would be a pure backward wave irrespective of the configuration of the source. (2) The backward waves could be reflected by disorders due to reciprocity, but those propagating forward are not contaminated.

Photonic crystals provide rich degrees of freedom to tune the dispersion relations to achieve backward waves [23], [41], [115], meanwhile having low absorption loss. However, the backward waves reported in references [23], [41], [115] were found in bulk photonic crystals, which lacks lateral confinements and cannot be guided through complex routes. Moreover, backward-wave modes in bulk photonic crystals coexist with other modes on one or more equal-frequency contours in the band structure[110], which are inherently not single-mode.

We seek to find single-mode backwards waves in reciprocal system, operating at optical frequencies, and also having the flexibility to be guided through complex routes. Photonic crystal defect waveguide is the ideal choice because defect waveguide mode can be engineered into a single mode in the bandgap of the bulk modes. In the meantime, we can exploit the periodic spatial modulation of a photonic crystal to construct backward waves.

In this chapter, we propose the first realization of single-mode backward waves using the photonic crystal defect waveguide (Section 4.2), to generate *optical* pulling forces in a reciprocal system. Reflection of backward waves corresponds to forward scattering in k-space and pulling forces (Section 4.3), which is confirmed by both MST and response theory (Section 4.3.1). Particles inside the waveguide can be traced towards the light source through a stable trajectory, using a small optical power (Section 4.3.2). Similar to Chapter 3, the periodic system introduces Bloch modes that need to be carefully identified in the k space with the information of both Bloch k and unit cell function. We give an example of aliased backward wave with similar dispersion relation but is essentially a forward wave that only generates pushing forces (Section 4.4).

This work has been published at the Conference on Lasers and Electro-Optics[116].

4.2 Single-mode Backward Waves in Photonic Crystal Defect Waveguide

We use a 2D photonic crystal defect waveguide with modified rods (Fig. 4.2a,d) to create the single-mode backward-wave (Fig.4.2b). The backward-wave has its Bloch k opposite to the group velocity. For this structure, the unit cell function did not contribute to modify the wavenumber k (detailed in Section 4.3.1).

Two rows of rods in the photonic crystal defect waveguide (Fig. 4.2a) are modified to ensure single-mode operation. A backward-wave defect mode is found in the 2nd TM

bandgap of the bulk photonic crystal, using a defect of width $d = 1.5a$ (Fig.4.2a). However, the simple defect waveguide structure also introduces a forward wave which covers the entire frequency range of the backward wave. In other words, the dispersion relation of the defect mode fails to maintain a negative slope throughout the positive half of the Brillouin zone: positive slope appears for the region of $k_x > 0.35(2\pi/a)$, and eventually the dispersion relation of the defect mode rises into the upper bulk band of the cladding (Fig.4.2b). The coexistence of the forward-wave mode raises possibility for pushing forces to be unintentionally introduced as described in the introduction. To avoid this issue, a modified structure is designed to pull down the frequencies of the defect mode in the region of $k_x > 0.35(2\pi/a)$ to a much lower value such that the defect mode is forced into the lower bulk band near the Brillouin zone boundary (Fig.4.2b). In the meantime, we make sure that no additional defect modes are pulled from the upper bulk band. Therefore we can obtain a single-mode backward wave.

It is well known in perturbation theory that adding high-index dielectrics to regions of high electric fields of an eigen mode lowers its frequency[14], while adding dielectrics to nodal planes of electric fields does not change the mode frequency. Following this principle, we noticed the significant difference in the field patterns of the defect modes and the modes in the upper bulk band of the cladding in regions near the second row of rods (Fig.4.2c). By adding a narrow elliptical tail (0.05x0.2a) of dielectric to these rods (Fig.4.2d), we achieved the aforementioned modification to the dispersion relation.

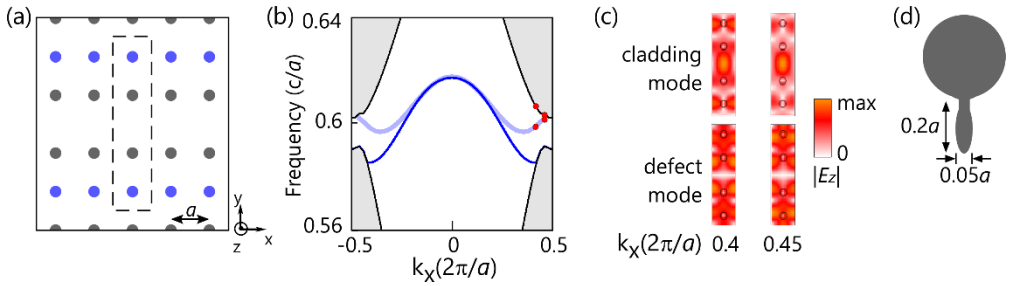

Figure 4.2: Tailoring the dispersion relation of a photonic crystal line defect for single-mode operation of backward waves. (a) Line defect created by enlarging the distance between two rows of dielectric rods in a 2D photonic crystal. The width of the defect is $d = 1.5a$ (b) Calculated dispersion relation of the line defect mode corresponding to the structure in panel a (light blue) and that of a modified line defect in Fig.4.3a (dark blue). The unmodified line defect supports a backward-wave mode for $|k_x| < 0.35(2\pi/a)$ but it is not a single-mode. Gray areas represent the projected band diagrams of the bulk modes. (c) Calculated electric field distributions of the defect mode and the lowest-frequency cladding mode above the bandgap at two k-points: k_x of $0.4(2\pi/a)$ and $0.45(2\pi/a)$ (red dots in panel b), in the region outlined by the dashed rectangle in panel a. (d) Detailed structure of the rods in the second row (blue circles in panel a) of the modified line defect. A "tail" structure is added to generate the dispersion relation shown by the thin blue curve in panel b.

4.3 Pulling Forces From Reflection of Backward Waves

A silicon particle inside the waveguide (Fig.4.3a) introduces reflection, i.e. the incoming backward-wave at negative k point is forward scattered into the positive k point (Fig.4.3b). Consequently the particle experiences pulling forces (quiver plot in Fig.4.3h). The pulling forces follow the discrete translational symmetry of the periodic system and exist over its entire length. The pulling force is valid over 1% bandwidth around the operating frequency.

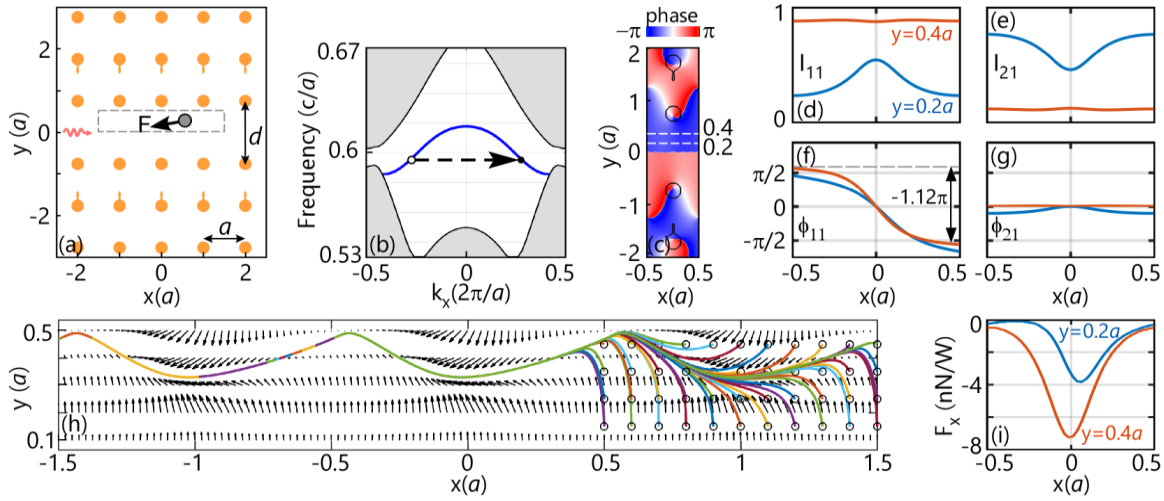

Figure 4.3: Backward-wave generating long-range pulling forces. (a) Schematic of the waveguide: line defect with a width $d = 1.5a$ along the Γ-X direction in a 2D square lattice photonic crystal of silicon rods ($r = 0.15a$, $\epsilon_r = 12.25$). Curly arrow indicates the incident light. The 2nd row of rods from the center are modified with a small 'appendix' to ensure single mode operation. (b) Dispersion relation (TM-polarization) of the backward-wave mode (blue). Gray regions are projected band diagrams of the bulk modes. Arrow indicates the scattering pathway. The waveguide is excited with a backward-wave at $k_x = -0.28 \cdot 2\pi/a$ and $\omega = 0.595 \cdot 2\pi c/a$. (c) Phase distribution of the unit cell function $\angle u(x, y)$. (d-g) Intensity and phase response of the reflection (I_{11}, ϕ_{11}) and transmission (I_{21}, ϕ_{21}) with a silicon particle ($r = 0.05a$, $\epsilon_r = 12.25$) moving along the dashed lines in (c). (h) Vector force field for the particle in the dashed gray box in (a) and particle trajectory released from various initial locations (black circles). Only one particle is present at any given time. (i) Axial optical forces on the particle moving along the dashed lines in (c)

4.3.1 Response Theory Analysis

To obtain the power and phase responses of the reflected and transmitted Bloch waves from first-principle calculations, we sampled the calculated fields (E_z fields for the 2D TM mode considered here) at a fixed interval of a along the waveguide axial direction. The fields are taken sufficiently away from the particle, where the near fields of the particle are negligible. The fields are also taken at a finite offset from the waveguide center ($y = 0$), which is a nodal plane for the backward-wave mode. The purpose of the periodic

sampling is to remove the influence of the unit cell function $u(x,y)$, which is periodic in x. In the case of the single-mode backward-wave waveguide, sampled fields in the region upstream from the particle were fitted to the expression $A_0 e^{ik_x \cdot x} + A_R e^{-ik_x \cdot x}$, and those from the region downstream to the expression $A_T e^{ik_x \cdot x}$, which allowed us to extract the complex-valued amplitudes of the incoming wave A_0, the reflected wave A_R, and the transmitted wave A_T. The power responses of the reflected and transmitted waves are normalized to that of the incident wave, as $I_{11} \equiv |A_R/A_0|^2$, $I_{21} \equiv |A_T/A_0|^2$. The phase responses are calculated at fixed reference planes.

The negative axial forces are verified by the power and phase responses according to RTOF (Fig.4.3d,e,f,g,i). The axial optical force is expressed in terms of phase responses of the outgoing waves versus the particle's axial displacement, $F_{\mathrm{x}} = I_{11}(x)/\omega \cdot \partial\phi_{11}(x)/\partial \mathrm{x} + I_{21}(x)/\omega \cdot \partial\phi_{21}(x)/\partial \mathrm{x}$, where ω is the frequency, I is the power, ϕ is the phase. Subscript 11 stands for the reflected wave and 21 stands for the transmitted wave. The transmitted wave introduces 0 contribution to the average axial force due to the symmetry in both I_{21} and ϕ_{21} (Fig.4.3e,g). The reflected wave plays the key role to determine the direction of axial force. The negative slope in ϕ_{11} versus displacement x confirmed that the axial force is negative (Fig.4.3f).

As mentioned in Chapter 3.3, for periodic waveguides, the phase response of a Bloch mode is determined by not only the Bloch k but also the unit cell function. Treating the particle as a perturbation to the waveguide, we find $\phi_{11}(x,y) = 2k_x \cdot x + 2\angle u(x,y)$, where (x,y) is the location of the particle, k_x is the Bloch k in the first Brillouin Zone, $u = E_z/e^{ik_x x}$ is the unit cell function and in this case of TM polarization it is based on the out-of-plane electric field E_z. Bloch theorem indicates the phase of the unit cell function satisfies $\angle u(x+a,y) - \angle u(x,y) = 2\pi N$, where N is an integer.

For the backward-wave in Fig.4.3, we find $N = 0$ in the line defect (Fig.4.3c), thus $\angle u$ is not modifying the overall negative slope ($2k_x = -1.12\pi/a$) in ϕ_{11} but only brings some spatial variations to the slope (Fig.4.3f). As the particle moves by one lattice constant, the change in ϕ_{11} amounts to $2k_x a = -1.12\pi$. Therefore the pulling force from backward wave is concrete.

4.3.2 Lateral Stability and Optical Power for the Pulling Forces

To allow a particle to be pulled continuously throughout the waveguide, especially in the photonic crystal structure with open cladding, it is necessary for the optical force field to provide lateral stability. The force field (Fig.4.3h) in the pulling-force-generating waveguide exhibits excellent lateral stability, as confirmed by particle tracing calculations (Fig.4.3h) for a particle being released from varies initial positions. A finite-difference time-domain solver is used to solve the equation of motion for the particle under both the optical forces and the viscous forces in a 3D system extrapolated from the 2D simulation. Such extrapolation is experimentally realizable by truncating a 2D photonic crystal in the 3rd dimension with conductive surfaces[29], [117]. In the extrapolated 3D system with an out-of-plane thickness t (typically $0.1a$), for a given input optical power I (in the unit of W/m), the optical force is $t \cdot I \cdot \boldsymbol{F}$, where $\boldsymbol{F}$ is the power-normalized optical force from the 2D finite element calculations in the unit of N/W. The viscous force for a particle with velocity $\boldsymbol{v}$ under the Stokes' law[104] is first normalized using the diameter of the particle in the out-of-plane direction to yield $-3\pi\mu\boldsymbol{v}$, then multiplied by the thickness t. Here the viscosity μ is taken as 1.837×10^{-5}Pa·s for air at $20°C$. Remarkably, all trajectories converge to a common path within one lattice constant from the initial release, as long as the initial velocity is not too large ($< 1a/s$). The stable trajectory has a lateral (y) offset from the waveguide center and is confined between y=$0.17a$ and y=$0.42a$, with a mirror

image in the lower half of the waveguide, as the mode satisfies an odd symmetry laterally (Fig.4.3c). The quick convergence suggests that a steady state is rapidly reached, in which the optical force is balanced by the viscous force: $t \cdot I \cdot \boldsymbol{F} = 3\pi\mu t\boldsymbol{v}$, allowing us to translate the optical force field into a steady-state velocity field of $(I/3\pi\mu)\boldsymbol{F}$ for the particle, independent of the initial location of release. Notice that the thickness t is cancelled when balancing the extrapolated optical forces and viscous forces, and it does not change the required power (in unit of W/m) for a steady-state velocity. Operating at the wavelength of 1550nm, the required frequency 0.595(c/a) in the band diagram determines the lattice constant a to be 922nm. With a steady-state velocity around $-0.4a \cdot s^{-1}\hat{\boldsymbol{x}}$, the required input optical power is 78.6mW/m. Assuming a thickness of $t = 0.1a$ for the extrapolated 3D system, the power needed is 0.00725μW.

4.4 Distinguishing Aliased Backward Waves in Periodic Structure

There are many occasions when a Bloch mode has a negative Bloch k, while its unit cell function carries nonzero phase shifts over one lattice constant. We have already encountered such an occasion in the one-way waveguide (Fig.3.8), for the evan mode at the frequency of $0.575c/a$. In Fig.3.8, the unit cell function of the even mode equivalently carries an additional wavenumber of $2\pi/a$. The total propagation constant becomes positive at $k_x + 2\pi/a$, although the Bloch k k_x is negative. We call this an aliased backward wave.

Here we show an example of aliased backward wave in two-way waveguide. Not surprisingly, it produces pushing force upon reflection. The mode is found in a photonic crystal defect waveguide between 45 degree tilted squared lattice of Silicon (Fig.4.4a). The dispersion relation follows the blue curve in Fig.4.4b. For clarity of explanation, we have plotted two Brillouin Zones. The unit cell function of this mode (Fig.4.4c) has a 2π phase

shift over one lattice constant. Therefore, moving the particle by a lattice constant traces a full 2π shift in the phase of the unit cell function, thus ϕ_{11} has an overall change of $2k_x \cdot x + 4\pi = 2.6\pi$, with positive slopes in between (Fig.4.4d). Consequently the average axial force is positive (Fig.4.4e).

As the unit cell function modifies the propagation constant from k_x to $k_x + 2\pi/a$, the scattering pathway follows the black arrow in Fig.4.4b instead of the gray arrow. This scattering pathway is no difference from the reflection of a plane wave, which generates pushing forces.

In other structures, there could be a combination of positive Bloch K and negative contribution from the unit cell function, resulting in a backward wave as well[23].

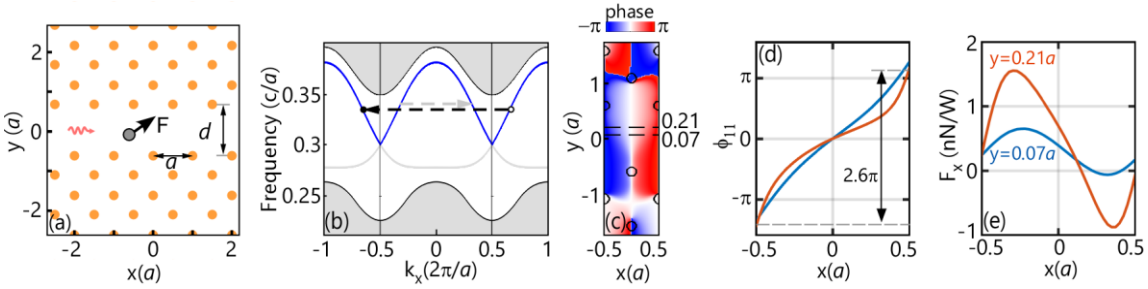

Figure 4.4: Aliased backward-wave generating pushing forces. (a) Schematic of the waveguide: line defect with a width $d = (\sqrt{2}+1)a/2$ along the Γ-M direction in a 2D square lattice photonic crystal of silicon rods ($r = 0.0849a$, $\epsilon_r = 12.25$). Curly arrow indicates the incident light. (b) Dispersion relation (TM-polarization) of the aliased backward wave (blue) for the first 2 Brillouin Zones. Gray arrow: the wrong scattering pathway, Black arrow: the correct scattering pathway. The waveguide is excited with an aliased backward-wave at $k_x = -0.35 \cdot 2\pi/a$ and $\omega = 0.332 \cdot 2\pi c/a$. (c) Phase distribution of the unit cell function $u(x, y)$. (d) Phase response of the reflection with a silicon particle ($r = 0.05a$, $\epsilon_r = 12.25$) moving along the dashed lines in (c). (i) Axial optical forces on the particle moving along the dashed lines in (c)

4.5 CONCLUDING REMARKS

We demonstrated long-range optical pulling forces using backward-waves in photonic crystal defect waveguides. The force field supports a stable trajectory irrespective of the initial position. Photonic crystal structure has the advantage to allow the tuning of dispersion relation to achieve single mode operation, which can largely reduce scattering loss and facilitate simple experimental implementations. It also paves the way towards the integration of optical pulling forces with microfluidic systems, and potential incorporation of complex routing topology such as beam splitters and T-junctions[118]. Moreover, this reciprocal system is readily realizable in pure silicon structure, at optical frequencies.

As pointed in Section 4.4, for periodic systems, negative Bloch k do not guarantee a backward-wave. The unit cell function is crucial in distinguishing the aliased backward-waves. This point is corroborated by an example of aliased backward wave, which only generates optical pushing forces.

It is also useful to point out the limitation of perturbation theory in predicting consistent pulling forces in photonic crystals. So far, we have derived the optical forces from phase response which relies on the validity of perturbation theory. However, when the particles are large enough to cause strong near-field interaction with the photonic crystal[119], the perturbation theory is no longer accurate. Instead, deep potential wells associated with resonances (sharp phase shifts) may emerge. In this paper, we use silicon particles with radii smaller than $0.06a$ to stay away from resonances. Alternatively, lower index allows larger particles to be tolerated.

Chapter 5: Linear Momentum Flux and Optical Forces in Periodic Structure

5.1 INTRODUCTION

For predicting the photonic pulling forces on a particle placed inside periodic structures (Chapter 3, Chapter 4), we have been using response theory[42], a virtual work approach, because we do not know the proper form of linear momentum in periodic system, and its relation with photonic forces. In this chapter we explore the way to apply momentum conservation in periodic structures, which breaks down to the following questions: For the Bloch modes in periodic media, can we define an intrinsic quantity relevant to linear momentum and optical forces, and visualize it as a function of frequency, just like the photonic band structure which is well known? How does the defined quantity relate to the propagation constant in magnitude and sign? Can we use band structure to tailor optical forces, e.g. to enhance optical forces at photonic band edge with the near-zero group velocity? How to account for the forces distributed over the periodic medium, defects, interfaces and reflectors, to arrive at agreement with momentum conservation?

Propagating waves carry linear momentum. The conservation of linear momentum governs the force/tensor incurred as light encounters an interface of different medium, either dielectric or metamaterial, either homogeneous or periodic, either impedance matched or mismatched. This topic has been studied in both theoretical [40], [80] and experimental [120] works. Mathematically, the law of momentum conservation is expressed as[44]

$$-\int_V \boldsymbol{f} d\Omega + \int_S \overleftrightarrow{T} \cdot dS = \frac{d}{dt}\int_V \boldsymbol{g} d\Omega \tag{5.1}$$

where $\boldsymbol{f}$ is the force density, being integrated over a defined volume V, $\overleftrightarrow{T}$ is the electromagnetic stress tensor, being integrated over a surface S enclosing the volume (the surface normal points outwards), $\boldsymbol{g}$ is the density of linear momentum in the volume.

There had been a long debate about the correct form for the linear momentum and the corresponding electromagnetic stress tensor in photonic media, which is known as the Abraham-Minkowski controversy, and is only recently resolved [121], [122]. However, if we focus on the steady state solution of the electromagnetic field, which is sufficient to treat the optical forces of our interest, Eq.5.1 reduces to

$$\int_S \overleftrightarrow{T} \cdot dS = \int_V \boldsymbol{f} d\Omega \tag{5.2}$$

Therefore, rather than the linear momentum density $\boldsymbol{g}$, the flux of linear momentum associated with the propagation of the Bloch mode ($\overleftrightarrow{T} \cdot dS$) [44] is more relevant to the optical forces in steady state. Momentum flux is a concept closely related to fluid mechanics[104] and draws similarities with electromagnetics. It represents how much momentum is carried by the fluid or optical field flowing over a unit surface per unit of time, in the form of the product of a stress tensor and a surface norm. However, quantifying momentum flux and understanding how it behaves upon scattering and reflection in periodic structures are quite different from that in homogeneous media. Because the periodic structure have inhomogeneous permittivity and permeability, the electromagnetic stress tensor, which is expressed in terms of the permittivity and permeability, is also non-uniform. Whereas a conserved quantity is preferred to describe the property of the medium and to facilitate the recognition of momentum conservation. Only in the long wavelength limit, one can use effective medium theory to model the effective permittivity and permeability and arrive at a uniform momentum flux for the periodic structure[39], [40]. However, momentum flux is not yet explored over a broader spectrum in periodic structures.

Our work analyze the linear momentum flux of the Bloch modes in the periodic structure, including its underlying composition, spectra, and implications on optical forces. We start with defining the momentum flux in terms of a conserved quantity under

translational symmetry (Section 5.2). Then, we recognize that the momentum flux can be decomposed into contributions from the underlying plane wave components: the propagating and evanescent plane waves (Section 5.3), whose contributions are quite different. The propagating plane waves always contribute to positive momentum flux in the direction of power flow, while the evanescent plane waves can lead to a momentum flux negative to the power flow (Section 5.4). By visualizing the momentum flux into spectra, we find it exhibits great difference from the spectra of Bloch k (i.e. the dispersion relation), in both the magnitude and sign, and it can also diverge near the band edges (Section 5.4). At the last, we show how to apply the conservation of momentum flux and how the optical forces are distributed in the periodic structure. We also revisit the momentum conservation in the setup (see Chapter 3) used to obtain photonic pulling forces (Section 5.5).

5.2 Linear Momentum Flux in Periodic Structure

We start by deriving the liner momentum flux carried by Bloch modes in periodic media with contiguous areas of free space. For example, in a 2D square lattice of dielectric rods, the existence of cross sections of the photonic crystal that are entirely in the free space (e.g. the dash line in Fig.5.1a) allows us to define the momentum flux unambiguously from the Maxwell Stress Tensor (MST), since in free space the linear momentum is entirely carried by the electromagnetic field and the definition of momentum density is not controversy[44]. Thanks to the translational symmetry, the evaluated momentum flux is invariant for each cross sections placed at integer multiples of the lattice constant apart. According to Eq.5.2, momentum flux carried by a mode propagating in the +x direction through an x-normal cross section equals to the optical forces applied towards the right hand side of the cross section per unit area. Without influencing the field profile or the

momentum flux on the left hand side, we can replace the right hand side of the cross section with a perfect absorber [11] (Fig.5.1b). Therefore, the definition of momentum flux corresponds to the forces applied on a perfect absorber per unit area. Integrating over the x-normal cross section, the x-component of the forces and the momentum flux is

$$F_x = \int_S \overleftrightarrow{T} \cdot dS_x = \int -T_{xx}\, dydz \tag{5.3}$$

where T_{xx} is the (x,x) element of the Maxwell stress tensor. Normalizing by the power I_x, we arrive at a power-normalized linear momentum flux p_x, which is an intrinsic property of a Bloch mode.

$$p_x = F_x / I_x \tag{5.4}$$

Notice that the Maxwell stress tensor also indicates the existence of shear forces $\int -T_{yx} dydz$, $\int -T_{zx} dydz$ that are normal to the x direction. The shear terms are out of the scope of this work.

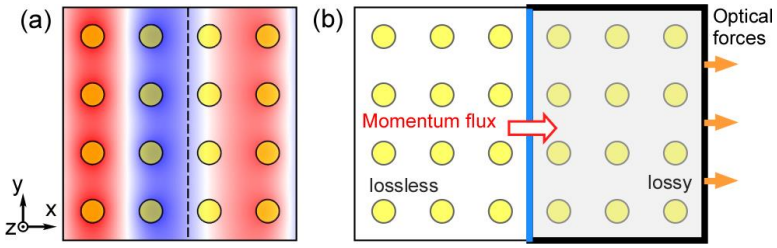

Figure 5.1: Momentum flux in a periodic medium. (a) Schematic of a 2D photonic crystal made of a square lattice of dielectric rods ($\epsilon_r = 13$) in air. The momentum flux across a plane entirely in air (dashed line along the y-z direction) is determined unambiguously. Red and blue regions represents strong positive and negative electric fields E_z of a TM mode propagating along the x direction. (b) The momentum flux across the interface (blue) equals to the average radiation pressure experienced by a perfect absorber.

[11] Numerically, the perfect absorber can be implemented in the form of a perfect matching layer with gradually increasing absorption along the propagation direction, similar to the ramped absorption in perfectly-matched layers [72].

Taking example of a z-polarized plane wave in free space, expressed as $E_z(\mathrm{x},\mathrm{y}) = E_0 e^{ik_x x + ik_y y - i\omega t}$, the power-normalized momentum flux across a y-z plane is

$$p_x = \frac{\int \frac{\epsilon_0}{2}\frac{k_x^2}{k_0^2}|E_z|^2 dydz}{\int \frac{1}{2\mu_0 c}\frac{k_x}{k_0}|E_z|^2 dydz} = \frac{k_x}{k_0}\cdot\frac{1}{c} \tag{5.5}$$

where k_x is the propagation constant in the axial direction, k_0 is the propagation constant of plane wave in free space, c is the speed of light. For normal incidence, the momentum flux of a plane wave reduces to $1/c$.

5.3 Plane-Wave Decomposition

For a plane wave, we can easily determine its momentum flux from the wavenumber (Eq.5.5). A Bloch mode is composed of many plane waves, where each plane wave have its own contribution to the momentum flux. Thus, plane wave composition uniquely determines the momentum flux of a Bloch mode. We will explore several different Bloch modes with their unique plane wave compositions and the associated momentum flux in Section 5.4. Here we explain the method for plane wave decomposition, to express the momentum flux in terms of the plane wave coefficients.

Let's consider the 2D photonic crystal structure as shown in Fig.5.1, but with oblique incidence (E_z field pattern shown in Fig.5.2a). The TM Bloch mode is unambiguously specified by its out-of-plane electrical field distribution E_z. We perform the expansion over a cross section at $x = x_0$ in the contiguous air region (could take any dashed lines shown in Fig. 5.2a). Bloch theorem provides a hint about the basis for the expansion: A Bloch mode with the Bloch k (k_x,k_y) can be decomposed into a Fourier series, represented by a series of $k_{y,n}$ separated by the reciprocal lattice constant $\frac{2\pi}{a}$.

$$E_z(y)|_{x=x_0} = e^{ik_x\cdot x_0}\cdot e^{ik_y\cdot x_0}\cdot u(x_0, y)$$

$$= e^{ik_x \cdot x_0} \cdot e^{ik_y \cdot x_0} \cdot \sum_n U_n(x_0) e^{i\frac{2\pi n}{a} y} = e^{ik_x \cdot x_0} \sum_n U_n(x_0) e^{ik_{y,n} \cdot y}$$

$$k_{y,n} = k_y + \frac{2\pi n}{a} \tag{5.6}$$

$$n \in N$$

The plane wave expansion that we need to use here is slightly different from Eq.5.6. Notice that the components in Eq.5.6 are not plane waves, because $k_x^2 + k_{y,n}^2 \neq k_0^2$, where k_x is the x component of the Bloch k, k_0 is the free space wavenumber. To obtain plane waves in the decomposition while taking advantage of the y-periodicity, we can keep the same series of $k_{y,n}$, but use $k_{x,n} = \sqrt{k_0^2 - k_{y,n}^2}$. The plane wave expansion is written as

$$E_z(y)|_{x=x_0} = \sum_n \left(A^+_{k_{y,n}} e^{ik_{x,n} \cdot x_0} + A^-_{k_{y,n}} e^{-ik_{x,n} \cdot x_0} \right) e^{ik_{y,n} \cdot y} \tag{5.7}$$

where $A^+_{k_{y,n}}$ and $A^-_{k_{y,n}}$ are the amplitudes of the forward and backward plane wave components, following $e^{ik_{x,n} \cdot x_0}$ and $e^{-ik_{x,n} \cdot x_0}$ respectively. As an example, the plane wave coefficients $A^{\pm}_{k_{y,n}}$ for the Bloch mode in Fig.5.2a is shown in Fig.5.2b. Here for the 2D bulk mode, we have only one propagating plane wave component ($k_{x,n} \in \mathbb{R}$, $|k_{y,n}| < k_0$) inside the light cone (orange shaded region in Fig.5.2b) while many evanescent plane wave components ($k_{x,n} \in \mathbb{I}$, $|k_{y,n}| > k_0$) outside of the light cone.

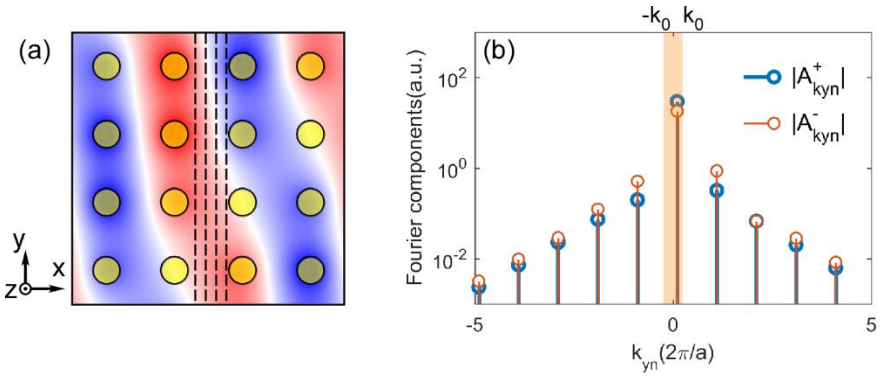

Figure 5.2: Plane wave expansion. (a) Field profile (Re{Ez}) in a 2D photonic crystal made of a square lattice of dielectric rods ($\epsilon_r = 13$) in air. The mode is taken along the 1st band, with a Bloch k of $(0.4,0.1)2\pi/a$. (b) Fourier coefficients from plane wave expansion at the dashed lines shown in (a).

Propagating plane waves and evanescent plane waves bring different characters to the momentum flux, as we will see later in Section 5.4. Separating the contributions from propagating plane waves and those from evanescent plane waves, the integrated time-averaged momentum flux and time-averaged optical power are expressed as:

$$F_x = \int_0^L \langle -T_{xx} \rangle dy = \int_0^L \frac{1}{4}\epsilon_0 \left(|E_z|^2 - c^2|B_x|^2 + c^2\left|B_y\right|^2 \right) dy$$

$$= \frac{La\epsilon_0}{2k_0^2}\left[\left(k_0^2 - k_{y,0}^2\right)\left(\left|A_{k_{y,0}}^+\right|^2 + \left|A_{k_{y,0}}^-\right|^2 \right) + \sum_{n\neq 0}\left(k_0^2 - k_{y,n}^2\right)\left(A_{k_{y,n}}^{-*}A_{k_{y,n}}^+ + A_{k_y}^{+*}A_{k_y}^- \right) \right] \tag{5.8}$$

$$I_x = \int_0^L \frac{1}{2} Re\{\boldsymbol{E} \times \boldsymbol{H}^*\}_x dy$$

$$= \frac{La}{2\mu_0 c}\left[\frac{k_{x,0}}{k_0}\left(\left|A_{k_{y,0}}^+\right|^2 - \left|A_{k_{y,0}}^-\right|^2 \right) + \sum_{n\neq 0}\frac{k_{x,n}}{k_0}\left(A_{k_{y,n}}^{-*}A_{k_{y,n}}^+ - A_{k_{y,n}}^{+*}A_{k_{y,n}}^- \right) \right] \tag{5.9}$$

L is the length of the cross section where the normalized momentum flux p_x (Eq.5.4) is being evaluated. The integration along the z direction is dropped for the 2D system.

5.4 Spectra of Normalized Momentum Flux

In this section, we visualize the normalized momentum flux as a function of frequency, namely, as a spectrum. The momentum flux does not follow the magnitude or the direction of the Bloch k, because the expression for momentum flux (Eq.5.8) share little in common with the Bloch k. We go through the Bloch modes composed of purely propagating plane waves, purely evanescent plane waves and a mixture of both. The propagating and evanescent plane waves bring very different contributions to the momentum flux.

5.4.1 Mode Composed of Purely Propagating Plane Waves

Some Bloch modes consist of purely propagating plane waves. The normalized momentum flux p_x of such modes is always positive in the direction of power flow.

Let's consider the Bloch modes in a 1D photonic crystal at normal incidence, i.e. $k_y = k_z = 0$. The field distribution is uniform along the cross section, and is the linear superposition of two counter-propagating plane waves, contributing disproportionately to the numerator and denominator of the normalized momentum flux $p_x = \frac{F_x}{I_x}$,

$$F_x = \frac{La\epsilon_0}{2}(|A_0^+|^2 + |A_0^-|^2) \tag{5.10}$$

$$I_x = \frac{La}{2\mu_0 c}(|A_0^+|^2 - |A_0^-|^2) \tag{5.11}$$

The normalized momentum flux p_x (Fig. 5.3c, f) range from 0 to infinity while the Bloch k (Fig.5.3b, e) take limited values within the Brillouin zone. For modes with positive group velocity, the normalized momentum flux is always positive while the Bloch k can take either sign. As the group velocity approaches zero, the power I_x carried by the mode approaches zero ($|A_0^+| \approx |A_0^-|$) while the integrated momentum flux F_x remain the same order of magnitude. The momentum flux spectrum is sensitive to the change of dielectric properties even for the same structure. As the permittivity of the dielectric layer increases from $3\epsilon_0$ (Fig.5.3a) to $13\epsilon_0$ (Fig.5.3d), the dispersion relations are compressed in the

frequency axis (from Fig.5.3b to Fig.5.3e), leading to smaller group velocities and smaller I_x given a fixed F_x. As a result, the momentum flux of the higher index structure (Fig.5.3f) is larger than the lower index structure (Fig.5.3c). Despite the magnitudes, the normalized momentum flux is in the same direction of the power flow (i.e. $p_x > 0$), because Eq.5.8 is always positive, while Eq.5.11 is positive in the propagation direction.

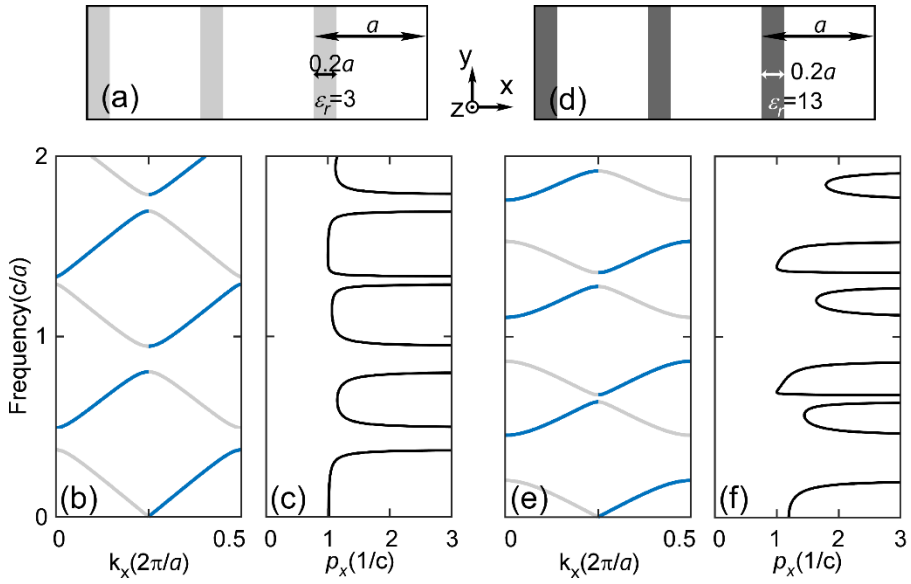

Figure 5.3: Band diagrams and normalized momentum flux of two 1D photonic crystals. (a,b) Schematics of the photonic crystals made of alternating layers of high-index and low-index (vacuum) materials. The high-index layer is 0.2a thick, with ϵ_r of 3 for (a) and 13 for (b). *a* is the lattice constant. (b,e) Band diagrams for K_x. Segments of the bands with positive group velocities are marked in blue. (c,f) Normalized momentum flux of the bands with positive group velocity.

5.4.2 Mode Composed of Purely Evanescent Plane Waves

Some Bloch modes consist of purely evanescent plane waves. The normalized momentum flux p_x of such modes can be either parallel or opposite to the direction of power flow, depending on the evanescent plane wave composition.

Let's consider the mode on the 3rd TM band along the **ΓX** direction of a 2D square lattice photonic crystal (Fig.5.4a,b). The calculated momentum flux spectrum (Fig.5.4c) is anti-symmetric with respect to the mid-frequency of the band $0.5343c/a$, being negative for the lower half and positive for the upper half of the band.

This mode can be described by tight binding model. The tight binding model predicts the complete dominance of evanescent plane waves as a result of nearest neighbor's evanescent coupling for this particular mode. It also quantitatively explains the spectrum of normalized momentum flux p_x (Fig.5.4c), by expressing it in terms of the frequency f. The reason that tight binding model is suitable for this mode is because the first-principle simulated dispersion relation (Fig.5.4b) can be perfectly fitted by

$$f = B - |C| \cdot \cos(k_x a) \tag{5.12}$$

where B is a constant representing the mid-frequency of the band, $|C|$ is a constant representing the coupling strength / the width of the band, k_x is the Bloch k. A curve fitting (Fig.5.4b) demonstrate good match of Eq.5.12, implying evanescent coupling of fields that are tight bonded to the dielectric rods.

To establish the relation between the normalized momentum flux p_x and the frequency f, we need to find the relation between p_x and k_x and then combine with Eq.5.12. We already know that p_x can be expressed in terms of plane wave components, which is determined by the wave function (E_z in this case), which can be explicitly modeled using tight bonding model for this particular mode. Suppose two neighboring columns of rods are located along $x = 0$ and $x = a$, the wave function (E_z) between $x = 0$ and $x = a$ can be approximated by

$$E_z = \sum_n g_n \cdot e^{ik_{y,n} \cdot y}\left(e^{-|k_{x,n}| \cdot x} + e^{i \cdot k_x \cdot a} e^{|k_{x,n}| \cdot (x-a)}\right) \tag{5.13}$$

while ignoring the fields localized around those rods further away. Here $k_{x,n} = \sqrt{k_0^2 - k_{y,n}^2} \in \mathbb{I}$. Eq.5.13 gives insights to understand both the momentum flux and power. Let's suppose for each $k_{y,n}$, the forward and backward components $A^+_{k_{y,n}}$ and $A^-_{k_{y,n}}$ have phases $\phi^+_{k_{y,n}}$ and $\phi^-_{k_{y,n}}$ respectively. We find the terms in momentum flux (Eq.5.8) and power (Eq.5.9) contributed from each $k_{y,n}$ explicitly depends on the relative phase $(\phi^+_{k_{y,n}} - \phi^-_{k_{y,n}})$

$$\int_0^L -T_{xx}dy\Big|_{k_{y,n}} = \frac{La\epsilon_0}{2}\frac{k_{x,n}^2}{k_0^2}\left(A^{-*}_{k_{y,n}}A^+_{k_{y,n}} + A^{+*}_{k_{y,n}}A^-_{k_{y,n}}\right)$$

$$= \frac{La\epsilon_0}{2}\frac{k_{x,n}^2}{k_0^2}\left|A^+_{k_{y,n}}\right|\left|A^-_{k_{y,n}}\right| 2\cos\left(\phi^+_{k_{y,n}} - \phi^-_{k_{y,n}}\right)$$

$$= -\frac{La\epsilon_0}{2}\frac{|k_{x,n}|^2}{k_0^2}\left|A^+_{k_{y,n}}\right|\left|A^-_{k_{y,n}}\right| 2\cos\left(\phi^+_{k_{y,n}} - \phi^-_{k_{y,n}}\right) \quad (5.14)$$

$$\int_0^L \frac{1}{2}Re\{\boldsymbol{E}\times\boldsymbol{H}^*\}_x dy\Big|_{k_{y,n}} = \frac{La}{2\mu_0 c}\frac{k_{x,n}}{k_0}\left|A^+_{k_{y,n}}\right|\left|A^-_{k_{y,n}}\right| 2i\sin\left(\phi^+_{k_{y,n}} - \phi^-_{k_{y,n}}\right)$$

$$= -\frac{La}{2\mu_0 c}\frac{|k_{x,n}|}{k_0}\left|A^+_{k_{y,n}}\right|\left|A^-_{k_{y,n}}\right| 2\sin\left(\phi^+_{k_{y,n}} - \phi^-_{k_{y,n}}\right) \quad (5.15)$$

The '−' sign in Eq.5.14 is due to $k_{x,n}^2 = k_0^2 - k_{y,n}^2 < 0$. The '−' sign in Eq.5.15 is due to $k_{x,n} \in \mathbb{I}$. Notice that in Eq.5.14, the evanescent components carry nonzero momentum flux through the interference of the evanescent tails $e^{|k_{x,n}|\cdot(x-a)}$ and $e^{-|k_{x,n}|\cdot x}$, although an isolated evanescent tail do not carry momentum flux. From a close examination on the decomposed terms, we find the relative phases between the forward and backward components $\left(\phi^+_{k_{y,n}} - \phi^-_{k_{y,n}}\right)$ for each $k_{y,n}$ have similar dependence on the Bloch k k_x, although $\phi^\pm_{k_{y,n}}$ can shift together by a phase $C_{k_{y,n}}$. As a consequence, $\left(\phi^+_{k_{y,n}} - \phi^-_{k_{y,n}}\right)$ for all $k_{y,n}$ can be treated equally, simplified into the form of $(\phi^+ - \phi^-) = -k_x a$. The normalized momentum flux p_x thus reduces to a simple dependence on the Bloch k k_x.

$$p_x = \frac{\sum_n \int_0^L -T_{xx}dy\Big|_{k_{y,n}}}{\sum_n \int_0^L \frac{1}{2}Re\{\boldsymbol{E}\times\boldsymbol{H}^*\}_x dy\Big|_{k_{y,n}}} = \frac{1}{c}\frac{\cos(\phi^+ - \phi^-)\sum_n \frac{|k_{x,n}|^2}{k_0^2}\left|A^+_{k_{y,n}}\right|\left|A^-_{k_{y,n}}\right|}{\sin(\phi^+ - \phi^-)\sum_n \frac{|k_{x,n}|}{k_0}\left|A^+_{k_{y,n}}\right|\left|A^-_{k_{y,n}}\right|}$$

$$\sim \cot(\phi^+ - \phi^-) = \cot(-k_x a) \tag{5.16}$$

Curve fitting the normalized momentum flux p_x versus the frequency f using Eq.5.12 &5.16 perfectly matches the momentum flux spectrum from first-principle simulation (Fig.5.4c). Due to the symmetry of trigonometric functions Eq.5.12&5.16, the spectrum of the momentum flux is anti-symmetric comparing the upper and lower half of the band (Fig.5.4c).

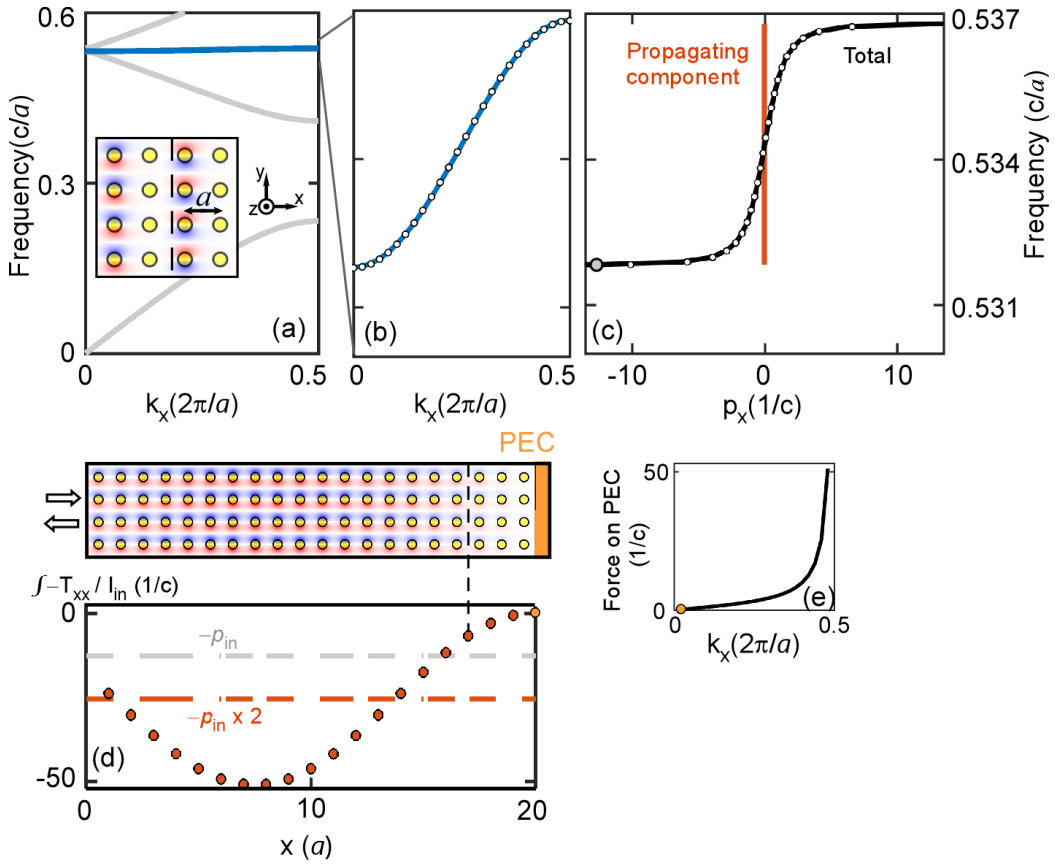

Figure 5.4: Band structures and momentum flux of Bloch mode in a 2D photonic crystal. (a) TM band diagram along the ΓX direction, with the 3rd TM band of interest highlighted in blue. Inset shows the Ez field and the structure of the 2D crystal at $= (0.25, 0) \cdot 2\pi/a$. (b) Magnified band diagram of the 3rd TM band (blue curve), which agrees with the tight binding model (circles). (c) Normalized momentum flux of the 3rd TM band (black curve), which agrees with the tight binding model (circles). The propagating plane waves (red curve) have 0 contribution. (d) Normalized momentum flux (red dots in lower panel) in a photonic crystal truncated by a perfect electrical conductor (PEC). The momentum flux is calculated from the MST obtained from the field pattern (upper panel) integrated over a corresponding cross section (black dashed line). The incident wave is indicate by a grey dot in the band structure (c), with $k_x = 0.02 \cdot 2\pi/a$. (e) Forces on the PEC plate for different Bloch k. The yellow dots in (e) and (d) correspond to each other.

Negative momentum flux indicates pulling forces on a perfect absorber. However, momentum flux is not additive. When multiple Bloch modes are present, the total

momentum flux is not simply the sum of the individual mode. One important example is that negative momentum flux does not result in a negative (pulling) force on a perfectly reflecting mirror that terminates the periodic medium (see proof in Section 5.7.1). Consider a bulk photonic crystal mode with negative momentum flux ($k_x = 0.02 \cdot 2\pi/a$ gray dot in Fig.5.4c). We calculate the momentum flux normalized to 1W of incident wave at multiple coordinates (Fig.5.4d, each dot correspond to one evaluation along a dashed line). Each evaluation indicates the forces applied on the structure on the right hand side of the corresponding dashed line. The momentum flux oscillate with periodicity $\frac{2\pi}{2k_x}$ due to the interference of the incident and reflected waves (see proof in Section 5.7.2). As the bulk photonic crystal encounters the PEC plate, the mode is entirely reflected and result in a positive force on the PEC plate (yellow dot in Fig.5.4d). Meanwhile, the net force is negative (red dashed line in Fig.5.4d) in order to balance out the change of momentum flux from the incident wave to the reflected wave. The value of the net force is 2x the normalized momentum flux of the incident wave (gray dashed line in Fig.5.4d). The net force includes negative force distributed over the rods in the near field of the mirror and the positive force on the PEC plate.

The force on the PEC plate is always positive and increases from 0 to infinity for k_x from 0 to $0.5 \cdot 2\pi/a$ (Fig.5.4e).

5.4.3 Mode Composed of Both Propagating and Evanescent Plane Waves

A broader range of Bloch modes consist of a mixture of the propagating and the evanescent plane waves. For these modes, the direction of momentum flux is determined by which component dominates and whether the evanescent part makes a negative contribution.

Let's consider the guided modes in photonic crystal line defect waveguides. Unlike the bulk modes, these defect modes do not have discrete translational symmetry in the y direction. Therefore the plane wave components take continuous values in $k_{y,n}$, i.e., n no longer take integer values, and $k_{y,n}$ is no longer discrete. Here the momentum flux (Eq.5.8) and optical power (Eq.5.9) are instead expressed in the integration form

$$F_x = \frac{La\epsilon_0}{2}\frac{1}{k_0^2}\left[\int_{-k_0}^{k_0}\left(k_0^2 - k_{y,n}^2\right)\left(\left|A_{k_{y,n}}^{+}\right|^2 + \left|A_{k_{y,n}}^{-}\right|^2\right)dk_{y,n} + \int_{-\infty}^{-k_0}\left(k_0^2 - k_{y,n}^2\right)\left(A_{k_y}^{-*}A_{k_y}^{+} + A_{k_{y,n}}^{+*}A_{k_{y,n}}^{-}\right)dk_{y,n} + \int_{k_0}^{+\infty}\left(k_0^2 - k_{y,n}^2\right)\left(A_{k_y}^{-*}A_{k_y}^{+} + A_{k_{y,n}}^{+*}A_{k_{y,n}}^{-}\right)dk_{y,n}\right] \tag{5.17}$$

$$I_x = \frac{La}{2\mu_0 c}\left[\int_{-k_0}^{k_0}\frac{k_{x,n}}{k_0}\left(\left|A_{k_{y,n}}^{+}\right|^2 - \left|A_{k_{y,n}}^{-}\right|^2\right)dk_{y,n} + \int_{-\infty}^{-k_0}\frac{k_{x,n}}{k_0}\left(A_{k_{y,n}}^{-*}A_{k_{y,n}}^{+} - A_{k_{y,n}}^{+*}A_{k_{y,n}}^{-}\right)dk_{y,n} + \int_{k_0}^{+\infty}\frac{k_{x,n}}{k_0}\left(A_{k_{y,n}}^{-*}A_{k_{y,n}}^{+} - A_{k_{y,n}}^{+*}A_{k_{y,n}}^{-}\right)dk_{y,n}\right] \tag{5.18}$$

For a guided mode in a reciprocal photonic crystal defect waveguide (Fig.5.5a,b), the plane-wave expansion yields a continuum of $k_{y,n}$. The defect waveguide is created by removing one row of rods from the photonic crystal, creating a defect with size of $d = 2a$ from center to center of the rods facing the defect. We have separately plotted the propagating and evanescent plane waves' contributions to the normalized momentum flux (Fig.5.5c). The sign and magnitude of the total normalized momentum flux p_x is

determined by the dominating contribution among the propagating and evanescent waves. As indicated in Section 5.4.1, the contribution from the propagating plane waves (red line) is always positive. As indicated in Section 5.4.2, the contribution from the evanescent plane waves (green line) can take either sign. In a narrow range of frequency around 0.3c/a the total momentum flux is negative, as the negative contribution from the evanescent waves dominates over the positive contribution from the propagating waves (Fig.5.5c).

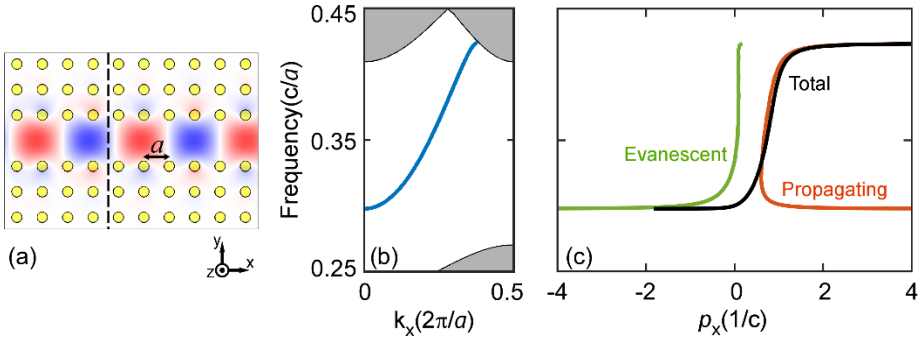

Figure 5.5: Band diagram and normalized momentum flux of a defect waveguide mode. (a) E_z field profile of the defect waveguide mode at frequency $0.36c/a$, in the first bandgap. The bulk photonic crystal is made of a square lattice of rods with $\epsilon_r = 13$ and radius $r = 0.2a$. The size of the line defect is $d = 2a$ from center to center (b) The defect waveguide band (blue line) and projected bulk bands (gray shaded area). (c) Normalized momentum flux of the waveguide mode. The partial sum of propagating plane waves (red line) is positive. The partial sum of evanescent plane waves (green line) can take either sign.

In contrast to the reciprocal defect waveguide mode mentioned above, a one-way defect waveguide mode (chiral edge state from Chapter 3) can never have negative momentum flux (Fig.5.6b), due to the dominance of the contribution from the propagating plane waves. One-way chiral edge states are special guided modes that are topologically protected from being reflected by any non-magnetic defect. They exist at the edge of magneto-optical photonic crystals, or domain walls between regions with opposite

magnetic biases. Here we use square lattices of yttrium iron garnet (YIG) ferrite rods[17]. The relative permittivity and permeability of YIG for the lower photonic crystal is $\epsilon_r = 15$ and $\mu_r = \begin{bmatrix} 14 & i12.4 & 0 \\ -i12.4 & 14 & 0 \\ 0 & 0 & 1 \end{bmatrix}$ using 0.2T of external DC magnetic field, around operating frequency of 0.45 GHz. The upper photonic crystal is applied with the opposite DC magnetic field, and the sign of off-diagonal elements in the μ tensor is reversed. A waveguide is formed from a line defect between the two crystals with a center-to-center distance of $1.5a$ between the rods facing the defect. On each side, the photonic crystal has Chern numbers of $+1$ and -1 respectively, therefore supporting two one-way modes at the interface. The two modes split into an odd mode (Fig.5.6a orange curve and Fig.5.6b inset) and an even mode (Fig.5.6a blue curve and Fig.5.6b inset) due to symmetry. Because the waveguide mode with negative group velocity do not exist (Fig.5.6a) for both of the one-way modes, the group velocity never reaches zero, requiring the propagating plane waves to dominate over the evanescent waves, which leads to an overall positive momentum flux (Fig.5.6b), although the evanescent wave can have negative contribution (Fig.5.6c). Similar to the bulk modes studied previously in 1D and 2D photonic crystals, here the normalized momentum flux of the defect waveguide modes also diverges as the group velocity infinitely approaches zero (Fig.5.6b) when the defect waveguide modes are merging into bulk bands (Fig.5.6a). Near the band-edge, the group velocity of the waveguide modes infinitely approaches zero due to the anti-crossing against the bulk modes, while never reaches zero due to the one-way nature.

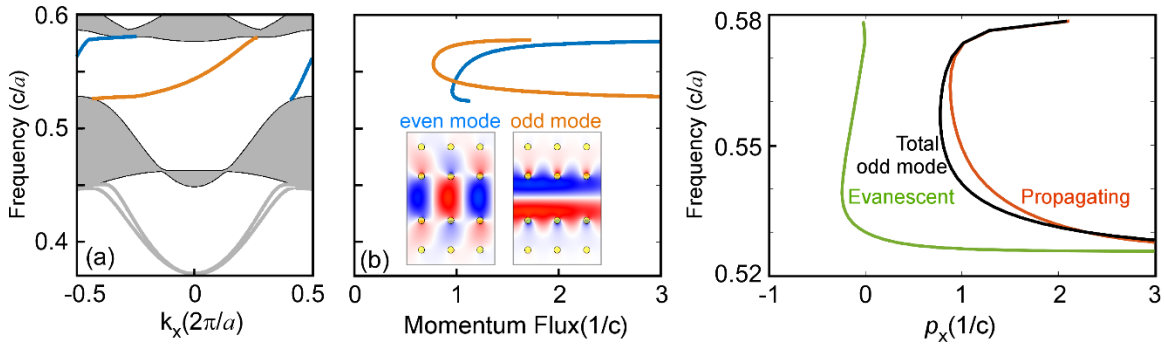

Figure 5.6: Band diagram and normalized momentum flux of one-way edge modes. (a) Projected band diagram and (b) normalized momentum flux of the one-way edge mode at a domain wall separating two magneto-optical photonic crystals with opposite magnetization. Two distinct edge modes, an even mode (blue) and an odd mode (orange), propagate along the same direction. Inset shows the structure of the photonic crystal and calculated E_z field patterns at frequency $0.54\ c/a$. Projected bulk bands and two-way defect modes are shown in grey. (c) Normalized momentum flux of the odd mode and its decomposition into the propagating and evanescent contributions.

5.5 The Conservation of Momentum Flux and Optical Forces

In this section we demonstrate the conservation of momentum flux and the resultant optical forces under scattering, mode conversion, reflection and transmission in periodic structures.

The direction and magnitude of the optical forces are determined by the change in momentum flux. Consider a Bloch wave traveling from region 1 to region 2, where the two regions can be of the same material separated by a defect, or different materials separated by an interface, leading to scattering, reflection or mode conversions. As a result, region 1 and region 2 would have different momentum flux MF_1 and MF_2. A total optical force of $MF_1 - MF_2$ would be distributed to the near field.

First we show a simple example of momentum flux conservation involving no reflection but just mode conversion, under the topologically protected scattering between one-way modes. The system consists of a one way waveguide (as shown in Fig.5.7) and a

point defect, i.e. a particle inside the waveguide. The one-way waveguide supports two modes (odd and even) as shown in Fig.5.6. One of the modes is chosen as the input, which is partly scattered into the other mode by the particle while both modes keep propagating forward. The total force incurred due to scattering (circles in Fig.5.7b, calculated from MST) is distributed onto both the particle and the photonic crystal structures in the near field region (shaded in gray in Fig.5.7a), and is equal to the change in momentum flux. Quantitatively, as a fraction S of the incident odd mode is scattered into the even mode, we have $MF_1 = p_{odd}$, $MF_2 = (1-S)\cdot p_{odd} + S\cdot p_{even}$. The total optical force equals to the change in momentum flux $F_{total} = S\cdot(p_{odd} - p_{even})$ (solid lines in Fig.5.7b, calculated from S, p_{odd} and p_{even}). It is vice versa for the case of even mode incidence. To be noticed, this is a special case where momentum flux is additive. Because the even and odd modes have opposite symmetry and their fields are orthogonal at each cross section. In consequence, unlike the oscillations observed in Fig.5.4d, the momentum flux is a constant when we measure it at a spacing of the lattice constant a, in the region where the odd and even modes coexist.

There are two interesting observations. First, the forces on a particle (dotted lines in Fig.5.7b, calculated from MST) differ significantly from the total force (circles in Fig.5.7b). The total force is determined by momentum conservation whereas the force on the particle is largely determined by the Bloch k and the unit cell function (Chapter 3.3). Second, the spatial symmetry of the force on the particle and the total force are different. The force on the particle comparing using the odd or the even mode as the incidence is not simply opposite to each other, except for when the particle is placed on special symmetric planes (i.e., $x = Na$ and $Na + \frac{1}{2}$, $N \in \mathbb{N}$). This is because the force on the particle is sensitive to the near field. However, the total force on the entire region is opposite with equal magnitudes comparing the odd and even incidence, no matter where the particle is

placed. This is because symmetry guarantees that the power scattered from the incident mode into the other mode stays the same for the two cases, leading to the same magnitude of change in momentum flux.

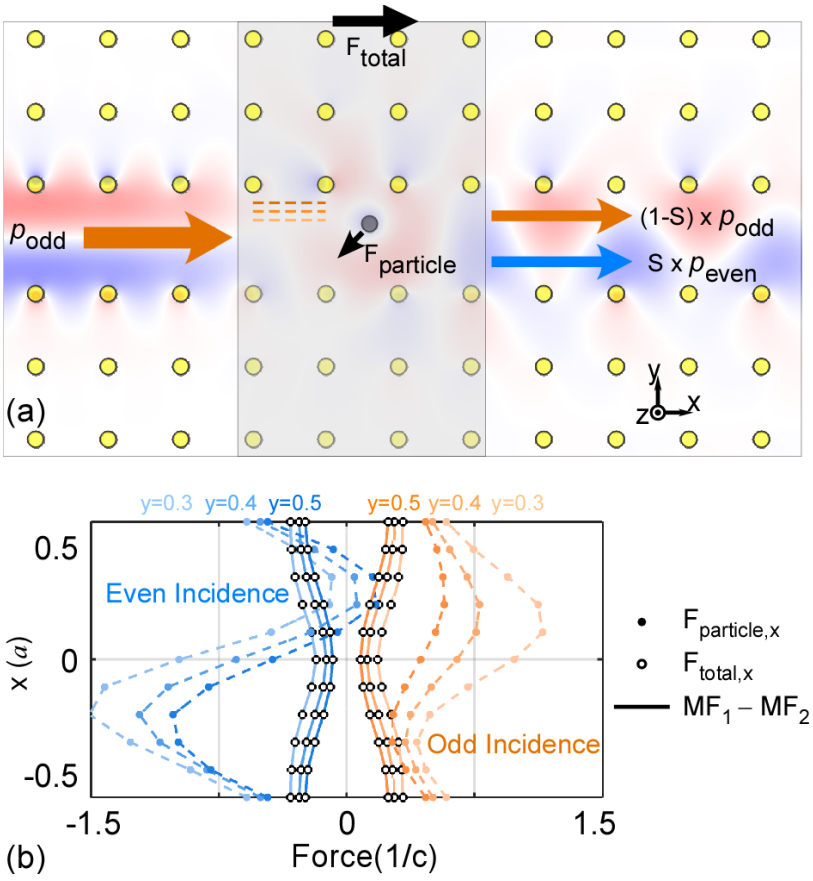

Figure 5.7: Momentum flux conservation in a one way waveguide with scattering and mode conversion due to a defect (the particle). (a) Schematic diagram of the scattering on top of the E_z field with odd mode incidence at $f = 0.55c/a$. The one-way mode (as described by Fig.5.6a) encounters a point defect, i.e., a dielectric particle ($\epsilon_r = 13$, radius $r = 0.1a$), which scatters an S fraction of power into the other mode, causing changes in the momentum flux. The momentum flux carried by each mode at each segment of the waveguide are marked next to the arrows representing the modes. The particle experiences a force $F_{particle}$, which is distinguished from the total force F_{net} experienced by the near field region (shaded in gray). (b) Momentum conservation and scattering forces using the odd (orange) and the even (blue) mode as incidence respectively. The axial total force $F_{total,x}$ (circles, calculated from MST) equals to the change in momentum flux (lines, calculated from the momentum flux spectra shown in Fig.5.6b). The particle experiences a significantly different force $F_{particle,x}$ (dots, calculated from MST).

We next show the conservation of momentum flux at a waveguide connection with both reflection and mode conversion. Consider a junction between two photonic crystal waveguides with different widths ($2a$ and $4a$ respectively) (Fig.5.8). To ensure significant power transmission, a pair of rods at the end of the narrower waveguide is enlarged. The two segments of waveguides support different modes of different dispersion relations (Fig.5.8a,b) and different normalized momentum flux (Fig.5.8c). At the junction, the incident mode experiences partial reflection into the upstream and mode conversion into the downstream region[12], generating forces that are distributed over a few columns of rods near the waveguide junction (shaded in gray in Fig.5.8d, e). The total force equals to the momentum flux in the upstream region minus that in the downstream region. Suppose 1[W] of mode 1 with normalized momentum flux p_1 encounters R[W] of reflection and T[W] of conversion into mode 2, where mode 2 has normalized momentum flux p_2. The momentum flux in the upstream and the downstream regions would be $p_1 \cdot (1+R)$ and $p_2 \cdot T$ respectively (dashed lines, Fig.5.8d,e). The total optical force is $F_{total} = p_1 \cdot (1+R) - p_2 \cdot T$, equaling to the sum of the contributions from both reflection $p_1 \cdot 2R$ and mode conversion $(p_1 - p_2) \cdot T$. The momentum flux in the entire upstream region (dots, Fig.5.8d,e for $x < 30a$) oscillate with periodicity $\frac{2\pi}{2k_x}$ due to the interference of the incident and reflected waves. Thus the rods in the entire upstream region experience periodic axial forces which average to 0 (bar graph, Fig.5.8d,e, for $x < 30a$). In the near field of the junction (gray shaded region, Fig.5.8d,e), the momentum flux can fluctuate. The local force can be significantly greater in magnitude than the total force, and can be opposite in signs (Fig.5.8d, for x in $30\sim35a$). This brings significant degree of freedom in the engineering for local forces even in the simple interface. For example, at the

[12] In the downstream region, only the waveguide mode colored in blue in Fig.5.8b is generated. Other waveguide modes (colored in grey in Fig.5.8b) are not generated due to either symmetry mismatch or frequency mismatch.

frequency of $0.36 \cdot c/a$ (Fig.5.8d), the total force on the junction as a whole is tensile, but locally the forces rapidly flip sign near the end of the narrower waveguide. The force on the wider waveguide alone is repulsive but negligible. At the frequency of $0.3 \cdot c/a$ (Fig.5.8e), the total force on the junction as a whole is compressive and mostly distributed near the end of the narrower waveguide. The force on the wider waveguide along is attractive but negligible.

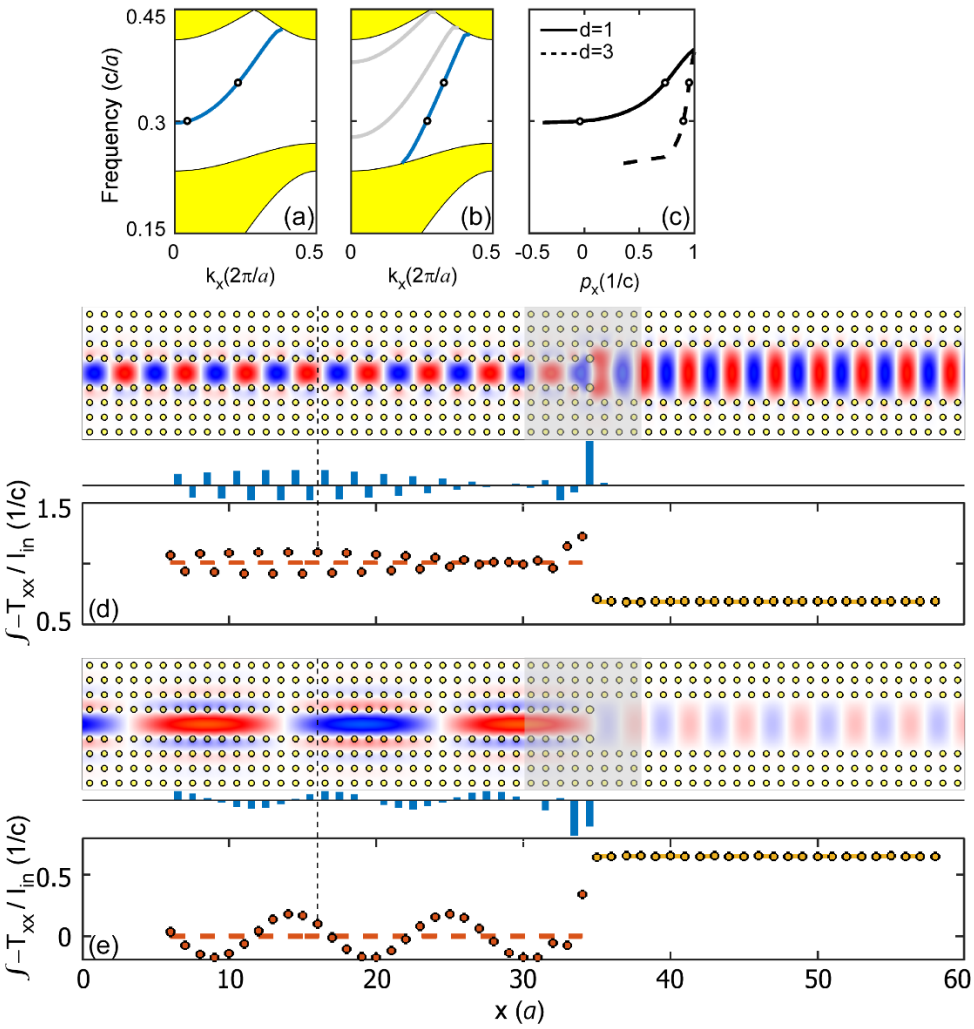

Figure 5.8: Momentum flux conservation at a waveguide junction (mode convertor). (a,b) Projected band diagrams of the waveguides before and after the junction. The waveguides are line defects in the photonic crystal described in Fig.5.5, with different widths of $2a$ and $4a$ respectively. Blue curves indicate the waveguide modes involved. (c) Momentum flux spectra of the two fundamental modes. (d,e) E_z field patterns (upper panel), force on each column of rods(middle panel), average momentum flux (dashed line, lower panel) calculated from the momentum flux spectra in (c), and momentum flux (circles, lower panel) at various x locations calculated from the MST integrated over the waveguide cross section (an example shown as the black dashed line) at two excitation frequencies: (d) $0.36\ c/a$ and (e) $0.3c/a$. The fundamental modes at these two frequencies are indicated as circles in panels (a-c).

Similarly, we can predict the forces at waveguide end facets (Fig.5.9) according to the conservation of momentum flux. The upstream waveguide in Fig.5.9 is identical to the narrower one in Fig.5.8, with normalized momentum flux illustrated in Fig.5.8c. The downstream is free space, with a normalized momentum flux less than $1/c$ due to the scattering of plane waves into multiple directions. Tensile net force occurs due to the change of momentum flux for the frequency at $0.36 \cdot c/a$ (Fig.5.9a) while compressive net force occurs for the frequency at $0.36 \cdot c/a$ (Fig.5.9b). The reflection causes the entire upstream region to experience periodic axial forces which average to 0 (bar graph, Fig.5.9, for $x < 33a$). The net force is majorly distributed in the near field of the end facet (Fig.5.9a,b, for x in $33\sim35a$).

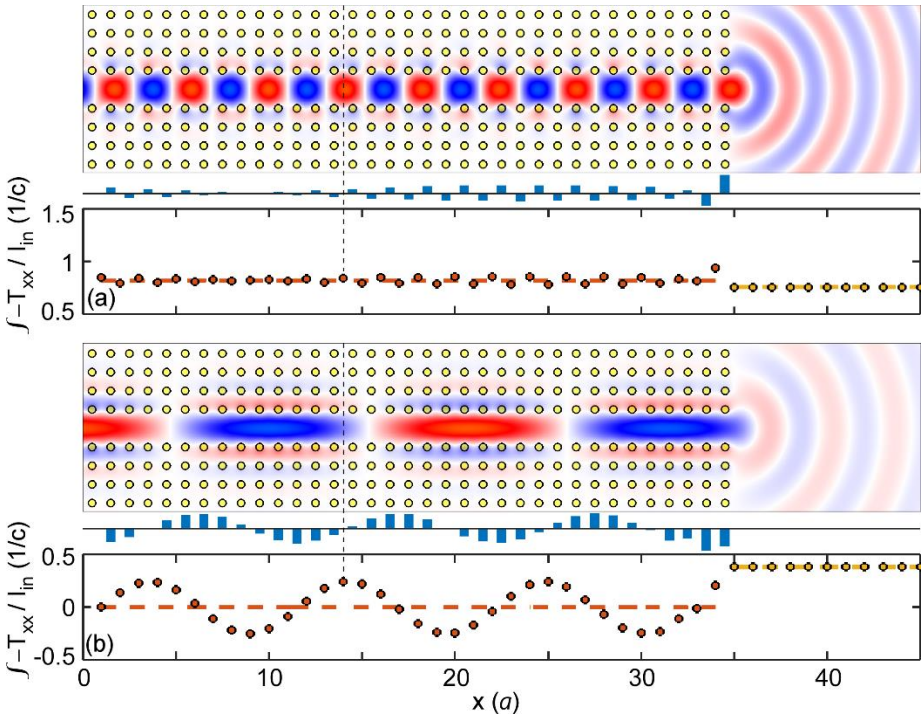

Figure 5.9: Momentum flux conservation at the end facet of a truncated waveguide. (a,b) E_z field patterns (upper panel), force on each column of rods(middle panel), average momentum flux (dashed line, lower panel) calculated from the momentum flux spectra given in Fig.5.8c, and momentum flux (circles, lower panel) at various x locations calculated from the MST integrated over the waveguide cross section (an example shown as the black dashed line) at two excitation frequencies: (a) $0.36c/a$ and (b) $0.3c/a$. The fundamental modes at these two frequencies are indicated by dots in Fig.5.8a.

5.6 Concluding Remarks

We studied the linear momentum flux for Bloch modes in periodic structure. Momentum flux is an intrinsic property of Bloch modes, representing its ability to apply optical forces on a perfect absorber. The spectra of momentum flux differ significantly from the spectra of the canonical momentum (i.e. the Bloch k), in both the magnitude and sign. Moreover, the momentum flux can diverge near band edge, which indicates enhanced forces on a perfect absorber. We analyzed the momentum flux by decomposing it into contributions from underlying plane wave components, including both the propagating and

the evanescent plane waves. Interestingly, negative momentum flux are found for Bloch modes in both bulk photonic crystal and defect waveguides, attributing to special formations of evanescent plane wave components. The conservation of momentum flux can be used to predict the total force in a variety of scenarios such as scattering, mode conversion, reflection and transmission, as the light encounters defects or interfaces. The total force equals to the change in momentum flux, and is distributed over all the objects in the near field. Negative total force arises from a decrease in momentum flux, while not necessarily from an incoming mode that carries negative momentum flux. Compressive/expansion forces can be predicted from the change of momentum flux at interfaces.

By revisiting the Chapter 3 case of inter-mode scattering in a one-way waveguide, we find the momentum conservation approach is not a good choice for predicting the direction of forces on the particle inside the waveguide. Because the force predicted by the change in momentum flux is distributed over both the particle and the near field photonic crystal structures. While the individual force on each object can only be wisely predicted using RTOF[42], the virtual work approach.

There are still some parallels between the momentum flux analysis in this chapter and the pulling/pushing forces analysis in Chapter 3&4. In both cases, the Fourier series of the unit cell function reveal important information. Here we perform a Fourier transform in the transverse direction, and the Fourier series coefficients determine the exact value of the momentum flux. In the pulling/pushing forces analysis, the Fourier transform is performed longitudinally, the strongest order of the Fourier series determines which Brillouin zone we use to identify the authentic wavenumbers.

5.7 APPENDIX

5.7.1 Forces on PEC from Plane Wave Components

Prove that the forces on PEC are always positive in the classical limit, irrespective of the plane wave composition of the incoming Bloch mode.

The incident mode consist of purely evanescent waves, and carries the following momentum flux

$$\int_0^L \langle -T_{xx} \rangle dy = La\frac{\epsilon_0}{2}\left\{\sum_{n\neq 0}\frac{k_{x,n}^2}{k_0^2}\left[A_{k_{y,n}}^{-*}A_{k_{y,n}}^{+} + A_{k_{y,n}}^{+*}A_{k_{y,n}}^{-}\right]\right\} \tag{5.19}$$

where $k_{x,n}^2 = k_0^2 - k_{y,n}^2$. Because $A_{k_{y,n}}^{-*}A_{k_{y,n}}^{+} + A_{k_{y,n}}^{+*}A_{k_{y,n}}^{-} \in \mathbb{R}$, we have the following

$$A_{k_{y,n}}^{-*}A_{k_{y,n}}^{+} = C_1 + i\cdot C_2,\ A_{k_{y,n}}^{+*}A_{k_{y,n}}^{-} = C_1 - i\cdot C_2 \tag{5.20}$$

where $C_1, C_2 \in \mathbb{R}$. Assuming

$$A_{k_{y,n}}^{+} = p^+ + iq^+,\ A_{k_y}^{-} = p^- + iq^- \tag{5.21}$$

where $p, q \in \mathbb{R}$, we have

$$p^-p^+ + q^-q^+ = C_1\ ,\ p^-q^+ - p^+q^- = C_2 \tag{5.22}$$

Combining the incident wave with the reflected wave we get the following momentum flux

$$\begin{aligned}\int_0^L \langle -T_{xx} \rangle dy &= La\frac{\epsilon_0}{2}\left\{\sum_{n\neq 0}\frac{k_{x,n}^2}{k_0^2}\left[\left(A_{k_{y,n}}^{-*} + A_{k_{y,n}}^{+*}\right)\left(A_{k_{y,n}}^{+} + A_{k_{y,n}}^{-}\right)\right.\right.\\ &\left.\left. + \left(A_{k_{y,n}}^{+*} + A_{k_{y,n}}^{-*}\right)\left(A_{k_{y,n}}^{-} + A_{k_{y,n}}^{+}\right)\right]\right\}\\ &= La\epsilon_0\sum_{|k_y|>k}\frac{k_x^2}{k^2}\left[A_{k_{y,n}}^{-*}A_{k_{y,n}}^{+} + A_{k_{y,n}}^{+*}A_{k_{y,n}}^{-} - \left|A_{k_{y,n}}^{-}\right|^2 - \left|A_{k_{y,n}}^{+}\right|^2\right]\end{aligned} \tag{5.23}$$

Applying Eq.5.20-5.22

$$\begin{aligned}\left|A_{k_{y,n}}^{-}\right|^2 + \left|A_{k_{y,n}}^{+}\right|^2 &= p^{+2} + q^{+2} + p^{-2} + q^{-2}\\ A_{k_{y,n}}^{-*}A_{k_{y,n}}^{+} + A_{k_{y,n}}^{+*}A_{k_{y,n}}^{-} &= 2C_1 = 2p^+p^- + 2q^+q^-\\ p^{+2} + q^{+2} + p^{-2} + q^{-2} &\geq 2p^+p^- + 2q^+q^-\\ \Rightarrow A_{k_{y,n}}^{-*}A_{k_{y,n}}^{+} + A_{k_{y,n}}^{+*}A_{k_{y,n}}^{-} - \left|A_{k_{y,n}}^{-}\right|^2 - \left|A_{k_{y,n}}^{+}\right|^2 &\leq 0\end{aligned} \tag{5.24}$$

Using $k_{x,n}^2 < 0$ and Eq.5.24, we find Eq.5.23≥ 0. So the forces on PEC are always positive in the classical limit, irrespective of the underlying plane wave composition and normalized momentum flux of the incoming Bloch mode.

5.7.2 Interference Pattern of Momentum Flux upon Reflection

Prove that when a Bloch mode is reflected, the momentum flux in the upstream region, measured at the spacing of lattice constant a, has a periodicity of $2\pi/2k_x$ due to interference, where k_x is the Bloch k.

Without loss of generality, we use the TM polarized Bloch mode. According to the expression of Maxwell stress tensor

$$\left\langle \int_0^L -T_{xx}dy \right\rangle = \int_0^L \frac{1}{4}\epsilon_0 \left(|E_z|^2 - c^2|B_x|^2 + c^2\left|B_y\right|^2 \right) dy$$

The periodicity of $\left\langle \int_0^L -T_{xx}dy \right\rangle$ follows the periodicity of E_z, B_x, B_y. Since B_x, B_y have the same periodicity as E_z. We only need to explore the periodicity of E_z. Considering both the incoming Bloch mode (k_x) and its reflection ($-k_x$), the total electric field is a superposition

$$E_z^{(total)} = u_{k_x}(x,y)\cdot e^{i\cdot k_x\cdot x} + r\cdot u_{-k_x}(x,y)\cdot e^{-i\cdot k_x\cdot x}$$

where r is the reflection coefficient, $u_{k_x}(x,y)$ is the unit cell function. Using the periodicity and reciprocity of the Bloch mode we have

$$u_{k_x}(x,y) = u_{k_x}(x+a,y),\ u_{k_x}(x,y) = u_{-k_x}^*(x,y)$$

$$\Rightarrow E_z^{(total)}(x,y) = u_{K_x}(x,y)\cdot e^{i\cdot K_x\cdot x} + r\cdot u_{K_x}^*(x,y)\cdot e^{-i\cdot K_x\cdot x}$$

$$\left|E_z^{(total)}(x,y)\right|^2 = \left|u_{k_x}\right|^2 + |r|^2\cdot\left|u_{k_x}(x,y)\right|^2$$

$$+u_{k_x}^*(x,y)\cdot e^{-i\cdot k_x\cdot x}\cdot r\cdot u_{k_x}^*(x,y)\cdot e^{-i\cdot k_x\cdot x}$$

$$+u_{k_x}(x,y)\cdot e^{i\cdot k_x\cdot x}\cdot r^*\cdot u_{k_x}(x,y)\cdot e^{i\cdot k_x\cdot x}$$

Evaluating $\left|E_z^{(total)}(x,y)\right|^2$ at sampling points spaced by the lattice constant a, we can observe a wavenumber of $2k_x$, without seeing the influence from the unit cell function u_{k_x}.

Therefore for the reciprocal Bloch modes in Fig.5.4,5.8,5.9, $\left\langle \int_0^L -T_{xx}dy \right\rangle$ has a periodicity of $2\pi/2k_x$ along the x direction, evaluated at sampling points spaced by the lattice constant a.

Chapter 6: Photonic Motor Around a Phase Singularity in Photonic Crystal Cavity

6.1 INTRODUCTION

Angular momentum can be exchanged between electromagnetic field and mechanical degrees of freedom [123], [124], leading to contact-free photonic motors or rotators. For example, the transfer of orbital angular momentum can drive Mie test particles into cyclic motion[64], [123], or drive windmill shaped particles into rotation [125] [126] [127] that can stir the surrounding liquid. The transfer of spin angular momentum can rotate chiral particles [128] or birefringent particles [129], which have been used to measure the rotational tensile properties of large molecules such as DNA[130].

Recently, integrated photonics have brought new solutions to a variety of applications with the benefit of small footprint, low cost and high reliability[131]. In particular, photonic crystals offer great potentials in tailoring the electromagnetic field[110] and optomechanical interactions [95], [116]. For example, optical trapping have been experimentally demonstrated using resonance enhanced fields in a photonic crystal cavity[75]. Robust and long range pulling forces have been theoretically demonstrated using forward scattering in photonic crystal waveguides (Chapter 3,4 [95], [116]). Can we also transfer angular momentum to objects using the electromagnetic fields that are entirely defined by the photonic crystal structures?

We propose a setup that can trap and apply torque on a lossy particle around a phase singularity in a photonic crystal cavity. The setup can be viewed as an analogy to a free space system, where a lossy probe particle is driven into cyclic motion by helical modes [64], [65]. The amplitude of the free-space helical mode has an angular dependence of $e^{im\theta}$, where m is known as a topological charge associated with the orbital angular momentum of light. For $m \neq 0$, a phase singularity exists at the center of the beam and

the light field carries an angular momentum flux of $\frac{I}{\omega}m$. Through absorption, the angular momentum flux of light partially transfers to the torque on the lossy particle, proportional to the power being absorbed ($\sim 25\%$) [64]. In the photonic crystal defect cavity, we can also find an Eigen mode (Fig.6.1a) whose electric field E_z have the angular dependence of $e^{im\theta}$ (TM polarization), with a phase singularity at the center of the cavity. The radial field distribution of the cavity mode is perfect for trapping a dielectric particle in a circular orbit (Fig.6.1a). However, predicting the torque on the particle in such photonic crystal system is quite different from that in free space. As we have discussed in Chapter 5, in photonic crystal waveguide, the change in momentum flux of the electromagnetic field is transferred to forces on both the particle and the photonic crustal structure. Here, the change in angular momentum flux of the electromagnetic field is also transferred to torques on both the particle and the photonic crystal structure. Therefore, we need to use RTOF to rigorously predict the torque on the particle. From RTOF, we know that singularity in the phase response of well-defined ports can lead to photonic motoring effect [43]. We will demonstrate the lossy particle becomes a port that perceives the singularity of the field into its phase response, which leads to a force field with curl, i.e. torque applied on the particle (Section 6.2). We also give a theoretical upper bound of the torque in our system, where the cavity mode is excited by a single port (Section 6.3).

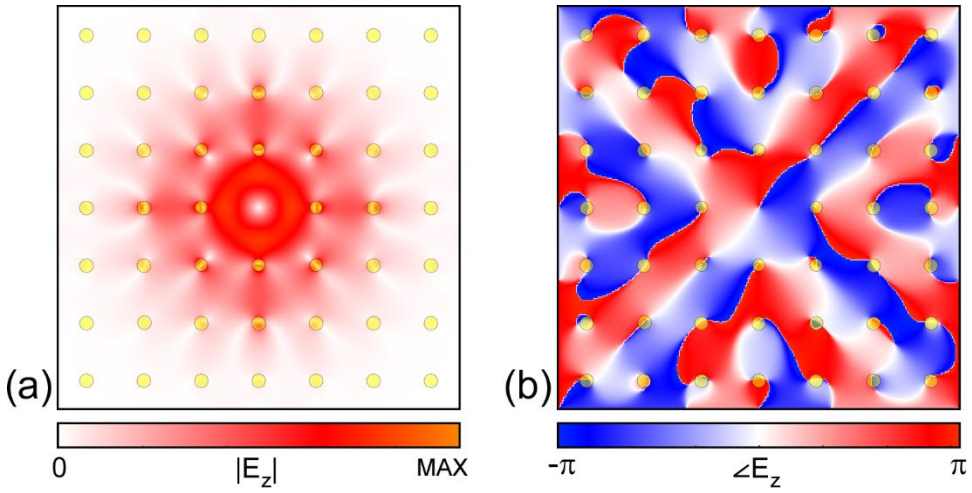

Figure 6.1: Absolute value (a) and phase (b) of E_z field of the Eigen mode in the photonic crystal point defect cavity (TM polarization, $f = 0.516c/a$). One rod is removed from the bulk photonic crystal to form the defect cavity. The photonic crystal consists of magneto-optical rods with same material as those used in Chapter 3 ($\epsilon_{11} = \epsilon_{22} = \epsilon_{33} = 15.0\epsilon_0$, $\mu_{11} = \mu_{22} = \mu_{33} = 14.0\mu_0$, $\mu_{12} = -\mu_{21} = -12.4i \cdot \mu_0$). The inner most 8 rods have radius $r = 0.11a$, other rods have radius $r = 0.12a$. (Eigen value study)

6.2 Torque Induced by Singularity in the Phase Responses

Similar to Chapter 3.6, we apply RTOF to predict the forces on a small lossy particle. As the lossy particle is treated as a perturbation to the field, it serves as a lossy port that absorbs the light with a phase following the phase of the electromagnetic field at where it is situated. The power and phase responses of the lossy port (particle) versus the displacement of itself determines the photonic force on the particle, if other ports have no significant contribution. We use this property to design the photonic motor.

When the lossy particle is trapped on a circular orbit of radius r_{orbit}, imagine it takes a positive angular displacement $\Delta\theta$, the lossy port that travels with the particle will experience a phase shift of $\Delta\phi = -\Delta\theta$. According to RTOF, the response of the photons absorbed by the lossy port contributes to a force tangential to the orbit

$$F_t = -\frac{I_{absorb}}{\omega} \cdot \frac{1}{r_{orbit}} \tag{6.1}$$

At this stage, we have a lossy particle inside an isolated cavity and seemingly unidirectional tangential forces along any circular orbit (Eq.6.1). However, given the lossy particle is the only output port of the system, the force on the particle is in principle conservative [43], because

$$\nabla \times \boldsymbol{F} = \nabla \times \left[\frac{I_{absorb}(x,y)}{\omega}\nabla\phi(x,y)\right] = \frac{1}{\omega}[\nabla I_{absorb}(x,y)] \times [\nabla\phi(x,y)] \tag{6.2}$$

$$\nabla I_{absorb}(x,y) = \mathbf{0} \tag{6.3}$$

To reconcile the contradiction with Eq.6.1, we notice that if the lossy particle is the only port, it will absorb 100% of the power and therefore is no longer a perturbation to the cavity. So the phase response of $\Delta\phi = -\Delta\theta$ corresponding to an angular displacement of $\Delta\theta$ would not hold.

To get non-conservative forces, we need at least 2 ports[43]. To introduce the extra port, we side couple the cavity to a line defect waveguide. In this way we can also excite the cavity mode using the waveguide, rather than using a current source inside the cavity. We use rods of radius $r = 0.12a$ outside of the dashed box shown in Fig.6.2 and $r = 0.11a$ inside the dashed box, so that the resonance frequency of the cavity mode is near the center of the 2nd bandgap. The cavity without the particle has a resonance frequency of $f = 0.516c/a$. A lossy dielectric particle placed inside the cavity lowers the resonance frequency by at most 0.08%, depending on where the particle is situated. Without loss of generality, we use the one-way mode similar to Chapter 3.6. With the one-way mode, we only have one port (the transmission) in addition to the lossy port. Notice that if we use two-way modes, we will have two additional ports (the transmission and reflection). As long as the extra ports do not yield opposite contribution to the lossy port, we can still get motoring effect.

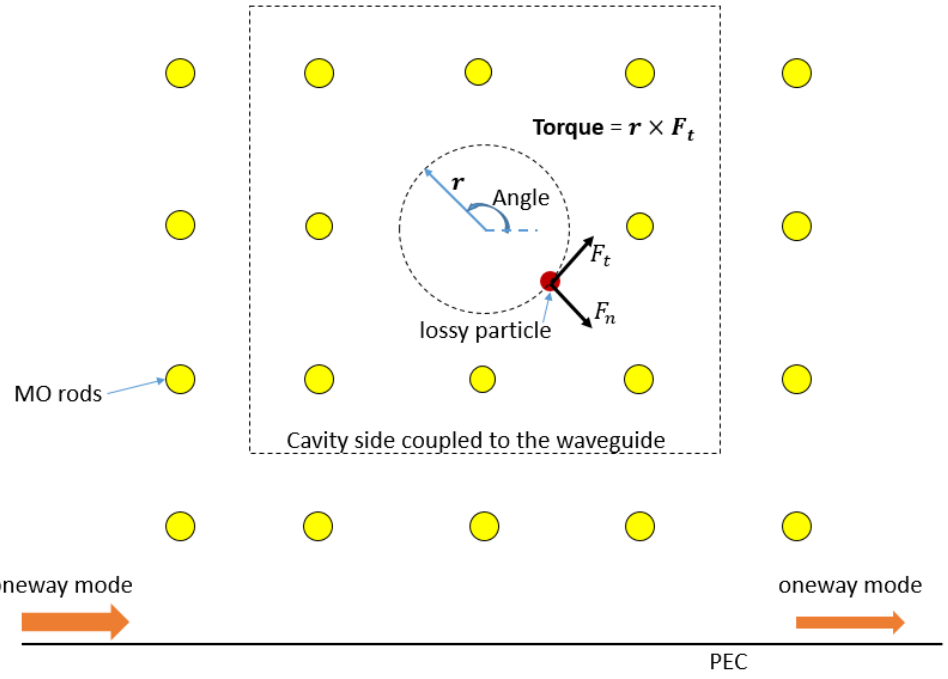

Figure 6.2: Illustration of a point defect cavity side coupled to a one-way waveguide. The magneto optical rods inside the dashed box have radius of $0.11a$, while outside the dashed box have radius of $0.12a$.

We conduct full-wave simulations with the lossy particle placed at different locations, while fixing the amplitude and phase of the incoming light. As the particle travels along an orbit of radius $0.4a$, the amplitude and phase distribution inside the cavity stay largely constant (Fig.6.3). Although a small change can be observed in the phase distribution, the absorbed light on the particle still experiences a full 2π phase shift as the particle completes a circular motion.

Operating with several different frequencies around the resonance, we find the lossy particle experiences a force field with curl (Fig.6.4 upper panel). The torque over the entire space is largely unidirectional (negative). There exist small areas that have positive torque, but as indicated by the force field, the particle will be trapped on orbits that have contiguous negative torque. In contrast, when we use a lossless particle instead, the force

fields become conservative (Fig.6.4 lower panel). Positive torques and negative torques equally divide up the area. This verifies the absorption on the lossy particle is indeed the source of contiguous torque.

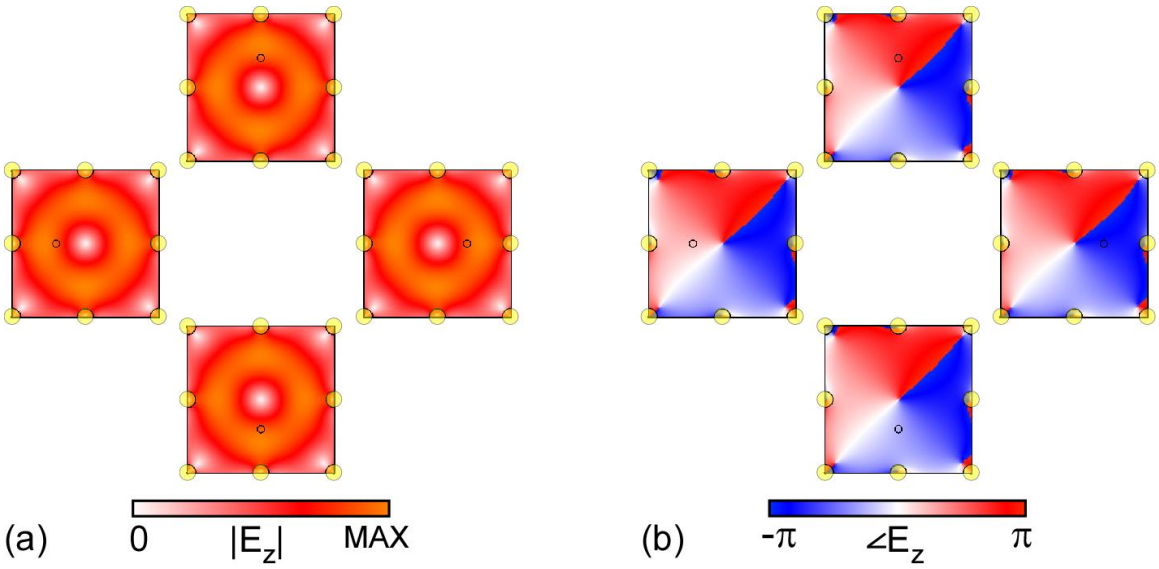

Figure 6.3: The amplitude and phase of E_z field with a lossy particle ($\epsilon_r = 2 + 0.5i$, $r = 0.05a$, black circle) traveling along an orbit of radius $0.4a$, at $f = 0.51586c/a$. (Full-wave study. The cavity mode is excited using the schematics shown in Fig.6.2. The phase of the incident light is fixed.)

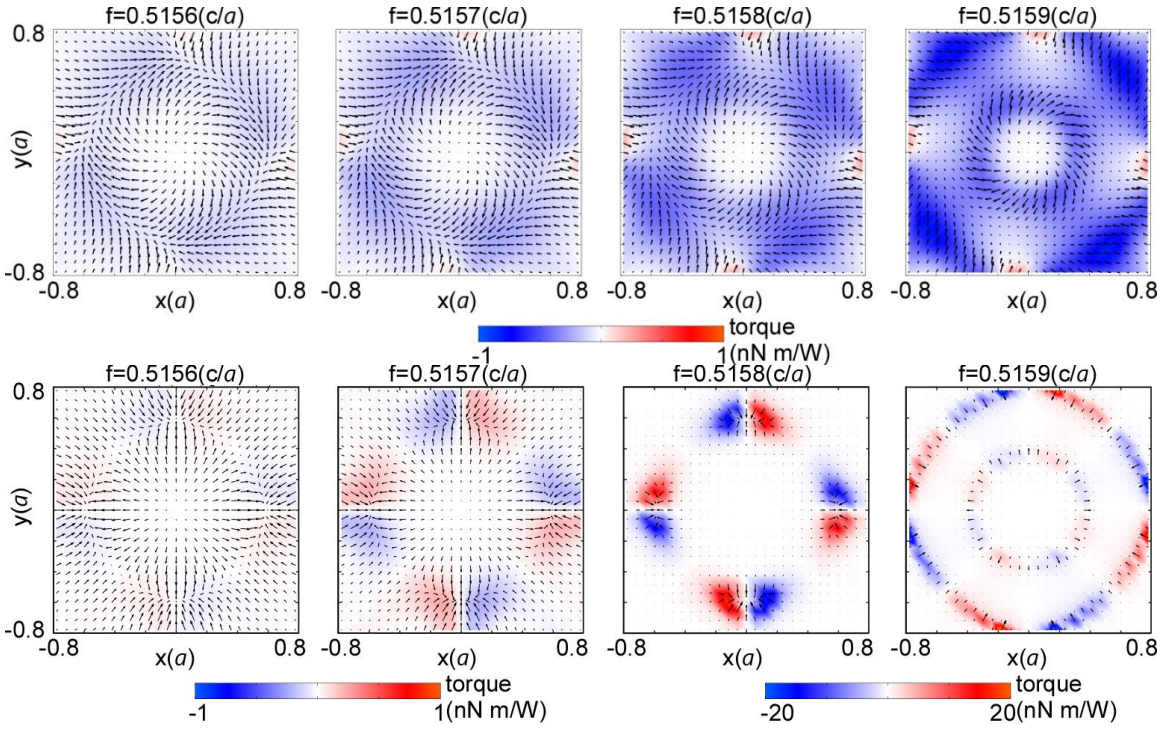

Figure 6.4: Vector force field experienced by a lossy particle ($\epsilon_r = 2 + 0.5i,\ r = 0.05a$, upper panel) and a lossless particle ($\epsilon_r = 2,\ r = 0.05a$, lower panel) placed inside the cavity. The color scale indicates the torque with respect to the center of the cavity.

The vector force field (Fig.6.5a) can be decomposed into normal (Fig.6.5b) and tangential (Fig.6.5b) components. The capability to trap the particle along an orbit is verified by the normal component of forces. At inner loops, the normal force is outwards. While at outer loops, the normal force is inwards. From the normal force, the stable orbit for the particle is estimated to be within the circle of $0.6a$ radius, where the torque and tangential force is always negative (Fig.6.5c).

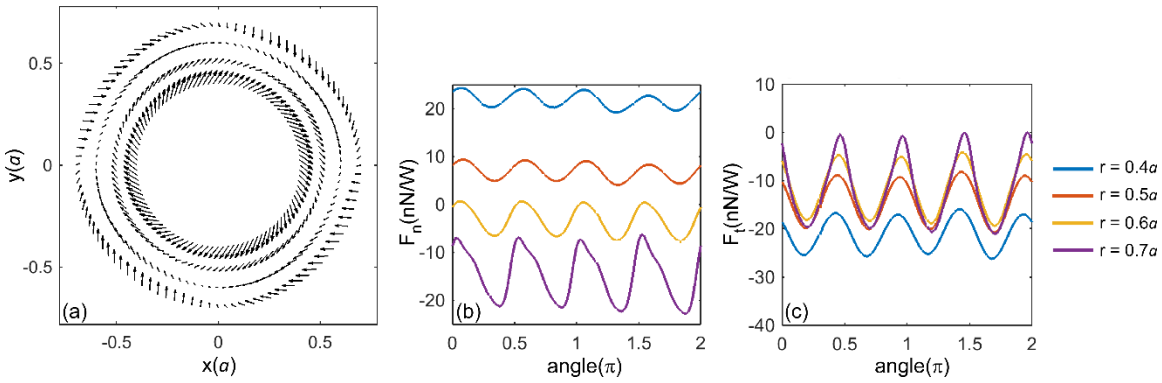

Figure 6.5: Photonic forces on a lossy particle with $\epsilon_r = 2 + 0.5i$ at frequency $f = 0.51586c/a$ The vector force field (a) can be decomposed into (b) normal component F_n and (c) angular component F_t.

RTOF analysis confirmed that the absorption through the lossy port dominates the contribution to the net torque. RTOF expresses the torque as

$$\text{torque} = r_{orbit} \times F_t = \frac{I_{trans}}{\omega}\frac{\partial \phi_{trans}}{\partial \theta} + \frac{I_{absorb}}{\omega}\frac{\partial \phi_{absorb}}{\partial \theta} \tag{6.4}$$

We observe good agreement between RTOF and MST calculated torques (Fig.6.6a). The phase response in the lossy port monotonically decreases, which contributes to net torque. While the power and phase response in the transmission port are symmetric with respect to the mirror plane at $\theta = \pi/2$ and $\theta = 3\pi/2$, which renders zero contribution to the net torque averaged over each circular orbit. Moreover, although the transmission port takes a major amount of power (>65%) (Fig.6.6b,c), the slope in the phase responses of the transmission port is 10x smaller than the slopes in the lossy port.

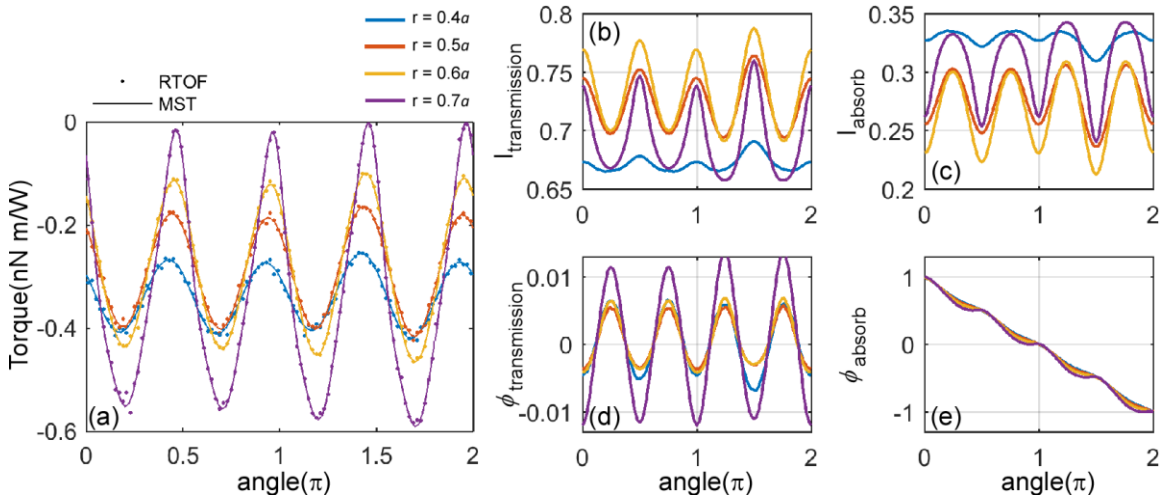

Figure 6.6: RTOF analysis of the torque on a lossy particle with $\epsilon_r = 2 + 0.5i$ at frequency $f = 0.51586c/a$. (a) RTOF agrees with MST calculated torques along orbits of various radius. (b)(c) Power response of the transmission and absorption ports. (d)(e) Phase response of the transmission and absorption ports.

6.3 Upper Limit of the Torque

For a side-coupled cavity, the energy that can be trapped inside the cavity scales up with the quality factor. However, the torque on the lossy particle doesn't scale up with the quality factor. The upper limit for the torque is $\frac{I}{2\omega}$, where I is the input power. The proof is as follows.

The coupled mode equation for the cavity mode side coupled to a one-way waveguide is written as

$$\frac{da}{dt} = (-j\omega_0 - \gamma_e - \gamma_o)a + \kappa S_+ \tag{6.5}$$

$$S_- = d \cdot a + C \cdot S_+ \tag{6.6}$$

where a is the amplitude of the cavity mode, $S_{+/-}$ is the amplitude of input/output one-way mode. κ, d, C are coupling coefficients. γ_o is the intrinsic loss of the cavity, where the loss is due to the lossy particle in our case. γ_e is the external loss of the cavity, where

the loss is due to energy flow from the cavity to the ports. From energy conservation we have

$$d^*d = \kappa^*\kappa = 2\gamma_e \tag{6.7}$$

From Eq.6.5-6.7 we get

$$a = \frac{\sqrt{\gamma_e}}{j(\omega_0 - \omega) + \gamma_e + \gamma_o} S_+$$

$$I_{absorb} = 2\gamma_o|a|^2 = 2\gamma_o \left|\frac{\sqrt{\gamma_e}}{j(\omega_0 - \omega) + \gamma_e + \gamma_o}\right|^2 |S_+|^2 \le 2\gamma_o \left|\frac{\sqrt{\gamma_e}}{\gamma_e + \gamma_o}\right|^2 |S_+|^2$$
$$= \frac{2\gamma_o\gamma_e}{|\gamma_o + \gamma_e|^2}|S_+|^2 \le \frac{1}{2}|S_+|^2 = \frac{1}{2}I$$

For the first inequality, equal sign holds when the cavity is on resonance, i.e. $\omega = \omega_0$. For the second inequality, equal sign holds when critical coupling occurs, i.e. $\gamma_o = \gamma_e$. As the average torque only attributes to the absorption port, and $\frac{\partial \phi_{absorb}}{\partial \theta}$ is on the scale of 1, the torque is largely determined by the absorption power. Therefore, the upper limit of the magnitude of the torque is on the order of $\frac{I}{2\omega}$. For a full circle of motion, the upper limit of the work done on the particle is $\frac{I\pi}{\omega}$.

6.4 Concluding Remarks

In conclusion, we have proposed a photonic motor allowing a lossy particle to conduct cyclic motion around a phase singularity in a photonic crystal defect cavity. The torques around the phase singularity are predicted and verified by RTOF. The force field in the cavity can trap the particle along a circular orbit where the torque is unidirectional. Based on coupled mode theory, the theoretical upper limit of the torque in our system is $I/2\omega$, when the cavity is operating on resonance and at critical coupling. The upper limit of the torque is irrelevant to the quality factor of the cavity, allowing low Q cavity and broad band operation.

Chapter 7: Optomechanics in Graphene Guided-wave System

7.1 Introduction

Graphene is a promising material for optomechanical applications due to its exceptional optical and mechanical properties. Optically, graphene interacts strongly with the light polarized parallel to its surface, leading to strong confinement of light, which is favorable for enhancing optical forces. For example, resonance enhanced optical forces in the THz regime on a suspended graphene under normal incidence of light had been numerically demonstrated[18]. Although graphene is lossy in the plasmonic regime, the loss greatly reduces when operating in the THz regime[35], [36]. Mechanically, graphene has one of the highest stiffness in the in-plane direction, low bending modulus in the out of plane direction and low mass density as a single-layer material[132]. Graphene as a mechanical resonator had been widely studied for potential applications in MEMs and NEMs[132], [133]. Optomechanically, graphene elastic modes interact efficiently with electromagnetic waves. For example, it can couple to microwave cavities[134], undergo laser cooling[135], and be detected by evanescent field[136].

Recent advancement in Radio Frequency (RF) signal processing have witnessed the usage of a strong nonlinear optomechanical interaction, known as Stimulated Brillouin Scattering (SBS), that can coherently transduce[12] and magnify[11] RF signals. Strong SBS interaction requires strong optical forces along guided waves. This had been realized in Silicon step-index waveguides[11]–[13], where the enhancement of optical forces arise from sub-micron confinement of light to the waveguide cross sections [10], [66]. The lateral confinement of light translates to wavelength reduction in the direction of propagation. Graphene guided-wave system exhibits extraordinary wavelength reduction [35], [36], being orders of magnitude stronger than existing guide-wave systems such as hybrid plasmonic waveguide [137] and silicon step-index waveguide[66], which should in

principle lead to strong optical forces along graphene waveguides. Moreover, graphene offers small mass density, large overlap between the optical force field and elastic displacement field, which are all preferred features for strong SBS generation. However, such potential has not yet been investigated.

We study the enhancement of optical forces in graphene guided-wave system and its potential application to SBS generation. Our work[20] numerically demonstrate that quasi-TEM mode confined between parallel graphene sheets provides strong optical forces at terahertz due to orders of magnitude of wavelength reduction. At the same time, an independent work conducted by Lu et.al[138] arrived at similar conclusion about the strong optical forces between parallel graphene nanoribbons. Our work[20] further shows that the optical forces induced by a quasi-TEM mode remain attractive irrespective of the manipulations on the dispersion relations, and irrespective of forward or backward waves. Transmission line model [35] and response theory [42] are applied to provide a profound understanding about the magnitude and direction of forces (Section 7.2). Next, we combine the optical forces and mechanical properties of graphene to estimate the SBS gain in graphene guided-wave system, which turns out to be orders of magnitude stronger than that in a Silicon step-index waveguide (Section 7.3).

Part of this work had been published at the Conference on Lasers and Electro-Optics[20].

7.2 Optical Forces

7.2.1 Enhanced Optical Forces due to Extraordinary Wavelength Reduction

The quasi-TEM mode (Fig.7.1b) between parallel graphene sheets (Fig.7.1a) separated by tens of nanometers has recently been shown to offer orders of magnitude of wavelength reduction [35], [36]. The extraordinary wavelength reduction is induced by the

large kinetic inductance of graphene in the THz regime, which makes graphene an excellent conductor to confine the quasi-TEM mode. The quasi-TEM mode and plasmonic mode are found along the same dispersion relation. While the plasmonic mode resides in the higher frequency range (~100THz) and is lossy because the field is mostly concentrated on the graphene sheets (Fig.7.1c). As a result, graphene optomechanics generally stay away from the plasmonic regime [18].

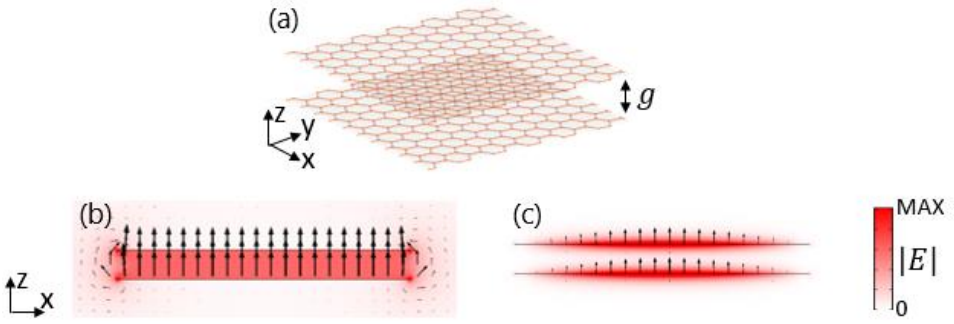

Figure 7.1: (a) Schematic of a parallel graphene sheet waveguide. (b) Cross-sectional electric field distribution of a Quasi-TEM mode at 1THz. (c) Cross-sectional electric field distribution of a plasmonic mode at 100THz. Vectors indicate the electric field components in x-z plane.

Transmission line model provides a profound understanding on the dispersion relations and wavelength reduction of the quasi-TEM mode between parallel graphene sheets[35]. According to transmission line model[114], the propagation constant is expressed as

$$k = \sqrt{(R + j\omega L)(j\omega C)} \tag{7.1}$$

where R, L, C represent the resistance, inductance, and capacitance per unit length respectively. The graphene quasi-TEM mode resides in the LC regime ($\omega L > R$), where the dispersion relation is largely linear. This is corroborated by the slowly changing effective index $n_{eff} = k/k_0$ in the THz range that corresponds to the quasi-TEM mode

(Fig.7.2a). As the capacitance C scales with g^{-1}, we have $n_{eff} \propto g^{-1/2}$, where g is the gap size between the parallel graphene sheets. The effective index n_{eff} represents the factor for wavelength reduction, which achieves 40 at a 30nm gap size. The wavelength reduction becomes even stronger for smaller gap sizes. The scaling power of $-1/2$ remains largely the same for a broad range of frequencies (Fig.7.2b). While for higher frequencies in the 100THz range, the quasi-TEM mode transforms into a plasmonic mode, which renders the transmission line model inapplicable, resulting in nonlinear dispersion relation (Fig.7.2a) and significantly different scaling power between n_{eff} and g (purple line in Fig.7.2b).

Using response theory of optical forces (RTOF) [42], we can predict the scaling and enhancement of lateral optical forces. According to the response theory, the forces (Fig.7.2c) follow the relation

$$F_z = \frac{1}{\omega}\frac{dk}{dg} \tag{7.2}$$

where F_z is the force per unit propagation length, normalized by the guided optical power, ω is the angular frequency, k is the wavenumber. Eq.7.2 can be understood by thinking of the guided mode as a port that allows the photon to leave the system. The phase of the port is determined by $k \cdot L$, where L is the length from the source to the reference plane where we measure the phase. As we enlarge the gap size g, response theory predicts a force of $\frac{I}{\omega}\frac{d(kL)}{dg}$ in the direction of displacement, applied on the segment of waveguide with the length L. After normalizing the forces versus the length and power, we arrive at Eq.7.2. Next, using the relations $k = n_{eff}k_0$ and $n_{eff} \propto g^{-1/2}$ we find $F_z \propto -g^{-3/2}$. The negative sign origins from the negative slope in k versus g, indicating attractive forces. At a 30nm gap size, the magnitude of the force between the graphene sheets is 40 times stronger than the maximum radiation pressure on the surface of a Silicon step-index waveguide[66], for the same guided power.

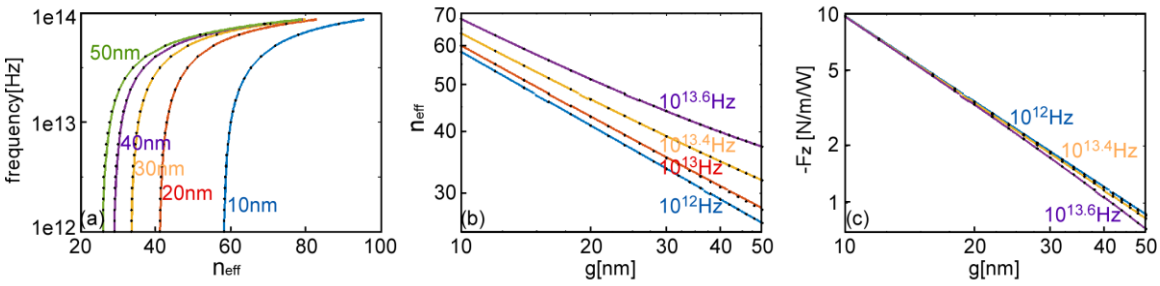

Figure 7.2: (a) Dispersion relation of the quasi-TEM mode for a series of separations g. Dots: from transmission line model; Lines: from first principle simulation (using Drude model for the conductivity of graphene [35]) (b) Relation between the effective index n_{eff} and the separation g for a series of frequencies. (c) Relation between the attractive optical force $-F_z$ and the separation g for a series of frequencies. Dots: from RTOF, Lines: from Maxwell Stress tensor[13]. The graphene sheets have infinite width in x direction.

7.2.2 Direction of Optical Forces under Dispersion Tuning

The strongly confined quasi-TEM mode allows the freedom to create a quasi-2D mode in the 3D structure [35]. Sandwiching a patterned dielectric slab between the graphene sheets, one can obtain a band structure that is identical to the TM modes in a purely 2D system, except for the frequencies are compressed proportional to $\sqrt{g}$ [35] [14]. Can we get strong repulsive forces instead of the attractive forces (see Section 7.2.1), by tuning the dispersion relation of the quasi-TEM mode? It is well-known that the optical forces in conventional waveguide change sign when the guided wave changes from a forward wave ($k \cdot v_g > 0$, v_g: group velocity) to a backward wave ($k \cdot v_g < 0$ [23], [116]). However, our study demonstrates that the optical force induced by the quasi-TEM

[13] Using $\boldsymbol{F} = \int_S \left(\overleftrightarrow{T}_2 - \overleftrightarrow{T}_1\right) \cdot \boldsymbol{n}_{1\to 2}\, ds$

[14] As the gap size g reduces, wavelength reduction enlarges the wavenumber, following $k \propto n_{eff} \propto g^{-1/2}$. To find the original k in the band structure, the corresponding frequency is reduced to $f \propto g^{1/2}$.

mode remains attractive, irrespective of dispersion tuning, and irrespective of forward or backward waves.

First we demonstrate attractive forces from a quasi-TEM mode which is engineered into a backward wave. A photonic crystal supporting backward wave is sandwiched between the graphene sheets (Fig.7.3a,b). The backward wave exists along the $\Gamma - M$ direction of the 2nd bulk band (Fig.7.3c) for $k_x, k_y \in (0.3, 0.38)2\pi/a$ [23]. We calculate the forces from first principle simulation and find attractive forces (Fig.7.3d) for the entire 2nd bulk band along the $\Gamma - M$ direction.

Now we explain the reason for universal attractive forces associated with the quasi-TEM mode. From RTOF[42]: the direction of forces follow the sign of dk/dg. Although the periodicity complicates the identification of the wavenumber k in the periodic Brillouin zone, the relation $f \propto \sqrt{g}$ simplifies the picture: For a fixed k, the eigen frequency increases as g increase (Fig.7.3c,e). So for a fixed frequency, a mode with positive group velocity always experiences a left-shift in k following the red arrows in Fig.7.3e, no matter whether the mode is forward-wave or backward-wave. The rule to use RTOF here is we need to always use the segments with positive group velocity, because the forces perpendicular to the graphene do not distinguish between a pair of opposite waves that are parallel to the graphene. Therefore, $dk/dg < 0$ and attractive forces are always the case for quasi-TEM modes, irrespective of dispersion tuning.

For the hybrid photonic crystal structure, the force from response theory is a total force on the hybrid interface including both the dielectric interface and the graphene. The hybrid interface is stable due to strong van der Waals force. For application as body force, one can fill the space between graphene with dielectric, meanwhile using photonic crystal to fine tune the dispersion relation. For application of forces on suspended graphene, one

can introduce an air defect in the photonic crystal slab[35], so that the optical force will be confined to the defect region.

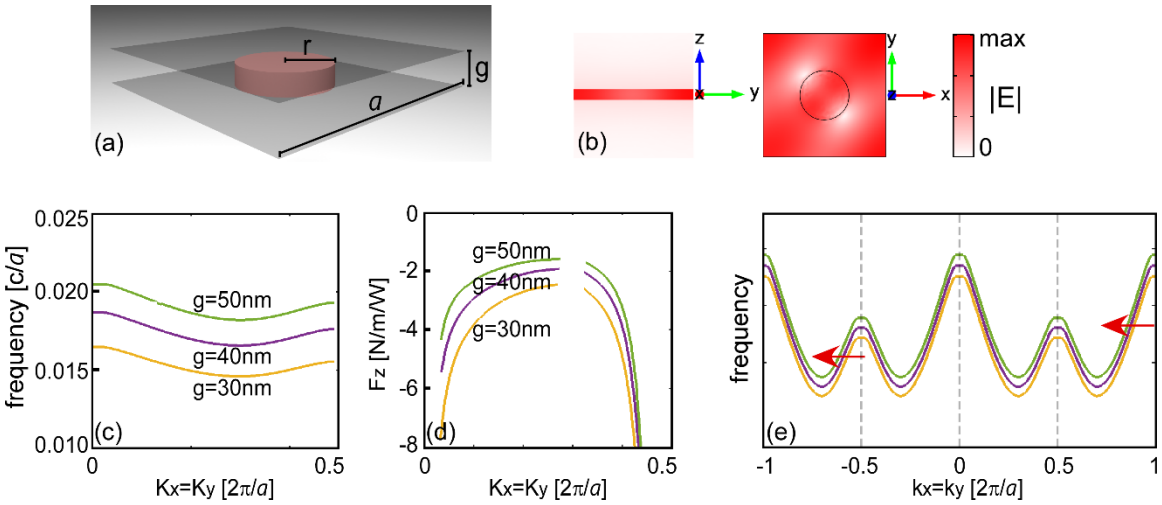

Figure 7.3: (a) Schematic of a unit cell of two single-layer graphene sheets sandwiching a square lattice ($a = 450nm$) of dielectric rods ($\epsilon_r = 9,\ r = 0.2a$). (b) Side and top view of the field distribution for a quasi-TEM mode. (c) Dispersion relation of the 2nd bulk band along $\Gamma - M$ direction, for different g. (d) Attractive forces for bands in (b). (d) Schematic of how the dispersion relation shift as g increase.

7.3 Stimulated Brillouin Scattering using Graphene Waveguide

In this section we estimate the SBS gain in the Graphene waveguide and compare it with the SBS gain in a Silicon step-index waveguide[12], [139].

In a typical SBS process, the pump wave $\boldsymbol{E}_p = e^{ik_p x - i\omega_p t}$ and Stokes wave $\boldsymbol{E}_s = e^{ik_s x - i\omega_s t}$ generate an optical force field that have the phase-matched wavenumber $q = k_p - k_s$ at the beating frequency $\Omega = \omega_p - \omega_s \ll \omega_{p,s}$. Mechanical vibrations driven by the optical forces enable parametric conversion between the pump and Stokes waves, following the relation [140]

$$\frac{dP_s}{dx} = gP_pP_s - \alpha_sP_s \tag{7.3}$$

where $P_p = v_g\langle \boldsymbol{E}_p, \epsilon \boldsymbol{E}_p\rangle/2$, $P_s = v_g\langle \boldsymbol{E}_s, \epsilon \boldsymbol{E}_s\rangle/2$ are the powers of the pump and Stokes waves, g is the SBS gain, α_s is the optical damping coefficient. The SBS gain of a single elastic mode is expressed as [139]

$$g_m(\Omega) = G_m \frac{(\Gamma_m/2)^2}{(\Omega-\Omega_m)^2+(\Gamma_m/2)^2} \tag{7.4}$$

$$G_m = \frac{\omega \cdot Q_m}{\Omega_m^2 2 P_p P_s} \cdot \frac{|\langle \boldsymbol{f}_m, \boldsymbol{u}_m\rangle|^2}{\langle \boldsymbol{u}_m, \rho \boldsymbol{u}_m\rangle} \tag{7.5}$$

where Ω_m is the eigen frequency of the mechanical mode, Γ_m is the elastic loss, $Q_m = \Omega_m/\Gamma_m$ is the quality factor of the mechanical vibration, ω is the optical frequency, $\boldsymbol{f}_m$ is the force density, $\boldsymbol{u}_m$ is the displacement field of the eigen elastic mode, ρ is the mass density. The SBS gain g_m takes the maximum value G_m when operating under phase matching and frequency matching condition.

To facilitate RF signal processing, the mechanical frequency Ω_m is usually chosen in the GHz range which matches with the RF signal. While other parameters can differ across systems. In order to enlarge the SBS gain, it is beneficial to have (1) high optical frequency ω; (2) high mechanical quality factor Q_m; (3) large forces under a given power $\frac{f_m}{P_{p,s}}$; (4) large overlap between the force field and the elastic mode $\langle \boldsymbol{f}_m, \boldsymbol{u}_m\rangle$; and (5) small mass density ρ. In the following we will see: although the graphene optomechanical system has smaller values in (1)&(2) compared to a Silicon step-index waveguide, it brings greater enhancements in (3)(4)(5) and overall a larger G_m.

To support mechanical mode, the parallel graphene sheets are doubly clamped to a pair of slabs (Fig.7.4a), leaving a suspended region of width d that can deflect and vibrate under optical forces. The clamping also allows pre-strain in the x direction, to achieve the desired mechanical frequency Ω_m. The mechanical eigen mode can be described as

$$\boldsymbol{u}_m = \big(0,0,w(x,y,t)\big) \tag{7.6}$$

which is governed by [141]

$$\ddot{w} + c\dot{w} - \rho^{-1}\left\{\frac{\partial}{\partial x}\left[\frac{\partial w}{\partial x}T_x\right] + \frac{\partial}{\partial y}\left[\frac{\partial w}{\partial y}T_y\right]\right\} = 0 \tag{7.7}$$

$$T_x = (\lambda + 2\mu)\delta_x + \lambda\delta_y + \left(\frac{\lambda}{2} + \mu\right)\left[\left(\frac{\partial w}{\partial x}\right)^2 + \left(\frac{\partial w}{\partial y}\right)^2\right] \quad (7.8)$$

$$T_y = (\lambda + 2\mu)\delta_y + \lambda\delta_x + \left(\frac{\lambda}{2} + \mu\right)\left[\left(\frac{\partial w}{\partial x}\right)^2 + \left(\frac{\partial w}{\partial y}\right)^2\right] \quad (7.9)$$

where $w(x, y, t)$ is the deflection in the z direction, c the damping coefficient, T_x and T_y are tensions in the x and y direction induced by the stretching of graphene, λ and μ are Lame parameters, δ_x and δ_y are constants representing the pre-strains in the x and y directions. Here we have $\delta_x \neq 0$ and $\delta_y = 0$. Under small deflections, the nonlinear terms can be ignored[132], [141], Eq.7.7-7.9 reduce to

$$\ddot{w} + c\dot{w} - \rho^{-1}\left\{(\lambda + 2\mu)\delta_x \frac{\partial^2 w}{\partial x^2} + \lambda\delta_x \frac{\partial^2 w}{\partial y^2}\right\} = 0 \quad (7.10)$$

The mechanical mode on graphene follows the form of

$$w(x, y, t) = w(t)\cos\frac{\pi x}{d} e^{i\cdot q\cdot y} \quad (7.11)$$

with an eigen frequency

$$\Omega_m = \frac{\pi}{d}\sqrt{\frac{\delta_x}{\rho}\left[\lambda\left(1 + \left(\frac{q}{\pi/d}\right)^2\right) + 2\mu\right]} \quad (7.12)$$

Experimental works [132] have reported the mechanical quality factor Q_m=300 for doubly clamped graphene strips at room temperature, where the mechanical damping is dominated by thermoelectric dissipation. At low temperatures (<100mK), the quality factor can increase to 10^5, where the mechanical damping is dominated by clamping loss. Nevertheless, even at room temperature, the damping coefficient c is much smaller than Ω_m and can be ignored to arrive at Eq.7.12.

For the quasi-TEM mode, the ratio between the optical forces and the guided power per unit width is invariant to the width (Fig.7.2). Exposing the clamped part of graphene to light causes inefficient usage of optical power because the clamped part cannot vibrate as the aforementioned elastic mode even though they also experience optical forces. So we use 1D photonic crystals instead of uniform slabs on the sides to concentrate the optical power to the suspended region. (Fig.7.4b). The 1D photonic crystals also help to shape the

y-directional forces into a lateral dependence that roughly follows $\cos\frac{\pi x}{d}$ (Fig.7.4c), which largely overlaps with the displacement field.

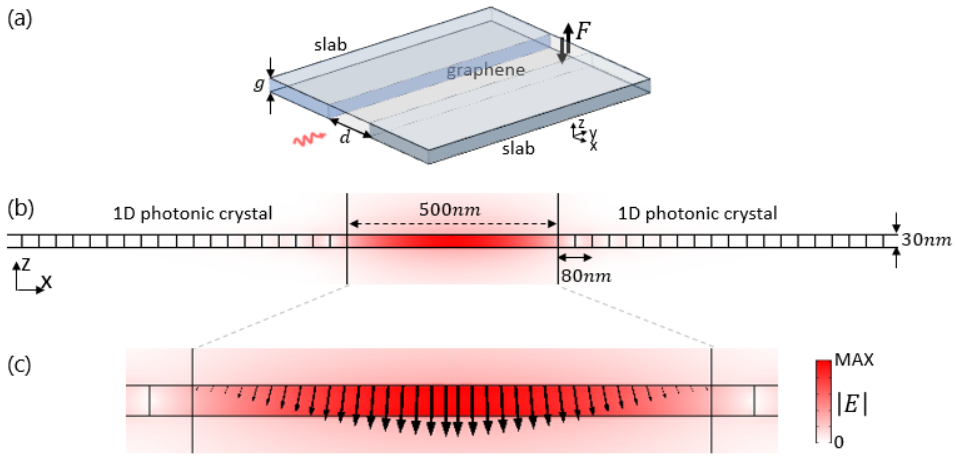

Figure 7.4: (a) Schematic of doubly clamped parallel graphene sheets for SBS generation. (b) Distribution of electric field in the cross section at f=20THz. The slabs on the sides are patterned into 1D photonic crystals to provide lateral confinement and shape the force field. The 1D PhC consists of half low index material ($\epsilon_r = 2.25$) and half high index material ($\epsilon_r = 11.67$). The periodicity of the 1D PhC is 80nm. (c) Vector indicates the forces on the top layer graphene. The bottom layer graphene experiences opposite z-directional forces, which is not shown here.

Let's consider the optical modes (pump and Stokes) operating at frequencies $f_p \approx f_s = 20THz$, to interact with a mechanical mode at frequency $f_m = f_p - f_s = 2.5GHz$. The gap size between the graphene sheets is chosen to be $g = 30nm$. The width of suspended graphene is chosen to be $d = 500nm$. The optical frequency and gap size determines the effective index to be $n_{eff} = 37.85$ (Fig. 7.2a), which stays relatively a constant for a bandwidth of a few GHz. The phase-matching wavenumber for the mechanical mode in the propagation direction is $q = k_p - k_s = \frac{2\pi(f_p - f_s)}{c} \cdot n_{eff} = 1983m^{-1}$. Notice that q is orders of magnitude smaller than the lateral wavenumber $\frac{\pi}{d} = 6.283 \times 10^6 m^{-1}$. Therefore Eq.7.12 reduces to

$$\Omega_m = \frac{\pi}{d}\sqrt{\frac{\delta_x}{\rho}(\lambda + 2\mu)} \tag{7.13}$$

Given the Lame parameters $\lambda + 2\mu = 340J/m^2$ and mass density $\rho = 7.6 \times 10^{-7} kg \cdot m^{-2}$ [141], the required pre-strain δ_x is 1.4%, which is achievable in many experiments [133]. Notice that for a fixed mechanical frequency Ω_m, δ_x is proportional to d^2. Therefore having a small width d is beneficial for controlling the required pre-strain at a low level.

Using the parameters discussed above, the SBS gain in the setup shown in Fig.7.4 is calculated to be $G_m = 4.02 \times 10^8 m^{-1}W^{-1}$. This is over 10^4 times stronger than the maximum value in a Silicon step index waveguide. Large SBS gain translates to smaller pump power and shorter interaction length, to achieve the same level of parametric conversion.

Here's a break-down comparison to illustrate why the SBS Gain in graphene waveguide is greater than that that in a silicon step-index waveguide. For the Graphene waveguide considered above, we have

$$\frac{\omega \cdot Q_m}{2\Omega_{\mathrm{m}}^2} = \frac{[2\pi \cdot 20THz] \cdot [300]}{2[2\pi \cdot 2.5GHz]^2} \tag{7.14}$$

$$\frac{|\langle \boldsymbol{f}_m, \boldsymbol{u}_m \rangle|^2}{P_p P_s \langle \boldsymbol{u}_m, \rho \boldsymbol{u}_m \rangle} = {}^{15}\frac{\langle \boldsymbol{f}_m, \boldsymbol{f}_m \rangle}{P_p P_s \rho} = \frac{\int_{-\frac{d}{2}}^{\frac{d}{2}} \left(2[N \cdot m^{-2}] \cdot \cos\frac{\pi x}{d}\right)^2 dx}{(1[W \cdot m^{-1}] \cdot d)^2 \cdot \rho} = \frac{2[N \cdot W^{-1}m^{-1}]^2}{d \cdot \rho} \tag{7.15}$$

The surface pressure of $2N \cdot m^{-2}$ on graphene for $1W \cdot m^{-1}$ power per unit width can be found from Fig.7.2c, at 30nm gap size. For a Silicon step-index waveguide with the cross section $a_1 \times a_2$ and mass density $\rho_{Si} = 2329kg \cdot m^{-3}$:

$$\frac{\omega \cdot Q_m}{2\Omega_{\mathrm{m}}^2} = \frac{[2\pi \cdot 200THz] \cdot [1500]}{2[2\pi \cdot 2.5GHz]^2} \tag{7.16}$$

The optical forces include the surface radiation pressure and the electrostrictive body force. Let's first estimate the contribution from the surface radiation pressure:

---

[15] Using the fact that $f_{m,z} \propto \cos\frac{\pi}{d}x \cdot e^{iqy}$, $\boldsymbol{u_m} = \left[0,0,\cos\frac{\pi}{d}x \cdot e^{iqy}\right]$ and integrating only along the graphene (x-direction).

$$\frac{|\langle \boldsymbol{f}_m, \boldsymbol{u}_m \rangle|^2}{P_p P_s \langle \boldsymbol{u}_m, \rho_{Si} \boldsymbol{u}_m \rangle} = \frac{\langle \boldsymbol{f}_m, \boldsymbol{f}_m \rangle}{P_p P_s \rho_{Si}} C = \frac{\int_{-a_1/2}^{a_1/2} dx \int_{-a_2/2}^{a_2/2} dy \frac{10^5[N \cdot m^{-2}] 10^5[N \cdot m^{-2}]}{a_1 \quad a_2}}{[W]^2 \cdot \rho_{Si}} C = \frac{\left(10^5[N \cdot m^{-2}]\right)^2}{[W]^2 \cdot \rho_{Si}} C \quad (7.17)$$

Where the factor C accounts for the mismatch between the force field f_m and displacement field u_m in the silicon waveguide, typically taking the value of 0.1. In Eq.7.17, we have used the maximum surface radiation pressure on a silicon step-index waveguide, which was reported to be $10^5 N \cdot m^{-2}$ for $1W$ of guided power, after scanning over the cross-sectional side length [66]. We also used a trick to remove the dimensional dependence in the Silicon waveguide for the purpose of comparison, by distributing the surface pressure over the bulk to arrive at a force density $\frac{10^5[N \cdot m^{-2}]}{a_{1,2}}$. Finally, we find the value of Eq.7.14 is 50 times smaller than that of Eq.7.16, while the value of Eq.7.15 is 1.2×10^7 times greater than that of Eq.7.17, which indicates the SBS Gain in the graphene waveguide is 2.4×10^5 times stronger than the surface radiation pressure induced SBS Gain in the Silicon step-index waveguide. Combing the contribution from electrostrictive force in Silicon step-index waveguide, one can boost the SBS Gain by a factor of 10 [139]. Overall, the SBS Gain in the graphene waveguide is still over 10^4 times stronger than that in a Silicon step-index waveguide.

7.4 CONCLUDING REMARKS

In conclusion, we have demonstrated strong optical forces between parallel graphene sheets at terahertz due to extraordinary wavelength reduction of the guided quasi-TEM mode, as well as its potential to generate strong SBS interaction. The wavelength reduction factor as well as the forces scale up as the gap size between the graphene sheets reduces. At a 30nm gap size, the forces are 40 times stronger than the maximum value achieved in a silicon step-index waveguide[66]. The force induced by a quasi-TEM mode remains attractive, irrespective of dispersion tuning, and irrespective of forward or backward waves. Combining the strong optical forces and the exceptional mechanical

property of graphene, a doubly clamped graphene waveguide can support an SBS gain of 4e8/W/m, which is 4 orders of magnitude stronger than in a Silicon step-index waveguide[10].

Chapter 8: Topology Optimization for Dispersion Engineering

8.1 Introduction

Topology optimization is a powerful technique for structural design in photonics [15], [16], [67], [68], [70], [139], [142]–[145] and mechanics [69]. It optimizes the material layout in a given design space, to improve the performance of the system. The design can attain any shape, which fully exploits the degrees of freedom available in a limited space. In topology optimization, the space is discretized into finite elements, where the material properties on each element are treated as design parameters. With recent advancements in computational power, topology optimization can handle millions of design parameters and a fine discretization[15].

In photonics, topology optimization can be applied for a broad range of purposes, such as to enlarge a complete band-gap[70], to tailor a slow light [67], [68], to design a broadband mode converter [16], [143], [144], to enhance the resonance in a cavity [142], to enhance nonlinear interactions [15], [145], etc. Suitable mathematical formulations are chosen based on the design target. For example, to maximize a complete bandgap, people have developed semidefinite program[70]. To tailor the scattering coefficients over a spectrum, or the quality factor of resonators, or the strength of nonlinear interaction, it is usually formatted as maximizing/minimizing the overlap integral between the driven fields and a specified field profile, or between multiple driven fields [15], [16], [142]–[145]. To tune the dispersion relations for a specific mode, one may locally perturb the structure to modify the Eigen frequencies [68], [146]. The gradients of the target function versus the element-wise material properties can be constructed through finite difference[15] or finite element [70] methods.

In this Chapter we apply topology optimization to one of our systems, to replace human effort with computational power, for future convenience in the optomechanics

structural design process. Based on our specific problem, we formulate the proper target functions and constraints, choose a suitable discretization approach and construct the gradients of the target and constraints versus the design parameters. Then using the globally-convergent method-of-moving-asymptotes (MMA) algorithm[147], we perform the optimization to tune the shape of the dielectric structures towards the design target.

8.1.1 Description of the Dispersion Engineering Problem

Recall that in Chapter 4.2, we encountered a dispersion engineering problem. We were searching for a single-mode backward-wave to realize long range and robust optical pulling forces in an all Silicon photonic crystal waveguide (Fig.8.1a). We have found a defect waveguide mode which is a backward-wave whose group velocity is opposite to its wavenumber ($|k_x| < 0.35 \cdot 2\pi/a$ on the blue curve in Fig.8.1b). However, the dispersion relation (blue curve in Fig.8.1b) begins to have a positive slope for $|k_x| > 0.35 \cdot 2\pi/a$, which becomes a forward-wave and coexists with the backward-wave at the same frequency. Single mode operation is desirable for experiments because it drastically simplifies the light source used to excite the backward-wave mode, and avoids mode mixing due to scattering. On the dispersion curve of the Bloch mode that we use, single mode means we can have only a single k value in the range of $(0,\pi/a)$ at a given frequency, which is not the case for the curve shown in Fig.8.1b. In Chapter 4.2, we hand-tuned the structure to bring down the frequency of the defect waveguide mode for $|k_x| > 0.35 \cdot 2\pi/a$, without deforming the rest of the band structure. Here instead of hand-tuning, we apply gradient based topology optimization for the same purpose. We format the optimization problem as follows:

Minimize:

$$f = \max_{k\in[0.35\cdot\frac{2\pi}{a},0.5\cdot\frac{2\pi}{a}]} \omega_{wg,k} \tag{8.1}$$

With constraints:

$$g_1 = \frac{\omega_{wg,k=0.2}^{initial}}{1+\varepsilon_1} - \omega_{wg,k=0.2} < 0 \tag{8.2}$$

$$g_2 = \frac{\omega_{up,k=0.45}^{initial}}{1+\varepsilon_2} - \omega_{up,k=0.45} < 0 \tag{8.3}$$

$$\epsilon_r^{\mathbb{D}} \in [\epsilon_r^{air}, \epsilon_r^{silicon}]$$

where $\omega = 2\pi f$, ω_{wg} is the angular frequency of the waveguide mode, ω_{up} is the angular frequency of the upper bulk mode, $0 < \varepsilon_{1,2} \ll 1$ is a slack variable that allows the frequency of each mode to be lowered for a limited percentage during optimization. $\epsilon_r^{\mathbb{D}}$ is the relative permittivity in the design region. During optimization iterations we allow $\epsilon_r^{\mathbb{D}}$ to take continuous values between $\epsilon_r^{air} = 1$ and $\epsilon_r^{silicon} = 12.25$. In the end we apply level set method[148] to convert $\epsilon_r^{\mathbb{D}}$ into binary values.

Thanks to the periodicity, we only need to compute the eigenvalue problem for a unit cell. The unit cell is chosen to have 7 rods on both sides of the line defect (total size $1a \times 14.5a$). Periodic boundary condition is applied. To prevent the band structure and mode profile from changing drastically, and to prevent the added dielectrics from blocking the path for the particles in the center of the waveguide, we limit the design region to the orange shaded rectangular areas in Fig.8.1a. Notice that the design regions are periodically repeated along the x-axis. In the design regions, we can modify the dielectric properties of each mesh element. While outside of the design regions, the structure is fixed.

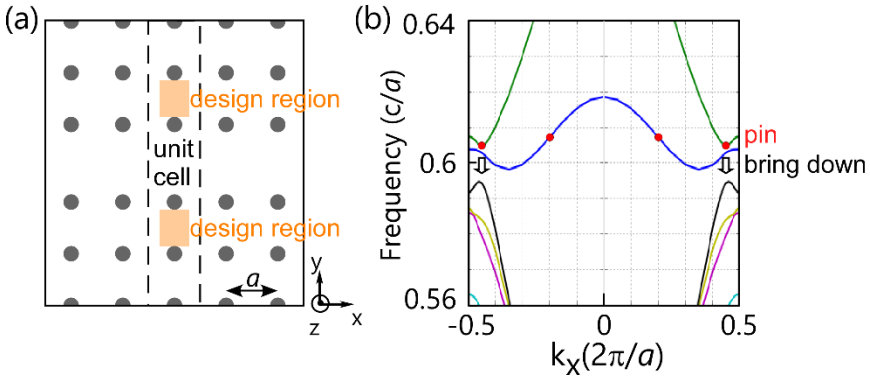

Figure 8.1: The dispersion engineering problem towards single mode operation. (a) Schematic of the waveguide: line defect with a width $d = 1.5a$ along the Γ-X direction in a 2D square lattice photonic crystal of silicon rods ($r = 0.15a$, $\epsilon_r = 12.25$). The design regions are repeated along the x-axis, for every lattice constant a. (b) Dispersion relation (TM-polarization) of the waveguide mode (blue) and bulk modes (other colors). The target of the dispersion engineering is to reduce the frequency of the waveguide mode for $k_x \in [0.35,0.5]\frac{2\pi}{a}$ as indicated by the black arrows. While enforcing constraints to limit the reduction in the frequencies denoted by the red dots. The calculated Eigen frequencies are slightly higher than that shown in Chapter 4.2 due to the lower finite element resolution being used here[73].

8.2 Implementation

Finite element method is employed to construct a linear algebra representation of the physics problem, from which we can extract the gradients of the Eigen frequencies versus the dielectric properties of each mesh element in the design region. The gradient based dispersion engineering turns out to be equivalent to a sequence of Eigen value perturbation. At each iteration, gradients are computed; updates are applied to the dielectric properties; and the Eigen value problem is recalculated. As the iteration goes on, the dispersion relations are tuned towards the design target.

8.2.1 Finite Element Formulation

As we have mentioned in Chapter2.1.1, the Eigen value study used to calculate the photonic crystal band structure is based on the Master's equation of electromagnetic fields.

$$\nabla \times \left(\frac{1}{\mu}\nabla \times \boldsymbol{E}(\boldsymbol{x})\right) - \omega^2 \overleftrightarrow{\epsilon}(\boldsymbol{x})\boldsymbol{E}(\boldsymbol{x}) = 0 \tag{8.4}$$

where $\boldsymbol{E}$ is the electric field; $\boldsymbol{x} \in \mathbb{R}^2$, $\mathbb{R}^2$ represents the coordinates in the unit cell; μ is the permeability, equaling to the vacuum permeability μ_0; $\overleftrightarrow{\epsilon}$ is the permittivity, which is to be tuned through optimization; ω is the angular frequency. As the mode of interest takes TM polarization, we can simply use E to denote the out-of-plane electric field, Eq.8.4 becomes

$$-\nabla \cdot \left(\nabla E(\boldsymbol{x})\right) - \left(\frac{\omega}{c}\right)^2 \epsilon_r(\boldsymbol{x})E(\boldsymbol{x}) = 0 \tag{8.5}$$

For Bloch modes

$$E(\boldsymbol{x}) = u_k(\boldsymbol{x}) \cdot e^{i\boldsymbol{k}\cdot\boldsymbol{x}} \tag{8.6}$$

where u_k is the unit cell function, $\boldsymbol{k}$ is the Bloch k, taking real values for lossless system.

Finite element method converts the original PDE (Eq.8.5) into a weak form

$$-\int_{\mathbb{R}^2} \tilde{E}(\boldsymbol{x})\left[\nabla \cdot \left(\nabla E(\boldsymbol{x})\right) - \left(\frac{\omega}{c}\right)^2 \epsilon_r(\boldsymbol{x})E(\boldsymbol{x})\right] d\Omega = 0 \tag{8.7}$$

where $\tilde{E}$ is the test function for E. The test function is free to take any value. Without loss of generality, we can use

$$\tilde{E}(\boldsymbol{x}) = \tilde{u}_k(\boldsymbol{x}) \cdot e^{-i\boldsymbol{k}\cdot\boldsymbol{x}} \tag{8.8}$$

Combining Eq.8.6-8.8 and using integration by parts we get

$$\begin{aligned}\int_{\mathbb{R}^2} \nabla\left[\tilde{u}_k\, e^{-i\boldsymbol{k}\cdot\boldsymbol{x}}\right] \cdot \nabla\left[u_k\, e^{i\boldsymbol{k}\cdot\boldsymbol{x}}\right] d\Omega - \int_{\partial\mathbb{R}^2} \tilde{u}_k\, e^{-i\boldsymbol{k}\cdot\boldsymbol{x}} \nabla\left[u_k\, e^{i\boldsymbol{k}\cdot\boldsymbol{x}}\right] ds \\ = \int_{\mathbb{R}^2} \left(\frac{\omega}{c}\right)^2 \epsilon_r(\boldsymbol{r})\ \tilde{u}_k\, u_k\ d\Omega\end{aligned} \tag{8.9}$$

The boundaries between unit cells get contributions from the boundary terms in Eq.8.9 from both the neighboring unit cells, which cancel out given that there is no electric current on the boundary. So we only need to deal with the domain terms:

$$\begin{aligned}\int_{\mathbb{R}^2} \nabla\tilde{u}_k \cdot \nabla u_k d\Omega - i\boldsymbol{k} \cdot \int_{\mathbb{R}^2} [\tilde{u}_k \nabla u_k - u_k \nabla\tilde{u}_k] d\Omega + \int_{\mathbb{R}^2} \boldsymbol{k} \cdot \boldsymbol{k}\, \tilde{u}_k\, u_k d\Omega \\ = \int_{\mathbb{R}^2} \left(\frac{\omega}{c}\right)^2 \epsilon_r(\boldsymbol{x})\tilde{u}_k\, u_k d\Omega\end{aligned} \tag{8.10}$$

For discretization, because the unit cell is rectangular and can be divided uniformly into squares, we use square shaped elements. For areas outside of the design region, we use quad-tree mesh [70] to reduce the computational cost. The quad-tree mesh element recursively refines itself if it is crossing a dielectric boundary, until the minimum size is reached (Fig.8.2). For regions far from the dielectric boundaries, the mesh elements take larger sizes, reducing the number of degrees of freedom efficiently. A 2:1 rule is enforced to ensure gradual transition in the mesh size. Inside the design region, all the elements take the minimum size, which allows full potential of the element-wise design.

After discretization, we need to approximate the unknown functions $u_k(\boldsymbol{x})$ within each element. With finite element method, each square shaped elements are mapped to a local coordinate (ξ, η) as shown in Fig.8.2. Functions inside the element are interpolated from the values of the approximated $u_k(\boldsymbol{x})$ on its four vortices. We use first order shape function, because for a given computational power, we prefer to divide the elements in the design region as fine as possible, so that the dielectric properties are specified to the finest resolution. The first order shape functions include four independent functions, each taking value 1 on one of the vortices and 0 on other vortices.

$$\phi_1^e = (1-\xi)(1-\eta)/4$$
$$\phi_2^e = (1+\xi)(1-\eta)/4$$
$$\phi_3^e = (1+\xi)(1+\eta)/4$$
$$\phi_4^e = (1-\xi)(1+\eta)/4$$

Values interpolated in the area of the element take the linear combination of the four shape functions, while the coefficients are the values of the approximated $u_k(\boldsymbol{x})$ on the four vortices.

$$\varphi_k^e = [\phi_1^e\ \phi_2^e\ \phi_3^e\ \phi_4^e]\begin{bmatrix} v_{1,k}^e \\ v_{2,k}^e \\ v_{3,k}^e \\ v_{4,k}^e \end{bmatrix}$$

Mapped onto each element, Eq.8.10 is rewritten into a linear algebra, leaving the values on the vortices as unknown coefficients to be solved.

$$\int_{\mathrm{e}} \nabla\tilde{\varphi}_k^e \cdot \nabla\varphi_k^e d\Omega = \tilde{\boldsymbol{v}}_k^{(e)^T} K^{(e)} \boldsymbol{v}_k^{(e)}$$

$$K_{ij}^{(e)} = \int_e \nabla\tilde{\phi}_i^e \cdot \nabla\phi_j^e\, d\Omega = \int_{\mathrm{e}} \left(\frac{\partial\tilde{\phi}_i^e}{\partial x}\frac{\partial\phi_j^e}{\partial x} + \frac{\partial\tilde{\phi}_i^e}{\partial y}\frac{\partial\phi_j^e}{\partial y}\right)\frac{dx}{d\xi}d\xi\frac{dy}{d\eta}d\eta$$

$$= \int_{\mathrm{e}} \left(\frac{\partial\tilde{\phi}_i^e}{\partial\xi}\frac{\partial\phi_j^e}{\partial\xi} + \frac{\partial\tilde{\phi}_i^e}{\partial\eta}\frac{\partial\phi_j^e}{\partial\eta}\right)d\xi d\eta$$

$$\frac{dx}{d\xi} = \frac{dy}{d\eta} = \frac{h}{2}$$

$$-i\boldsymbol{k}\cdot\int_e [\tilde{\varphi}_k^e\nabla\varphi_k^e - \varphi_k^e\nabla\tilde{\varphi}_k^e]d\Omega = \tilde{\boldsymbol{v}}_k^{(e)^T}\left[-ik_x C_x^{(e)} - ik_y C_y^{(e)}\right]\boldsymbol{v}_k^{(e)}$$

$$C_{x,ij}^{(e)} = \frac{h}{2}\int_e \left(\tilde{\phi}_i^e\frac{\partial\phi_j^e}{\partial\xi} - \phi_j^e\frac{\partial\tilde{\phi}_i^e}{\partial\xi}\right)d\xi d\eta$$

$$C_{y,ij}^{(e)} = \frac{h}{2}\int_e \left(\tilde{\phi}_i^e\frac{\partial\phi_j^e}{\partial\eta} - \phi_j^e\frac{\partial\tilde{\phi}_i^e}{\partial\eta}\right)d\xi d\eta$$

$$\int_e \boldsymbol{k}\cdot\boldsymbol{k}\,\tilde{\varphi}_k^e\,\varphi_k^e d\Omega = \tilde{\boldsymbol{v}}_k^{(e)^T}|\boldsymbol{k}|^2 M^{(e)}\boldsymbol{v}_k^{(e)}$$

$$M_{ij}^{(e)} = \left(\frac{h}{2}\right)^2\int_e \tilde{\phi}_i^e\phi_j^e\, d\xi d\eta$$

$$\int_e \left(\frac{\omega}{c}\right)^2\epsilon_r(\boldsymbol{x})\tilde{\varphi}_k^e\,\varphi_k^e d\Omega = \tilde{\boldsymbol{v}}_k^{(e)^T}\lambda_k M_\epsilon^{(e)}\boldsymbol{v}_k^{(e)}$$

$$\lambda_k = \left(\frac{\omega_k}{c}\right)^2$$

$$M_{\epsilon,ij}^{(e)} = \left(\frac{h}{2}\right)^2\int_e \epsilon_r^{(e)}\tilde{\phi}_i^e\phi_j^e\, d\xi d\eta$$

Collecting all terms we have

$$\tilde{\boldsymbol{v}}_k^{(e)^T}\left(K^{(e)} - i\boldsymbol{k}\cdot\boldsymbol{C}^{(e)} + |\boldsymbol{k}|^2 M^{(e)}\right)\boldsymbol{v}_k^{(e)} = \lambda_k \tilde{\boldsymbol{v}}_k^{(e)^T} M_\epsilon^{(e)} \boldsymbol{v}_k^{(e)} \tag{8.11}$$

Next, Eq.8.11 of all the elements are assembled into a comprehensive system of equations. Meanwhile, we need to eliminate some degrees of freedom that are not independent: (1) In the quad-tree mesh, a vortex positioned in the middle of an edge (red dots in Fig.8.2) depends on the nearest two vortices on the same edge (taking the interpolation). (2) Under periodic boundary condition, vortices on the interfacing boundaries are related by a phase factor $e^{i\boldsymbol{k}\cdot\boldsymbol{a}}$.

Assembling Eq.8.11 of all the elements and keeping only the independent degrees of freedom, we arrive at

$$\tilde{\boldsymbol{v}}_k^T(K - i\boldsymbol{k}\cdot\boldsymbol{C} + |\boldsymbol{k}|^2 M)\boldsymbol{v}_k = \lambda_k \tilde{\boldsymbol{v}}_k^T M_\epsilon \boldsymbol{v}_k \tag{8.12}$$

Because the test function can take arbitrary values, the vector of coefficients $\tilde{\boldsymbol{v}}^T$ can take arbitrary values, requiring

$$(K - i\boldsymbol{k}\cdot\boldsymbol{C} + |\boldsymbol{k}|^2 M)\boldsymbol{v}_k = \lambda_k M_\epsilon \boldsymbol{v}_k \tag{8.13}$$

Or equivalently,

$$(K - i\boldsymbol{k}\cdot\boldsymbol{C} + |\boldsymbol{k}|^2 M)V_k = M_\epsilon V_k \Lambda_k \tag{8.14}$$

where V_k is the orthonormal matrix of Eigen vectors. Λ_k is the diagonal matrix of eigen values $\lambda_{iband,k} = \left(\frac{\omega_{iband,k}}{c}\right)^2$, $iband = 1,2,3,\ldots$.

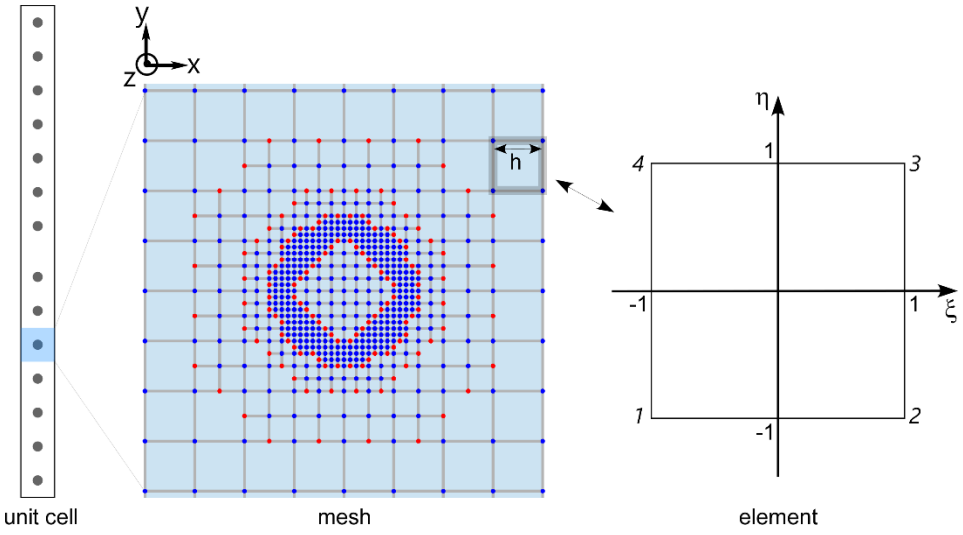

Figure 8.2: Quad-tree mesh shown around a rod. Dots represent vortices of the elements. Red dots represent vortices that are located in the middle of an edge, which are not independent degrees of freedom. Each square in the mesh is mapped to a local coordinate (ξ, η), on which the basis functions are defined.

8.2.2 Gradient Based Optimization

Topology optimization in photonics usually involve tuning thousands of parameters simultaneously. It is inefficient to use Newton or Quasi-Newton methods, because computing the Hessian or even the approximation of Hessian are numerically heavy. Instead, we use the globally-convergent method-of-moving-asymptotes (MMA) algorithm[147] to perform gradient-based local optimization, which is available in an open source package nlopt[149].

The gradients of the target and constraints versus the design parameters (i.e. permittivities in the design region $\epsilon_r^{\mathbb{D}}$) are

$$\frac{\partial f}{\partial \epsilon_r^{\mathbb{D}}} = \sum_{iband,k} \frac{\partial f}{\partial \omega_{iband,k}} \cdot \frac{\partial \omega_{iband,k}}{\partial \epsilon_r^{\mathbb{D}}} \tag{8.15}$$

$$\frac{\partial g_i}{\partial \epsilon_r^{\mathbb{D}}} = \sum_{iband,k} \frac{\partial g_i}{\partial \omega_{iband,k}} \cdot \frac{\partial \omega_{iband,k}}{\partial \epsilon_r^{\mathbb{D}}} \tag{8.16}$$

To find $\frac{\partial \omega_{iband,k}}{\partial \epsilon_r^{\mathbb{D}}}$ from Eq.8.14, we notice that for a generalized eigen value problem

$$A_k V_k = B_k V_k \Lambda_k \tag{8.17}$$

$$V_k^+ B_k V_k = I \tag{8.18}$$

the derivative of the i^{th} eigen value is

$$\lambda'_{i,k} = \boldsymbol{v}^{+}_{i,k}\left(A'_k - \lambda_{i,k}B'_k\right)\boldsymbol{v}_{i,k} \tag{8.19}$$

where $\boldsymbol{v}_{i,k}$ is the eigen vector corresponding to the i^{th} eigen value for a specific Bloch k. In our case (Eq.8.14), only M_ϵ depends on $\epsilon_r^{\mathbb{D}}$, which greatly simplifies the gradient calculation. Next, using the relation $\omega_{iband,k}/c = \sqrt{\lambda_{iband,k}}$, we can find $\frac{\partial \omega_{iband,k}}{\partial \epsilon_r^{\mathbb{D}}}$.

For numerical feasibility, we rewrite the target function as

$$f = \sum_{k\in[0.35\cdot\frac{2\pi}{a},0.5\cdot\frac{2\pi}{a}]} \omega^4_{wg,k} \tag{8.20}$$

which offers improved continuity compared to the original Eq.8.1. To save computational cost, we can limit the sum in Eq.8.20 to only a few k points that have higher frequencies in the range $k \in [0.35 \cdot \frac{2\pi}{a}, 0.5 \cdot \frac{2\pi}{a}]$ along the dispersion curve of the waveguide mode in Fig.8.1b, for example, using $0.45 \cdot 2\pi/a$ and $0.48 \cdot 2\pi/a$.

Regarding the choice of slack variables in the constraints specified by Eq.8.2 and Eq.8.3, we notice that first, the initial condition should satisfy the constraint, requiring $\varepsilon_i \geq 0$. Second, the target of lowering the frequencies of a specific mode in a specific range of *k* requires adding dielectrics, which inevitably lowers the frequencies for the global band structure. This requires $\varepsilon_i > 0$, to grant a certain percentage of down shifts in the global band structure. Third, larger ε_i allows more dielectrics to be added at the risk of drastically deforming the global band structure. To avoid the drastic deformation, ε_i should be controlled under 0.01. Finally, the slack variables ε_i can be treated as hyper-parameters that are optimized via grid search. Here we use $\varepsilon_1 = 0.003,\ \varepsilon_2 = 0.006$.

Mirror symmetries are enforced on the design regions, to maintain symmetries in the responses and optical forces. The mirror planes are located across the center of the unit cell (Fig.8.2a) both horizontally and vertically. The vertical mirror plane enforces the symmetry discussed in Section 3.3.3, leading to symmetric power and phase responses in the transmitted wave. This is crucial to ensure zero average axial forces contributed from

the responses in the transmitted wave, so that optical pulling forces are guaranteed by the incidence of backward-waves. The horizontal mirror plane makes the force field mirror symmetric between the upper and lower half of the waveguide. These symmetries reduce the number of design parameters by a factor of 4. Setting the minimum element size to be $a/128$, we have 3.5k independent design parameters.

8.2.3 Computation

We use python to implement the finite element method and gradient based optimization. The built-in data structures of python facilitate efficient finite element meshing and matrix assembling. Scipy provides fast and accurate computation for sparse linear algebra[16]. It is also convenient to parallelize the program using well-developed packages[17].

Notice that with 14 rods and a line defect in the unit cell, the waveguide mode of interest (blue curve in Fig.8.1b) which lies above the 2nd bulk band is located at the 29th eigenvalue, while the upper bulk mode involved in the constraints is located at the 30th eigenvalue. Therefore we only need to calculate the smallest 30 Eigen values and their corresponding Eigen vectors.

At each iteration, the solving of Eq.8.14 for different k are parallelized by broadcasting the current design parameters $\epsilon_r^{\mathbb{D}}$ from the master process to the parallel processes. Using a discretization with minimum element size of $a/128$, Eq.8.14 has 91k degrees of freedom. The individually solved eigenvalues and eigenvectors for each k are gathered from the parallel processes to the master process to compute the values and gradients of the target function and constraints, which are next fed into the optimization algorithm (MMA[147] implemented in nlopt[149]) for updating the design parameters $\epsilon_r^{\mathbb{D}}$.

[16] Using scipy.sparse.linalg.eigsh to solve the eigen value problem for sparse matrix.
[17] One can use either multiprocessing or mpi4py.

Each fully parallelized iteration takes 11 seconds on Xeon E5-2680 processors. The optimization usually converges within 50 iterations.

8.3 RESULTS

First, we allow continuous values for the permittivity $\epsilon_r^{\mathbb{D}}$ during optimization. The resultant distribution of dielectrics in the upper design region of Fig.8.1a is shown in Fig.8.3a. Following mirror symmetry, the lower design region in Fig.8.1a maps to the vertical flip of Fig.8.3a. The optimization have indeed lowered the frequencies of the waveguide mode in the range $k_x \in \left[0.35 \cdot \frac{2\pi}{a}, 0.5 \cdot \frac{2\pi}{a}\right]$, without drastically deforming the rest of the band structure (Fig.8.3b). Next, in order to arrive at a manufacturable structure, we apply level set method[148] to enforce binary permittivity values (Fig.8.3c), which leads to the dispersion relation as shown in Fig.8.3d. The backward-waves after topology optimization (blue curves in Fig.8.3b,d) have a broad frequency range (2.2%) for single mode operation.

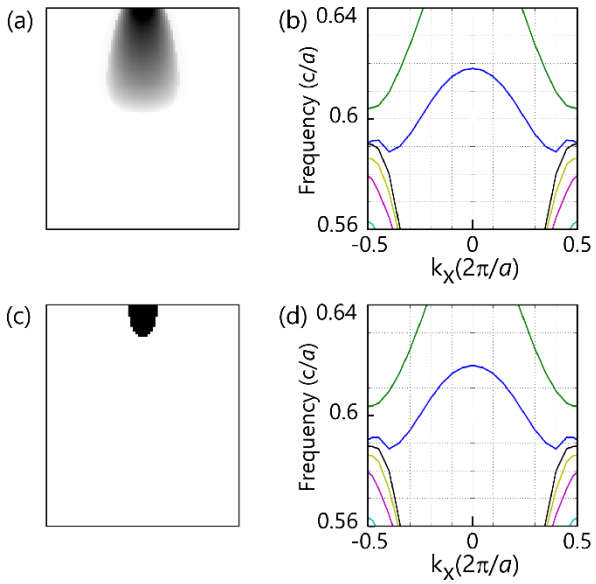

Figure 8.3: (a)(c) Distribution of dielectrics in the design region after optimization. The area maps to the upper design region, and vertically flipped lower design region in Fig.8.1a. Color scale represents relative permittivity from 1(white) to 12.25(black). (a) Permittivity takes continuous values. (c) Permittivity takes discrete values after applying level set, which yields a manufacturable geometry. (b)(d) Dispersion relations corresponding to (a)(c). The waveguide mode (blue curves) now support a broad frequency range of single-mode backward-wave operation.

8.4 Concluding Remarks

In this chapter, we incorporated topology optimization to replace human effort for the dispersion engineering task encountered in Chapter 4. We performed a gradient based dispersion engineering to enable broad-band (2.2%) single mode operation of a backward-wave mode, which can be used to generate long range and robust optical pulling forces in an all silicon guided wave system (Chapter4).

Topology optimization is a powerful technique for seeking device performance beyond intuition. Nowadays, many finite element/finite difference based commercial software, such as COMSOL[48] and CST[150], are also increasing their efforts to incorporate topology optimization functionalities. Topology optimization have great

potential to take over the inefficient hand-tuning or parameter sweeping in photonics and optomechanics structural design, given that suitable target functions and constraints can be formulated specific to the problem.

References

[1] D. G. Grier, "A revolution in optical manipulation," *Nature*, vol. 424, no. 6950, pp. 810–816, 2003.

[2] A. Hayat, J. P. B. Mueller, and F. Capasso, "Lateral chirality-sorting optical forces," *Proc. Natl. Acad. Sci.*, vol. 112, no. 43, pp. 13190–13194, Oct. 2015.

[3] V. Demergis and E.-L. Florin, "Ultrastrong Optical Binding of Metallic Nanoparticles," *Nano Lett.*, vol. 12, no. 11, pp. 5756–5760, Nov. 2012.

[4] M. Ozkan, M. Wang, C. Ozkan, R. Flynn, and S. Esener, "Optical Manipulation of Objects and Biological Cells in Microfluidic Devices," *Biomed. Microdevices*, vol. 5, no. 1, pp. 61–67, Mar. 2003.

[5] S. Chu, J. E. Bjorkholm, A. Ashkin, and A. Cable, "Demonstration of Laser Cooling and Trapping of Atoms," in *Atomic Physics*, I. Shimamura, Ed. Amsterdam: Elsevier, 1987, pp. 377–393.

[6] M. Li, W. H. P. Pernice, C. Xiong, T. Baehr-Jones, M. Hochberg, and H. X. Tang, "Harnessing optical forces in integrated photonic circuits," *Nature*, vol. 456, no. 7221, pp. 480–484, Nov. 2008.

[7] M. Aspelmeyer, T. J. Kippenberg, and F. Marquardt, "Cavity optomechanics," *Rev. Mod. Phys.*, vol. 86, no. 4, pp. 1391–1452, Dec. 2014.

[8] M. Eichenfield, J. Chan, R. M. Camacho, K. J. Vahala, and O. Painter, "Optomechanical crystals," *Nature*, vol. 462, no. 7269, pp. 78–82, Nov. 2009.

[9] M. L. Povinelli *et al.*, "Evanescent-wave bonding between optical waveguides," *Opt. Lett.*, vol. 30, no. 22, pp. 3042–3044, 2005.

[10] P. T. Rakich, C. Reinke, R. Camacho, P. Davids, and Z. Wang, "Giant Enhancement of Stimulated Brillouin Scattering in the Subwavelength Limit," *Phys. Rev. X*, vol. 2, no. 1, p. 011008, Jan. 2012.

[11] E. A. Kittlaus, H. Shin, and P. T. Rakich, "Large Brillouin amplification in silicon," *Nat. Photonics*, vol. 10, no. 7, pp. 463–467, Jul. 2016.

[12] H. Shin *et al.*, "Tailorable stimulated Brillouin scattering in nanoscale silicon waveguides.," *Nat. Commun.*, vol. 4, p. 1944, Jan. 2013.

[13] H. Shin, J. A. Cox, R. Jarecki, A. Starbuck, Z. Wang, and P. T. Rakich, "Control of coherent information via on-chip photonic–phononic emitter–receivers," *Nat. Commun.*, vol. 6, p. 6427, Mar. 2015.

[14] J. D. Joannopoulos, S. G. Johnson, J. N. Winn, and R. D. Meade, *Photonic Crystals: Molding the Flow of Light*, 2nd ed. Princeton University Press, 2011.

[15] Z. Lin, A. Pick, M. Lončar, and A. W. Rodriguez, "Enhanced Spontaneous Emission at Third-Order Dirac Exceptional Points in Inverse-Designed Photonic Crystals," *Phys. Rev. Lett.*, vol. 117, no. 10, p. 107402, Aug. 2016.

[16] A. Y. Piggott, J. Lu, K. G. Lagoudakis, J. Petykiewicz, T. M. Babinec, and J. Vučković, "Inverse design and demonstration of a compact and broadband on-chip wavelength demultiplexer," *Nat. Photonics*, vol. 9, no. 6, p. nphoton.2015.69, May 2015.

[17] Z. Wang, Y. Chong, J. D. Joannopoulos, and M. Soljacić, "Observation of unidirectional backscattering-immune topological electromagnetic states.," *Nature*, vol. 461, no. 7265, pp. 772–5, Oct. 2009.
[18] S. H. Mousavi, P. T. Rakich, and Z. Wang, "Strong THz and Infrared Optical Forces on a Suspended Single-Layer Graphene Sheet," *ACS Photonics*, vol. 1, no. 11, pp. 1107–1115, Nov. 2014.
[19] I. A. D. Williamson, S. H. Mousavi, and Z. Wang, "Extraordinary wavelength reduction in terahertz graphene-cladded photonic crystal slabs," *ArXiv150900443 Phys.*, Sep. 2015.
[20] D. Wang, I. Williamson, H. Mousavi, and Z. Wang, "Strong Attractive Force Between Graphene Sheets at Terahertz Induced by Extraordinary Wavelength Reduction," in *Conference on Lasers and Electro-Optics (2016), paper FTu3B.6*, 2016, p. FTu3B.6.
[21] I. A. D. Williamson, S. H. Mousavi, and Z. Wang, "Dual-carrier Floquet circulator with time-modulated optical resonators," *ArXiv170804005 Phys.*, Aug. 2017.
[22] Y. Shi, Z. Yu, and S. Fan, "Limitations of nonlinear optical isolators due to dynamic reciprocity," *Nat. Photonics*, vol. 9, no. 6, pp. 388–392, Jun. 2015.
[23] M. Ghebrebrhan, M. Ibanescu, S. G. Johnson, M. Soljaćić, and J. D. Joannopoulos, "Distinguishing zero-group-velocity modes in photonic crystals," *Phys. Rev. A*, vol. 76, no. 6, p. 063810, Dec. 2007.
[24] A. Salandrino and D. N. Christodoulides, "Reverse optical forces in negative index dielectric waveguide arrays.," *Opt. Lett.*, vol. 36, no. 16, pp. 3103–5, Aug. 2011.
[25] J. Nemirovsky, M. C. Rechtsman, and M. Segev, "Negative radiation pressure and negative effective refractive index via dielectric birefringence.," *Opt. Express*, vol. 20, no. 8, pp. 8907–14, Apr. 2012.
[26] V. M. Shalaev, "Optical negative-index metamaterials," *Nat. Photonics*, vol. 1, no. 1, pp. 41–48, Jan. 2007.
[27] J. He, Y. Jin, Z. Hong, and S. He, "Slow light in a dielectric waveguide with negative-refractive-index photonic crystal cladding," *Opt. Express*, vol. 16, no. 15, p. 11077, Jul. 2008.
[28] A. H. Safavi-Naeini *et al.*, "Electromagnetically induced transparency and slow light with optomechanics," *Nature*, vol. 472, no. 7341, pp. 69–73, Apr. 2011.
[29] Z. Wang, Y. Chong, J. D. Joannopoulos, and M. Soljačić, "Reflection-Free One-Way Edge Modes in a Gyromagnetic Photonic Crystal," *Phys. Rev. Lett.*, vol. 100, no. 1, pp. 013905–013905, Jan. 2008.
[30] W. Qiu, Z. Wang, and M. Soljačić, "Broadband circulators based on directional coupling of one-way waveguides," *Opt. Express*, vol. 19, no. 22, pp. 22248–22257, 2011.
[31] Z. Yu and S. Fan, "Optical isolation based on nonreciprocal phase shift induced by interband photonic transitions," *Appl. Phys. Lett.*, vol. 94, no. 17, p. 171116, Apr. 2009.

[32] K. Fang, Z. Yu, and S. Fan, “Realizing effective magnetic field for photons by controlling the phase of dynamic modulation,” *Nat. Photonics*, vol. 6, no. 11, pp. 782–787, Oct. 2012.
[33] A. B. Khanikaev, S. H. Mousavi, W.-K. Tse, M. Kargarian, A. H. MacDonald, and G. Shvets, “Photonic topological insulators.,” *Nat. Mater.*, vol. 12, no. 3, pp. 233–9, Mar. 2013.
[34] T. Ma, A. B. Khanikaev, S. H. Mousavi, and G. Shvets, “Guiding Electromagnetic Waves around Sharp Corners: Topologically Protected Photonic Transport in Metawaveguides,” *Phys. Rev. Lett.*, vol. 114, no. 12, p. 127401, Mar. 2015.
[35] I. A. D. Williamson, S. H. Mousavi, and Z. Wang, “Extraordinary wavelength reduction in terahertz graphene-cladded photonic crystal slabs,” *Sci. Rep.*, vol. 6, p. 25301, May 2016.
[36] S. H. Mousavi, I. A. D. Williamson, and Z. Wang, “Kinetic inductance driven nanoscale 2D and 3D THz transmission lines,” *Sci. Rep.*, vol. 6, p. 25303, May 2016.
[37] A. Dogariu, S. Sukhov, and J. Sáenz, “Optically induced ‘negative forces,’” *Nat. Photonics*, vol. 7, no. 1, pp. 24–27, Jan. 2013.
[38] B. Lombardet, L. A. Dunbar, R. Ferrini, and R. Houdré, “Fourier analysis of Bloch wave propagation in photonic crystals,” *J. Opt. Soc. Am. B*, vol. 22, no. 6, p. 1179, 2005.
[39] W. Sun, S. B. Wang, J. Ng, L. Zhou, and C. T. Chan, “Analytic derivation of electrostrictive tensors and their application to optical force density calculations,” *Phys. Rev. B*, vol. 91, no. 23, p. 235439, Jun. 2015.
[40] S. Wang, J. Ng, M. Xiao, and C. T. Chan, “Electromagnetic stress at the boundary: Photon pressure or tension?,” *Sci. Adv.*, vol. 2, no. 3, p. e1501485, Mar. 2016.
[41] A. S. Ang, S. V. Sukhov, A. Dogariu, and A. S. Shalin, “Scattering Forces within a Left-Handed Photonic Crystal,” *Sci. Rep.*, vol. 7, p. 41014, Jan. 2017.
[42] P. T. Rakich, M. A. Popovic, and Z. Wang, “General treatment of optical forces and potentials in mechanically variable photonic systems,” *Opt. Express*, vol. 17, no. 20, p. 18116, Sep. 2009.
[43] Z. Wang and P. Rakich, “Response theory of optical forces in two-port photonics systems: a simplified framework for examining conservative and non-conservative forces,” *Opt. Express*, vol. 19, no. 22, pp. 22322–22336, Oct. 2011.
[44] J. D. Jackson, *Classical Electrodynamics*, 3rd ed. Wiley, 1998.
[45] H. A. Haus, *Fields and Waves in Optoelectronics*. Prentice Hall, Incorporated, 1984.
[46] H. Haus and W. P. Huang, “Coupled-mode theory,” *Proc. IEEE*, vol. 79, no. 10, pp. 1505–1518, Oct. 1991.
[47] J.-M. Jin, *The Finite Element Method in Electromagnetics*, 2 edition. New York: Wiley-IEEE Press, 2002.
[48] *COMSOL Multiphysics*. COMSOL Inc.
[49] J. J. Sáenz, “Optical forces: Laser tractor beams,” *Nat. Photonics*, vol. 5, no. 9, pp. 514–515, Sep. 2011.

[50] S. Sukhov and A. Dogariu, “Negative Nonconservative Forces: Optical ‘Tractor Beams’ for Arbitrary Objects,” *Phys. Rev. Lett.*, vol. 107, no. 20, pp. 1–5, Nov. 2011.
[51] O. Brzobohatý, V. Karásek, M. Šiler, L. Chvátal, T. Čižmár, and P. Zemánek, “Experimental demonstration of optical transport, sorting and self-arrangement using a ‘tractor beam,’” *Nat. Photonics*, vol. 7, no. 2, pp. 123–127, Jan. 2013.
[52] J. Chen, J. Ng, Z. Lin, and C. T. Chan, “Optical pulling force,” *Nat. Photonics*, vol. 5, no. 9, pp. 531–534, Jul. 2011.
[53] A. Novitsky, C.-W. Qiu, and H. Wang, “Single Gradientless Light Beam Drags Particles as Tractor Beams,” *Phys. Rev. Lett.*, vol. 107, no. 20, pp. 203601–203601, Nov. 2011.
[54] A. Novitsky, C.-W. Qiu, and A. Lavrinenko, “Material-Independent and Size-Independent Tractor Beams for Dipole Objects,” *Phys. Rev. Lett.*, vol. 109, no. 2, pp. 023902–023902, Jul. 2012.
[55] N. Wang, J. Chen, S. Liu, and Z. Lin, “Dynamical and phase-diagram study on stable optical pulling force in Bessel beams,” *Phys. Rev. A*, vol. 87, no. 6, pp. 063812–063812, Jun. 2013.
[56] C. Pfeiffer and A. Grbic, “Generating stable tractor beams with dielectric metasurfaces,” *Phys. Rev. B*, vol. 91, no. 11, p. 115408, Mar. 2015.
[57] A. Novitsky and C.-W. Qiu, “Pulling extremely anisotropic lossy particles using light without intensity gradient,” *Phys. Rev. A*, vol. 90, no. 5, Nov. 2014.
[58] S. Sukhov and A. Dogariu, “On the concept of ‘tractor beams’.,” *Opt. Lett.*, vol. 35, no. 22, pp. 3847–9, Nov. 2010.
[59] K. Ding, J. Ng, L. Zhou, and C. T. Chan, “Realization of optical pulling forces using chirality,” *Phys. Rev. A*, vol. 89, no. 6, pp. 063825–063825, Jun. 2014.
[60] F. G. Mitri, R. X. Li, R. P. Yang, L. X. Guo, and C. Y. Ding, “Optical pulling force on a magneto-dielectric Rayleigh sphere in Bessel tractor polarized beams,” *J. Quant. Spectrosc. Radiat. Transf.*, vol. 184, pp. 360–381, Nov. 2016.
[61] V. Intaraprasonk and S. Fan, “Optical pulling force and conveyor belt effect in resonator-waveguide system.,” *Opt. Lett.*, vol. 38, no. 17, pp. 3264–7, Sep. 2013.
[62] A. V. Maslov, “Resonant Pulling of a Microparticle Using a Backward Surface Wave,” *Phys. Rev. Lett.*, vol. 112, no. 11, pp. 113903–113903, Mar. 2014.
[63] M. Z. Hasan and C. L. Kane, “Colloquium: topological insulators,” *Rev. Mod. Phys.*, vol. 82, no. 4, p. 3045, 2010.
[64] H. He, M. E. J. Friese, N. R. Heckenberg, and H. Rubinsztein-Dunlop, “Direct Observation of Transfer of Angular Momentum to Absorptive Particles from a Laser Beam with a Phase Singularity,” *Phys. Rev. Lett.*, vol. 75, no. 5, pp. 826–829, Jul. 1995.
[65] Y. Roichman, B. Sun, Y. Roichman, J. Amato-Grill, and D. G. Grier, “Optical Forces Arising from Phase Gradients,” *Phys. Rev. Lett.*, vol. 100, no. 1, p. 013602, Jan. 2008.

[66] P. T. Rakich, Z. Wang, and P. Davids, “Scaling of optical forces in dielectric waveguides: rigorous connection between radiation pressure and dispersion,” *Opt. Lett.*, vol. 36, no. 2, pp. 217–219, Jan. 2011.
[67] R. Stainko and O. Sigmund, “Tailoring dispersion properties of photonic crystal waveguides by topology optimization,” *Waves Random Complex Media*, vol. 17, no. 4, pp. 477–489, Oct. 2007.
[68] F. Wang, J. S. Jensen, and O. Sigmund, “Robust topology optimization of photonic crystal waveguides with tailored dispersion properties,” *JOSA B*, vol. 28, no. 3, pp. 387–397, Mar. 2011.
[69] M. P. Bendsoe and O. Sigmund, *Topology Optimization: Theory, Methods, and Applications*, 2nd ed. Berlin Heidelberg: Springer-Verlag, 2004.
[70] M. HAN, “Optimal Design of Photonic Crystals,” Thesis, 2010.
[71] “MIT Photonic Bands - AbInitio.” [Online]. Available: http://ab-initio.mit.edu/wiki/index.php?title=MIT_Photonic_Bands&printable=yes.
[72] U. S. Inan and R. A. Marshall, *Numerical Electromagnetics: The FDTD Method*. Cambridge University Press, 2011.
[73] J. T. Oden, E. B. Becker, and G. F. Carey, *001: Finite Elements: An Introduction. Volume I*, 6th Printing edition. Englewood Cliffs, N.J: Prentice Hall, 1981.
[74] D. Ray, *Computation of Nonlinear Structures: Extremely Large Elements for Frames, Plates and Shells*, 1 edition. Chichester: Wiley, 2015.
[75] N. Descharmes, U. Dharanipathy, Z. Diao, M. Tonin, and R. Houdré, “Observation of Backaction and Self-Induced Trapping in a Planar Hollow Photonic Crystal Cavity,” *Phys. Rev. Lett.*, vol. 110, no. 12, p. 123601, Mar. 2013.
[76] S. Fan, W. Suh, and J. Joannopoulos, “Temporal coupled-mode theory for the Fano resonance in optical resonators,” *JOSA A*, vol. 20, no. 3, pp. 569–572, 2003.
[77] K. X. Wang, Z. Yu, S. Sandhu, and S. Fan, “Fundamental bounds on decay rates in asymmetric single-mode optical resonators,” *Opt. Lett.*, vol. 38, no. 2, pp. 100–102, 2013.
[78] N. Descharmes, U. P. Dharanipathy, Z. Diao, M. Tonin, and R. Houdré, “Resonant optical trapping and back-action effects in a hollow photonic crystal cavity,” in *2013 15th International Conference on Transparent Optical Networks (ICTON)*, 2013, pp. 1–2.
[79] V. Kajorndejnukul, W. Ding, S. Sukhov, C.-W. Qiu, and A. Dogariu, “Linear momentum increase and negative optical forces at dielectric interface,” *Nat. Photonics*, vol. 7, no. 10, pp. 787–790, Aug. 2013.
[80] C.-W. Qiu *et al.*, “Photon momentum transfer in inhomogeneous dielectric mixtures and induced tractor beams,” *Light Sci. Appl.*, vol. 4, no. 4, p. e278, Apr. 2015.
[81] M. I. Petrov, S. V. Sukhov, A. A. Bogdanov, A. S. Shalin, and A. Dogariu, “Surface plasmon polariton assisted optical pulling force,” *Laser Photonics Rev.*, vol. 10, no. 1, pp. 116–122, Jan. 2016.
[82] S.-H. Lee, Y. Roichman, and D. G. Grier, “Optical solenoid beams.,” *Opt. Express*, vol. 18, no. 7, pp. 6988–93, Mar. 2010.

[83] A. Canaguier-Durand and C. Genet, “Chiral route to pulling optical forces and left-handed optical torques,” *Phys. Rev. A*, vol. 92, no. 4, p. 043823, Oct. 2015.
[84] A. Mizrahi and Y. Fainman, “Negative radiation pressure on gain medium structures.,” *Opt. Lett.*, vol. 35, no. 20, pp. 3405–7, Oct. 2010.
[85] K. J. Webb, “Negative electromagnetic plane-wave force in gain media,” *Phys. Rev. E*, vol. 84, no. 5, pp. 057602–057602, Nov. 2011.
[86] A. S. Desyatnikov, V. G. Shvedov, A. V. Rode, W. Krolikowski, and Y. S. Kivshar, “Photophoretic manipulation of absorbing aerosol particles with vortex beams: theory versus experiment.,” *Opt. Express*, vol. 17, no. 10, pp. 8201–11, May 2009.
[87] V. Shvedov, A. R. Davoyan, C. Hnatovsky, N. Engheta, and W. Krolikowski, “A long-range polarization-controlled optical tractor beam,” *Nat. Photonics*, vol. 8, no. 11, pp. 846–850, Nov. 2014.
[88] O. Ilic, I. Kaminer, Y. Lahini, H. Buljan, and M. Soljačić, “Exploiting Optical Asymmetry for Controlled Guiding of Particles with Light,” *ACS Photonics*, vol. 3, no. 2, pp. 197–202, Feb. 2016.
[89] M. V. Berry and N. L. Balazs, “Nonspreading wave packets,” *Am. J. Phys.*, vol. 47, no. 3, pp. 264–267, Mar. 1979.
[90] M. Burla *et al.*, “System integration and radiation pattern measurements of a phased array antenna employing an integrated photonic beamformer for radio astronomy applications,” *Appl. Opt.*, vol. 51, no. 7, pp. 789–802, Mar. 2012.
[91] T. M. Squires and S. R. Quake, “Microfluidics: Fluid physics at the nanoliter scale,” *Rev. Mod. Phys.*, vol. 77, no. 3, pp. 977–1026, Oct. 2005.
[92] L. Lu, J. D. Joannopoulos, and M. Soljačić, “Topological photonics,” *Nat. Photonics*, vol. 8, no. 11, pp. 821–829, Nov. 2014.
[93] T. Ozawa *et al.*, “Topological Photonics,” *ArXiv180204173 Cond-Mat Physicsphysics Physicsquant-Ph*, Feb. 2018.
[94] A. B. Khanikaev and G. Shvets, “Two-dimensional topological photonics,” *Nat. Photonics*, vol. 11, no. 12, pp. 763–773, Dec. 2017.
[95] D. Wang, C. Qiu, P. T. Rakich, and Z. Wang, “Guide-wave Photonic Pulling Force Using One-way Photonic Chiral Edge States,” in *CLEO: 2015 (2015), paper FM2D.7*, 2015, p. FM2D.7.
[96] B. A. Bernevig and T. L. Hughes, *Topological insulators and topological superconductors*. Princeton: Princeton University Press, 2013.
[97] Y. Hatsugai, “Chern number and edge states in the integer quantum Hall effect,” *Phys. Rev. Lett.*, vol. 71, no. 22, pp. 3697–3700, Nov. 1993.
[98] C. L. Kane and E. J. Mele, “Z2 Topological Order and the Quantum Spin Hall Effect,” *Phys. Rev. Lett.*, vol. 95, no. 14, p. 146802, Sep. 2005.
[99] A. B. Khanikaev, S. Hossein Mousavi, W.-K. Tse, M. Kargarian, A. H. MacDonald, and G. Shvets, “Photonic topological insulators,” *Nat. Mater.*, vol. 12, no. 3, pp. 233–239, Mar. 2013.
[100] D. J. Thouless, M. Kohmoto, M. P. Nightingale, and M. den Nijs, “Quantized Hall Conductance in a Two-Dimensional Periodic Potential,” *Phys. Rev. Lett.*, vol. 49, no. 6, pp. 405–408, Aug. 1982.

[101] Z. Wang, Y. D. Chong, J. D. Joannopoulos, and M. Soljacić, "Reflection-Free One-Way Edge Modes in a Gyromagnetic Photonic Crystal," *Phys. Rev. Lett.*, vol. 100, no. 1, p. 4, Jan. 2007.
[102] Z. Yu, Z. Wang, and S. Fan, "One-way total reflection with one-dimensional magneto-optical photonic crystals," *Appl. Phys. Lett.*, vol. 90, no. 12, p. 121133, 2007.
[103] D. Marcuse, "Mode conversion caused by surface imperfections of a dielectric slab waveguide," *Bell Syst. Tech. J.*, vol. 48, no. 10, pp. 3187–3215, Dec. 1969.
[104] B. R. Munson, A. P. Rothmayer, and T. H. Okiishi, *Fundamentals of Fluid Mechanics*, 7th ed. Wiley Global Education, 2012.
[105] S. Lin, "Experimental Demonstration of Guiding and Bending of Electromagnetic Waves in a Photonic Crystal," *Science*, vol. 282, no. 5387, pp. 274–276, Oct. 1998.
[106] S. Fan, S. G. Johnson, J. D. Joannopoulos, C. Manolatou, and H. a. Haus, "Waveguide branches in photonic crystals," *J. Opt. Soc. Am. B*, vol. 18, no. 2, p. 162, 2001.
[107] H. Lira, Z. Yu, S. Fan, and M. Lipson, "Electrically Driven Nonreciprocity Induced by Interband Photonic Transition on a Silicon Chip," *Phys. Rev. Lett.*, vol. 109, no. 3, p. 033901, Jul. 2012.
[108] S. A. Skirlo, L. Lu, Y. Igarashi, Q. Yan, J. Joannopoulos, and M. Soljačić, "Experimental Observation of Large Chern Numbers in Photonic Crystals," *Phys. Rev. Lett.*, vol. 115, no. 25, p. 253901, Dec. 2015.
[109] Z. Yu, G. Veronis, Z. Wang, and S. Fan, "One-Way Electromagnetic Waveguide Formed at the Interface between a Plasmonic Metal under a Static Magnetic Field and a Photonic Crystal," *Phys. Rev. Lett.*, vol. 100, no. 2, p. 023902, Jan. 2008.
[110] et al John D. Joannopoulos, *Photonic Crystals Molding the Flow of Light*, Second Edi. Princton University Press, 2008.
[111] "Ashkin 1970 PRL_Acceleration Trapping particles Radiation Pressure.pdf." .
[112] a Ashkin, "Forces of a single-beam gradient laser trap on a dielectric sphere in the ray optics regime.," *Methods Cell Biol.*, vol. 55, no. February, pp. 1–27, Jan. 1998.
[113] A. K. Zvezdin and V. A. Kotov, *Modern Magnetooptics and Magnetooptical Materials*. CRC Press, 1997.
[114] D. M. Pozar, *Microwave engineering*, 4th ed. Hoboken, NJ: Wiley, 2012.
[115] C. Luo, S. G. Johnson, J. D. Joannopoulos, and J. B. Pendry, "All-angle negative refraction without negative effective index," *Phys. Rev. B*, vol. 65, no. 20, p. 201104, May 2002.
[116] D. Wang and Z. Wang, "Optical Pulling Force in Periodic Backward-wave Waveguides," in *Conference on Lasers and Electro-Optics (2017), paper FTh1H.4*, 2017, p. FTh1H.4.
[117] I. A. D. Williamson, S. H. Mousavi, and Z. Wang, "Extraordinary wavelength reduction in terahertz graphene-cladded photonic crystal slabs," *Sci. Rep.*, vol. 6, p. 25301, May 2016.

[118] S. Fan, S. G. Johnson, J. D. Joannopoulos, C. Manolatou, and H. A. Haus, "Waveguide branches in photonic crystals," *J. Opt. Soc. Am. B*, vol. 18, no. 2, p. 162, 2001.
[119] M. Nieto-Vesperinas, R. Gomez-Medina, and J. J. Saenz, "Angle-suppressed scattering and optical forces on submicrometer dielectric particles.," *J. Opt. Soc. Am. A Opt. Image Sci. Vis.*, vol. 28, no. 1, pp. 54–60, Jan. 2011.
[120] K. J. Chau and H. J. Lezec, "Revisiting the Balazs thought experiment in the case of a left-handed material: electromagnetic-pulse-induced displacement of a dispersive, dissipative negative-index slab," *Opt. Express*, vol. 20, no. 9, pp. 10138–10162, Apr. 2012.
[121] P. W. Milonni and R. W. Boyd, "Momentum of Light in a Dielectric Medium," *Adv. Opt. Photonics*, vol. 2, no. 4, pp. 519–553, Dec. 2010.
[122] S. M. Barnett, "Resolution of the Abraham-Minkowski Dilemma," *Phys. Rev. Lett.*, vol. 104, no. 7, pp. 1–4, Feb. 2010.
[123] K. Y. Bliokh, A. Y. Bekshaev, and F. Nori, "Extraordinary momentum and spin in evanescent waves," *Nat. Commun.*, vol. 5, p. 3300, Mar. 2014.
[124] A. Aiello, P. Banzer, M. Neugebauer, and G. Leuchs, "From transverse angular momentum to photonic wheels," *Nat. Photonics*, vol. 9, no. 12, pp. 789–795, Dec. 2015.
[125] S. Matsuo *et al.*, "Laser microfabrication and rotation of ship-in-a-bottle optical rotators," *Appl. Phys. Lett.*, vol. 93, no. 5, p. 051107, 2008.
[126] M. Liu, T. Zentgraf, Y. Liu, G. Bartal, and X. Zhang, "Light-driven nanoscale plasmonic motors.," *Nat. Nanotechnol.*, vol. 5, no. 8, pp. 570–3, Aug. 2010.
[127] E. Higurashi, H. Ukita, H. Tanaka, and O. Ohguchi, "Optically induced rotation of anisotropic micro-objects fabricated by surface micromachining," *Appl. Phys. Lett.*, vol. 64, no. 17, p. 2209, 1994.
[128] M. H. Alizadeh and B. M. Reinhard, "Transverse Chiral Optical Forces by Chiral Surface Plasmon Polaritons," *ACS Photonics*, vol. 2, no. 12, pp. 1780–1788, Dec. 2015.
[129] K. D. Wulff, D. G. Cole, and R. L. Clark, "Controlled rotation of birefringent particles in an optical trap.," *Appl. Opt.*, vol. 47, no. 34, pp. 6428–33, Dec. 2008.
[130] P.-C. Li, J.-C. Chang, A. La Porta, and E. T. Yu, "Fabrication of birefringent nanocylinders for single-molecule force and torque measurement," *Nanotechnology*, vol. 25, no. 23, p. 235304, Jun. 2014.
[131] L. Thylén, M. Qiu, and S. Anand, "Photonic Crystals—A Step towards Integrated Circuits for Photonics," *ChemPhysChem*, vol. 5, no. 9, pp. 1268–1283, Sep. 2004.
[132] C. Chen, "Graphene NanoElectroMechanical Resonators and Oscillators," 2013.
[133] D. Akinwande *et al.*, "A review on mechanics and mechanical properties of 2D materials—Graphene and beyond," *Extreme Mech. Lett.*, vol. 13, pp. 42–77, May 2017.
[134] X. Song, M. Oksanen, J. Li, P. J. Hakonen, and M. A. Sillanpää, "Graphene Optomechanics Realized at Microwave Frequencies," *Phys. Rev. Lett.*, vol. 113, no. 2, p. 027404, Jul. 2014.

[135] R. A. Barton *et al.*, "Photothermal Self-Oscillation and Laser Cooling of Graphene Optomechanical Systems," *Nano Lett.*, vol. 12, no. 9, pp. 4681–4686, Sep. 2012.
[136] R. M. Cole *et al.*, "Evanescent-Field Optical Readout of Graphene Mechanical Motion at Room Temperature," *Phys. Rev. Appl.*, vol. 3, no. 2, p. 024004, Feb. 2015.
[137] X. Yang, Y. Liu, R. F. Oulton, X. Yin, and X. Zhang, "Optical Forces in Hybrid Plasmonic Waveguides," *Nano Lett.*, vol. 11, no. 2, pp. 321–328, Feb. 2011.
[138] W. Lu, H. Chen, S. Liu, J. Zi, and Z. Lin, "Extremely strong bipolar optical interactions in paired graphene nanoribbons," *Phys. Chem. Chem. Phys.*, vol. 18, no. 12, pp. 8561–8569, Mar. 2016.
[139] W. Qiu, "Nanophotonics for tailoring light-matter interaction/," Thesis, Massachusetts Institute of Technology, 2013.
[140] R. W. Boyd, *Nonlinear Optics*. Academic Press, 2008.
[141] J. Atalaya, A. Isacsson, and J. M. Kinaret, "Continuum Elastic Modeling of Graphene Resonators," *Nano Lett.*, vol. 8, no. 12, pp. 4196–4200, 2008.
[142] X. Liang and S. G. Johnson, "Formulation for scalable optimization of microcavities via the frequency-averaged local density of states," *Opt. Express*, vol. 21, no. 25, pp. 30812–30841, Dec. 2013.
[143] J. Lu, S. Boyd, and J. Vučković, "Inverse design of a three-dimensional nanophotonic resonator," *Opt. Express*, vol. 19, no. 11, pp. 10563–10570, May 2011.
[144] L. Su, A. Y. Piggott, N. V. Sapra, J. Petykiewicz, and J. Vučković, "Inverse Design and Demonstration of a Compact on-Chip Narrowband Three-Channel Wavelength Demultiplexer," *ACS Photonics*, Nov. 2017.
[145] Z. Lin, X. Liang, M. Lončar, S. G. Johnson, and A. W. Rodriguez, "Cavity-enhanced second-harmonic generation via nonlinear-overlap optimization," *Optica*, vol. 3, no. 3, pp. 233–238, Mar. 2016.
[146] T. H. Lee, "Adjoint Method for Design Sensitivity Analysis of Multiple Eigenvalues and Associated Eigenvectors," *AIAA J.*, vol. 45, no. 8, pp. 1998–2004, 2007.
[147] K. Svanberg, "A Class of Globally Convergent Optimization Methods Based on Conservative Convex Separable Approximations," *SIAM J. Optim.*, vol. 12, no. 2, pp. 555–573, Jan. 2002.
[148] S. Osher and R. Fedkiw, *Level Set Methods and Dynamic Implicit Surfaces*, 2003 edition. New York: Springer, 2002.
[149] Steven G. Johnson, "The NLopt nonlinear-optimization package." http://ab-initio.mit.edu/nlopt.
[150] "CST - Computer Simulation Technology." [Online]. Available: https://www.cst.com/.